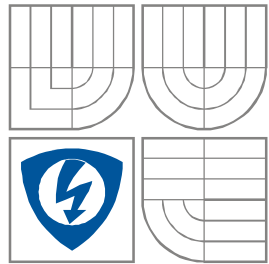




VYSOKÉ UČENÍ TECHNICKÉ V BRNĚ
BRNO UNIVERSITY OF TECHNOLOGY



FAKULTA ELEKTROTECHNIKY A KOMUNIKAČNÍCH
TECHNOLOGIÍ
ÚSTAV RADIOELEKTRONIKY

FACULTY OF ELECTRICAL ENGINEERING AND COMMUNICATION
DEPARTMENT OF RADIO ELECTRONICS

POLARIZATION IMPERFECTIONS OF LIGHT IN INTERFEROMETRY

POLARIZAČNÍ NEDOKONALOSTI SVĚTLA V INTERFEROMETRII

DISERTAČNÍ PRÁCE
DISSERTATION THESIS

AUTOR PRÁCE
AUTHOR

Ing. Petr Kučera

VEDOUCÍ PRÁCE
SUPERVISOR

prof. Ing. Otakar Wilfert, CSc.

Abstrakt

Disertační práce pojednává o polarizačních nedokonalostech optických komponentů, které jsou využívány ke kontrole a k transformaci polarizačního stavu světla. Získané teoretické výsledky jsou pak využity ve vybraných aplikacích, jež ke své činnosti využívají právě polarizace světla. Konkrétně se jedná o zařízení měřící vibrace oscilujících objektů, dále o interferenční měření dvojlomu v transparentních materiálech a konečně, o vybraná témata z optické kvantové komunikace.

Klíčová slova

Polarizace světla, polarizační stav, interferometrie, polarimetrie, stav fotonu.

Abstract

The emphasis of the dissertation is put on the investigating of polarization imperfections of optical components which are used to control and transform polarization of light. The theoretical results of this investigation are then applied to different applications which exploit light polarization, namely to the arrangements for high-resolution measurement of vibrating targets, to interferometric measurements for the determination of stress-induced birefringence in transparent materials and to the selected topics in quantum optical communication.

Keywords

Polarization of light, state of polarization, interferometry, vibrometry, polarimetry, state of the photon.

Prohlášení

Prohlašuji, že svou disertační práci na téma Polarizační nedokonalosti světla v interferometrii jsem vypracoval samostatně pod vedením školitele a s použitím odborné literatury a dalších informačních zdrojů, které jsou všechny citovány v práci a uvedeny v seznamu literatury na konci práce.

Jako autor uvedené disertační práce dále prohlašuji, že v souvislosti s vytvořením této disertační práce jsem neporušil autorská práva třetích osob, zejména jsem nezasáhl nedovoleným způsobem do cizích autorských práv osobnostních a jsem si plně vědom následků porušení ustanovení § 11 a následujících autorského zákona č. 121/2000 Sb., včetně možných trestněprávních důsledků vyplývajících z ustanovení § 152 trestního zákona č. 140/1961 Sb.

V Brně dne 26. října 2009

autor práce

Bibliografická citace

KUČERA, P. *Polarizační nedokonalosti světla v interferometrii*. Disertační práce. Brno: FEKT VUT v Brně, 2009, 94 stran.

Acknowledgement

I would like to express thanks to Prof. Otakar Wilfert, from University of Technology in Brno, who has been motivating me in both, scientific and private life.

I owe special debts to Prof. Friedemann Mohr, of Pforzheim University where all experiments were performed, who has been giving me inspiring ideas during the work.

List of abbreviations

AGC	Automatic Gain Control
DOP	Degree of Polarization
DUT	Device Under Test
FA	Fast Axis
FPGA	Field Programmable Gate Array
HWP	Half Wave Plate
HWSHD	Homodyne With Synthetic Heterodyne Demodulation
LED	Light Emitting Diode
LP	Linear Polarizer
NBP	Neutral Beamsplitter
OOK	On-Off Keying
PBS	Polarizing Beamsplitter
QWP	Quarter Wave Plate
QEP	Quantum Error Probability
SA	Slow Axis
SBC	Soleil-Babinet Compensator
SOP	State of Polarization

List of symbols

\hat{a}	Anihilation operator
\mathbf{E}	Electric field vector
\tilde{E}_x	A complex signal representing a component of the electrical field
e	Extinction coefficient of the linear polarizer
I	Irradiance (also called intensity)
\mathbf{J}	Jones matrix
\mathbf{k}	Wave vector
\mathbf{M}	Meuller matrix
P	Degree of polarization
P_s	Degree of pseudo-polarization
\hat{P}	Projection operator, matrix representation is used without operator symbol
Q, I	Quadrature signals
$(r), (i)$	Real and imaginary part
\mathbf{S}	Stokes vector
x, y, z, u, v	Cartesian coordinates
Δ	Used to denote difference between quantities (phase, distance)
φ	Mainly used for a phase shift between reference and signal beam
ω	Angular frequency of the field
λ	Wavelength of the light
$\hat{\rho}, \rho$	Density operator which define state of polarization and its matrix representation
$\langle \rangle$	Mean value notation, when the averaging is performed over time or spatial dimension is emphasized in the text
Tr	Matrix trace (the sum of the diagonal elements)
X^H	Hermite conjugation
\tilde{X}	Used to emphasize the complex quantity
$ x\rangle$	Dirac vector notation
$\langle x y\rangle$	Dot product

Contents

1	Introduction	1
1.1	<i>Motivation</i>	1
1.2	<i>Current state of the art</i>	1
1.3	<i>Dissertation's goals</i>	3
2	Influence of non-cooperative target	4
2.1	<i>Fully developed integrated speckle pattern</i>	5
2.2	<i>Depolarization by the target – deterministic approach</i>	6
2.3	<i>Measurements of the target's pseudo-depolarization</i>	9
2.4	<i>First order statistics of partly pseudo-polarized speckles</i>	12
2.5	<i>Integrated speckle pattern</i>	15
2.6	<i>Speckle reduction</i>	17
2.7	<i>Zoom lens in vibrometry</i>	25
2.8	<i>Multimode interference</i>	29
2.9	<i>Chapter summary</i>	31
3	Periodic deviations in vibrometry	32
3.1	<i>Measuring properties of retarders and beamsplitters</i>	32
3.2	<i>Influence of periodic deviations on quadrature signals</i>	38
3.3	<i>Reduction of periodic deviation</i>	42
3.4	<i>Experimental verification</i>	48
3.5	<i>Chapter summary</i>	51
4	Quantum description of optical devices	52
4.1	<i>Coherent and number states</i>	52
4.2	<i>Phase shifter and retarder</i>	53
4.3	<i>Mirror</i>	56
4.4	<i>Non-polarizing beamsplitter</i>	57
4.5	<i>Chapter summary</i>	61
5	Polarization imperfections in Polarimetry	62
5.1	<i>Laser as a light source</i>	63
5.2	<i>Using of non-ideal polarizers and depolarizations effects</i>	65
5.3	<i>Experimental results</i>	69
5.4	<i>Polariscope with only one QWP</i>	73
5.5	<i>Chapter summary</i>	74
6	Polarization properties in communication	75
6.1	<i>Nomenclature</i>	75
6.2	<i>Quantum measurement</i>	76
6.3	<i>On-off keying</i>	78
6.4	<i>Background radiation</i>	85
6.5	<i>Chapter summary</i>	90
7	Summary	91
8	References	92

1 Introduction

1.1 *Motivation*

This doctoral thesis is partly connected with a research project which was running at Pforzheim University and which was funded with financial support from an industrial partner and from the German Ministry of Research and Development in its FH3 program. The goal of this project was development of a laser vibrometer with a novel architecture: on the optical side based upon a polarization optical concept, and on the electronic side exploiting high-speed programmable electronic circuits (FPGAs). Background and main subject of the project is an optical laser vibrometer operating in a homodyne scheme. Homodyne schemes generally apply architectural concepts which generate a pair of quadrature signals which are then processed electronically to produce an output signal proportional to the speed of the measured target. Main emphasis of the dissertation is put on the optical part of the instrument, where a suitable architecture has to be defined, the properties of the required components have to be evaluated, and potential error sources resulting from non-ideal characteristics have to be determined.

1.2 *Current state of the art*

Interferometers are usually considered as belonging to either of two main families: heterodyne and homodyne interferometers [1].

Heterodyne interferometers have an architecture where the optical frequencies of the beams in measuring and reference path, respectively, are different. Superposition of these beams on the detector then produces, in the electrical domain, an IF signal with a frequency identical to the difference of both optical beams (so-called bias frequency). A movement of the target in the direction of the measuring beam then produces, through the well-known Doppler effect, a frequency shift on the measuring beam proportional to the target velocity. In case of a vibrating target the interferometer detector gives an output that is frequency modulated. The bias frequency mentioned above must be introduced in order to distinguish the sign of the target velocity. The preferred methods are to use an electro-optic device in one interferometer arm or to use a stabilized He-Ne laser whose output beam consists of two frequency components. The heterodyne technique is the most common approach in today's interferometric laser vibrometry.

Contrary to the competing heterodyne approach with its light beams with differing optical frequencies, the homodyne scheme for generating signals from an interferometric arrangement is based on the use of two optical beams of the same frequency. Homodyne interferometers detect the phase difference between the measuring and the reference arms. The sign of the target velocity is, in this case, determined from two signals in quadrature generated at the output of the vibrometer. Known methods for producing the required 90°-phase shift include the use of a beam

splitter with an absorbing metal coating [2] and the use of specific polarization-optical arrangements [3]. The second method, although it requires additional components to be included in the setup, is preferred to the first one. It is because of the non-stable behavior of the metal coating in the beam splitter and due to the loss of the energy which was reported in the literature.

As mentioned, the heterodyne concept requires expensive optical components such as a Bragg cell or a Zeeman Laser. On the side of the electrical signal extraction, it requires RF circuitry which is also quite costly and does not offer a high flexibility. In contrast to this, the homodyne-based concept that we chose avoids all these drawbacks both on the optical and on the electrical part of the architecture. Thus, our strategy reduces the optical complexity for the prize of higher signal processing demand. Based on the fact that today highly integrated signal processing hardware such as DSPs (Digital Signal Processors) or FPGAs solutions are much less expensive than in the past, this so called HWSHD (Homodyne With Synthetic Heterodyne Demodulation) strategy is therefore competitive to the classical usage of expensive optical components in the heterodyne concept.

In our investigations of this concept we have to focus on two main fields of problems. The first occurs with any interferometrical setup using light from a noncooperative target rather than a mirror. The light returning from the investigated target will be far from an ideal laser field with plane wave fronts. Instead, it will possess a statistical nature generally known as speckles [4]. As was stated previously, in the class of interferometers treated in the work, the required directional information is acquired by appropriately making use of the polarization properties of the light beams brought to interference. Consequently, we must pay special attention to the polarization of the backscattered field, and we cannot limit ourselves to the case of fully polarized speckle patterns (so called fully developed speckles [4]).

The influence of a fully developed speckle field on an interferometric signal was investigated in [5], [6] and [7]. There was assumed, however, that the phase of the backscattered field is correlated only within a single speckle and that the correlation between speckles is zero. In the mentioned publications was clearly demonstrating the spoiling effect of speckles on the visibility, i.e. on the quality of the interferometric signal.

The second difficulty arises due to polarization imperfection of components used in the optical part of interferometer. The errors due to these imperfections are called periodic deviations and were thoroughly studied in the dissertation [8] for the case of a heterodyne vibrometer. In [8] one can find analytical formulations of these errors. These errors, however, are in general difficult to analyze not for their mathematical complexity but for the finding the origin of these errors. Periodic deviations result not only from the inherent imperfections of components (non-ideal retardations, non-ideal transmission and reflection coefficients...) but also from the rotational misalignment of these components which is in practice hard to measure and control. Apart from the polarization-optical components, it must be kept in mind that the adjustment of all components (mostly mirrors and beamsplitters) has, above all, to satisfy several goals at once: measuring and reference beam must be brought to a good lateral and angular overlap in order to guarantee a good interference contrast (and to optimally exploit the available light power).

Periodic deviations also play an important role in another kind of measuring instrument, the so-called polarimeter. This instrument belongs to one of the oldest forms of interferometric measurements for determination of stress-induced birefringence in transparent materials. The recent technologies offer to produce micropolarizers arrays [9] and [10]. This brings a possibility of using these arrays in imaging [11] and in polarimetry. However, as can be found in [9], [10] these arrays have quite low extinction coefficients (between 100 and 300). Another difficulty is the exact orientation of transmission axes of micropolarizers. These two problems result again in the degradation of measuring performance due to the polarization imperfections of used micropolarizer arrays, and commonly used phase shift algorithms [12], [13] need to be refined.

The final part of the dissertation refers to polarization imperfections in optical communication with the emphasis on quantum optical communication. The part briefly summarizes published results in that field. Although this topic seems to be different from the main contents of the dissertation, some common features can be found. Namely, the function of the detector in communication schema is to determine which state was transmitted with the minimal probability of misdiagnosis. When polarization properties of light are used for encoding the information then a Wollaston prism fills the function of the detector and its imperfections increase the probability of misdiagnose. Some achieved results will be compared with papers from other authors [14], [15]. However a certain contradiction was found in [15].

1.3 Dissertation's goals

The main part of the dissertation is thus devoted to the problems that arise by using real optical components which possess non-ideal polarization properties. These problems are then in the dissertation analyzed, solved and obtained results are then applied to practical applications.

Let us summarize the main goals of the dissertation:

- Describe the influence of partly polarized speckle field on the interferometric signals.
- Find a solution how to reduce speckle effects resulting from the usage of non-cooperative target as the surface which is investigated by a vibrometer.
- Find the influence of periodic deviations on interferometric signals generated by vibrometer working in the homodyne concept and find the way how this spoiling influence can be eliminated.
- Study the influence of analyzer with low extinction coefficient and angular misalignment on measured retardation in polarimetry. Find an algorithm how the effect of low extinction coefficient can be eliminated from the current retardation determination procedure.
- Investigation of the influence of polarization imperfections on probability of misdiagnose in quantum optical communication.

2 Influence of non-cooperative target

In this section, we discuss the problems occurring in the interferometrical vibrometers (arrangements for high-resolution measurement of vibrating targets as in Fig. 2-1) which arise when the interferometer uses a conventional, so-called “non-cooperative” target rather than a mirror. In such arrangements, it is not generally possible to fix a mirror on the surface under consideration and as a result, the light returning from the target will be far from an ideal laser field with plane wave fronts. Instead, it will possess a statistical nature generally known as speckles [4]. This speckle field is then superimposed with the reference beam in order to generate an interferometric signal from which the information about the movement of the target can be derived by suitable electronic processing. Of course, the main aim in interferometry is then to achieve as high a visibility on the detector as possible. To achieve this, one needs to describe the speckle field in good detail.

In the class of interferometers treated here, the required directional information is acquired by making appropriate use of the polarization properties of the light beams brought to interference. Consequently, we must pay special attention to the polarization of the backscattered field, and we cannot limit ourselves to the case of fully polarized speckle patterns (so called fully developed speckles [4]) whose influence on an interferometric signal was investigated in [5], [6] and [7]. It was assumed, however, that the phase of the backscattered field is correlated only within a single speckle and that the correlation between speckles is zero. However, when suitable imaging optics is used, then the phase of the speckle field is fully deterministic as will be shown later in this chapter.

The main original author work in this chapter is the influence of a partly polarized speckle field on an interferometrical signal and a speckle reduction due to the using of a suitable imaging optics. The results were published in [16] and [17]. Next an idea of using a zoom objective in vibrometry is realized in the chapter. This enhances performances of the vibrometer, namely detected signal is independent of the target distance.

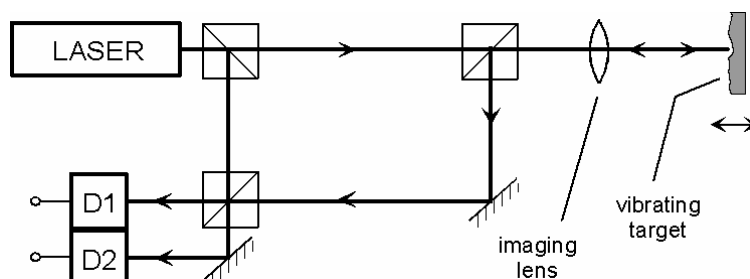


Fig. 2.1. Standard architecture of an interferometrical laser vibrometer.

2.1 Fully developed integrated speckle pattern

In [5] and [6], a probability density function for the field resulting from the superimposition of a fully polarized speckle field with a uniform reference field was derived. The results are interpreted using quantities I_0 and I_M which represent the background intensity and the modulation intensity respectively. Thence, the resultant intensity at a given point i at the detector can be written as

$$I_i = I_{0,i} + I_{M,i} \cos(\varphi_i + \Delta\varphi) = I_{R,i} + I_{S,i} + 2\sqrt{I_{R,i}I_{S,i}} \cos(\varphi_i + \Delta\varphi) \quad (2.1)$$

with I_R denoting reference beam intensity, I_S speckle intensity, $\Delta\varphi$ phase difference due to the different lengths of the interferometers arms and φ phase difference due to the scattering from the target. The previous quantities (except $\Delta\varphi$) are related to a specific point at the detector and we used discrete labeling rather than continuous for the reasons that will be clarified shortly. The reference field is deterministic while the speckle field obeys first order statistics as derived in [4].

However, a detector has a finite size and the detected intensity I_D is an integration of (2.1) over the detector area S and divided by the detector area to receive intensity. This is illustrated again in [4] for a single speckle field. The author there divides a detector into n elementary areas in which the intensity I_i is assumed to be constant (so called box-car approximation). In fact, it is a numerical integration

$$I_D = \frac{1}{S} \sum_{i=1}^n \left(I_i \frac{S}{n} \right). \quad (2.2)$$

The crucial point here is how to choose the number n . The first thought, to choose n as high as possible in order to achieve best precision of the integration, would extend the calculation time unreasonably high (because of the correlation of elementary surface areas). In fact, it is quite obvious that it is sufficient to select n identical to the number of speckles within the detector area. Then, the fields in these areas will be statistically independent of each other and (2.2) can be treated as a sum of n independent random variables which is simple to perform.

With this choice of n , the resultant statistics of the detected intensity is expressed quite simply, because in n , the correlation function of the speckle field is hidden. So the speckle field is represented by n only and a first order statistics.

For the details of the derivation of the I_M statistics, we refer to [5], [6] and for the experimental verification, to [7]. We only emphasize that the authors assumed the reference field to be uniform, the speckle field to be fully polarized, the phase of the speckle field to possess uniform distribution and finally the detector response to be constant over its area.

In the following sections, we will drop the assumption of a fully developed speckle pattern (so as to be able to also treat targets partly depolarizing the incident light) and the assumption of the uniform distribution of the phase (speckle reducing).

2.2 Depolarization by the target – deterministic approach

The influence of a partly polarized speckle field on an interferometric signal was investigated by the author in [16]. However, there was no distinction between the depolarization and so called pseudo-depolarization. The former deals with the familiar time average definition of the degree of polarization. The latter is related to the ensemble average over the surfaces with different microstructure. In this case, the light is in fact fully polarized at a particular point in the observer plane but the state of the polarization changes with the position. When this kind of light impinges on the polarizing sensitive detector of sufficiently large area, then this light appears partly polarized even though that there are no changes in time. This situation can be explained that the speckle field is viewed a superposition of large number of spatial modes. Each mode has a well defined polarization. The strength of the mode amplitudes varies with the position and hence the state of polarization is different from point to point. Note that the same effect can be observed in multimode fibers [18].

First, we will assume that a target partly depolarized the incident light which can be caused by some intrinsic time activity. Next, we assume that the light from the target is collimated by a lens (see Fig. 2.1) to form a narrow beam. Then, complex signals \tilde{E}_x , \tilde{E}_y represent the x and y -component of the electric field at a particular point in space. The spatial dependence of the components will be suppressed for now which corresponds to the situation of a point-like detector. Then, we can use the familiar definition of Stokes time-averaged, non-normalized parameters

$$\begin{aligned}
 \langle \tilde{E}_x(t)\tilde{E}_x^*(t) \rangle_T + \langle \tilde{E}_y(t)\tilde{E}_y^*(t) \rangle_T &= S_0 \\
 \langle \tilde{E}_x(t)\tilde{E}_x^*(t) \rangle_T - \langle \tilde{E}_y(t)\tilde{E}_y^*(t) \rangle_T &= S_1 \\
 \langle \tilde{E}_x(t)\tilde{E}_y^*(t) \rangle_T + \langle \tilde{E}_x^*(t)\tilde{E}_y(t) \rangle_T &= S_2 \\
 i\langle \tilde{E}_x(t)\tilde{E}_y^*(t) \rangle_T - i\langle \tilde{E}_x^*(t)\tilde{E}_y(t) \rangle_T &= S_3.
 \end{aligned} \tag{2.3}$$

Note, that the symbol \tilde{X} indicates a complex quantity and angle-bracket notation is used for statistical or longer-time averages (this employ ergodic assumption) with an appropriate lower index. The degree of polarization is defined as

$$P = \frac{\sqrt{S_1^2 + S_2^2 + S_3^2}}{S_0}. \tag{2.4}$$

The light from the target is then put in the form

$$\begin{pmatrix} S_{0T} \\ PS_{0T} \\ 0 \\ 0 \end{pmatrix} = (1-P) \begin{pmatrix} S_{0T} \\ 0 \\ 0 \\ 0 \end{pmatrix} + P \begin{pmatrix} S_{0T} \\ S_{0T} \\ 0 \\ 0 \end{pmatrix} \tag{2.5}$$

where we introduced the index “ T ” to distinguish the target field from the reference field which will be later superimposed. The assumption that the scattered light is partially linearly polarized constitutes no loss of generality, because one can always choose a coordinate system, in which the described light has the form of (2.5).

The next step is to express (2.5) for both electric field components

$$\begin{aligned}\tilde{E}_{xT}(t) &= \sqrt{\frac{S_{0T}}{2}}(1-P)\tilde{A}_{xT}(t) + \sqrt{S_{0T}P}\tilde{A}_{xR}(t) \\ \tilde{E}_{yT}(t) &= \sqrt{\frac{S_{0T}}{2}}(1-P)\tilde{A}_{yT}(t)\end{aligned}\quad (2.6)$$

where the complex analytic signal \tilde{A}_{xT} is in the general form

$$\tilde{A}_{xT}(t) = \tilde{a}_{xT}(t)\exp(-i\bar{\omega}t) \quad (2.7)$$

where $\tilde{a}_{xT}(t)$ is slowly varying complex envelope and $\bar{\omega}$ is the mean angular frequency. Similarly \tilde{A}_{yT} . Finally \tilde{A}_{xR} has the form

$$\tilde{A}_{xR}(t) = \exp(-i\bar{\omega}t) \quad (2.8)$$

and represents analytic signals describing the laser source characterized by the mean angular frequency $\bar{\omega}$. Here we suppressed the time dependent complex envelope in accord with the assumption of the monochromaticity of the source (the laser source is assumed).

In physical words equation (2.6) means that the scattered light is divided into one part which is unpolarized and independent of the illuminating beam and another which is polarized and maintains the history of the illuminating source beam. The analytical signals satisfy (these demands follow from eqns (2.3) and (2.5))

$$\begin{aligned}\langle \tilde{A}_{xT}(t)\tilde{A}_{xT}^*(t) \rangle &= \langle \tilde{A}_{yT}(t)\tilde{A}_{yT}^*(t) \rangle = \langle \tilde{A}_{xR}(t)\tilde{A}_{xR}^*(t) \rangle = 1 \\ \langle \tilde{A}_{xT}(t)\tilde{A}_{yT}^*(t) \rangle &= \langle \tilde{A}_{yT}(t)\tilde{A}_{xT}^*(t) \rangle = 0 \\ \langle \tilde{A}_{xT}(t)\tilde{A}_{xR}^*(t) \rangle &= \langle \tilde{A}_{yT}(t)\tilde{A}_{xR}^*(t) \rangle = 0\end{aligned}\quad (2.9)$$

where in the last line of (2.9) was assumed that $\tilde{a}_{xT}(t)$ is zero mean complex-valued random process.

At the detector the field from the target (2.6) is superimposed with the reference beam. We will assume that the field of the reference beam is linearly polarized in x -direction. Thus, it can be described by a single component

$$\tilde{E}_{xR}(t) = \sqrt{S_{0R}}\tilde{A}_{xR}(t) \quad (2.10)$$

where the Stokes parameter S_{0R} characterizing the intensity of the reference beam was introduced. The components of the superimposed field are then

$$\begin{aligned}\tilde{E}_x(t) &= \left(\sqrt{\frac{S_{0T}}{2}}(1-P)\tilde{A}_{xT}(t) + \sqrt{S_{0T}P}\tilde{A}_{xR}(t) \right) \exp(i\Delta\varphi) + \sqrt{S_{0R}}\tilde{A}_{xR}(t) \\ \tilde{E}_y(t) &= \sqrt{\frac{S_{0T}}{2}}(1-P)\tilde{A}_{yT}(t)\exp(i\Delta\varphi)\end{aligned}\quad (2.11)$$

where the phase difference $\Delta\varphi$ between the two interferometer arms was introduced. Using (2.3) and (2.9) we obtain the resulting Stokes vector (constituted of an unpolarized and a polarized part) as

$$\mathbf{S} = S_{0T}(1-P) \begin{pmatrix} 1 \\ 0 \\ 0 \\ 0 \end{pmatrix} + [S_{0T}P + S_{0R} + 2\sqrt{S_{0R}S_{0T}P} \cos(\Delta\varphi)] \begin{pmatrix} 1 \\ 1 \\ 0 \\ 0 \end{pmatrix}. \quad (2.12)$$

Next, we note that when the rough surface is illuminated by quasimonochromatic light (the coherence length of the light is greater than the maximum path length difference encountered in the experiment), the scattered light cannot be modeled as an ergodic random processes and one has to distinguish the ensemble and time average.

If the surface has no in-plane velocity component and if there is no time activity of the material, then the modulus of the complex coherence factor is unity (for the time-averaged definition of the spatial coherence). Hence, the rough surface does not reduce the coherence of the light, since the spatial structure of the surface (modeled as a stationary random process) does not change with time. However, a certain class of the targets can introduce pseudo-depolarization. When this kind of light is brought to interference with the reference beam, the interference signal is reduced due to the finite area of the detector.

Let us introduce the Stokes ensemble-averaged parameters defined in similar way to (2.3) where the time averages are replaced by ensemble averages (also known as statistical averages). These parameters are related to the degree of pseudo-polarization P_s . The overlap between the reference beam polarization and the scattered beam with degree of pseudo-polarization P_s is $(1+P_s)/2$. In this case, the Stokes vector of the detected interferometric signal is given by

$$\mathbf{S} = 2\sqrt{\frac{S_{0R}S_{0T}}{2}(1+P_s)} \cos(\Delta\varphi) \begin{pmatrix} 1 \\ 1 \\ 0 \\ 0 \end{pmatrix}_s. \quad (2.13)$$

Hence, even when the backscatter light is completely pseudo-depolarized, the interference fringes are visible. This is illustrated in Fig. 2.2 where normalized interferometric signal is depicted as a function of degree of polarization and pseudo-polarization, respectively.

We defer discussion of experimental verification of formula (2.13) to the next section which deals with measurements of the degree of pseudo-polarization which are needed in order to verify equation (2.13). For current discussion we only note that the degrees of pseudo-polarization of all used targets are 0.21, 0.6, 0.8, 0.93 and 0.97 and were obtained by experimental means discussed further.

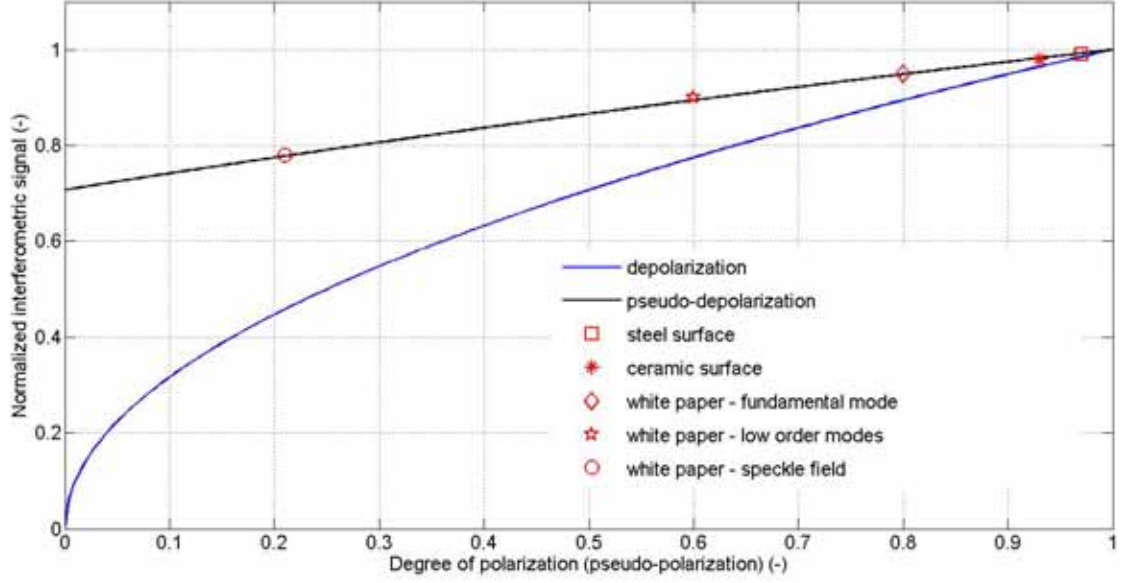


Fig. 2.2. Normalized interferometric signal as a function of degree of polarization (dashed line) and pseudo-polarization (solid line).

2.3 Measurements of the target's pseudo-depolarization

We start with presenting Mueller matrices of steel surface and white paper which we measured using a typical ellipsometer arrangement (see [37] for instance). White paper, in the first approximation, behaves like Lambertian surface, which scatters light uniformly into all hemispheric directions and pseudo-depolarize in random fashion. On the other hand, steel surface strongly reflects light specularly and does not depolarize incident light. The normalized matrices for normal incidence and for wavelength 633 nm are

$$\mathbf{M}_S = \begin{bmatrix} 1.00 & 0.00 & -0.01 & 0.00 \\ 0.01 & 1.00 & 0.02 & 0.01 \\ 0.00 & -0.02 & -0.99 & 0.12 \\ -0.01 & -0.02 & -0.08 & -0.94 \end{bmatrix} \quad \mathbf{M}_P = \begin{bmatrix} 1.00 & 0.10 & -0.06 & 0.00 \\ 0.12 & 0.19 & 0.07 & 0.02 \\ 0.00 & -0.05 & -0.18 & 0.12 \\ -0.02 & 0.03 & -0.08 & -0.19 \end{bmatrix}. \quad (2.14)$$

The matrices fulfill so called over-polarization and over-gained conditions [38] which are usually tested for measured Mueller matrices and are necessary conditions for a physically realizable medium. Mueller matrix also fulfilled condition [38] to have an equivalent Jones matrix.

A good understanding of Mueller matrixes was presented in [37]. The matrix in the principal frame (s and p -polarization are the principal axes in the case of a surface) can be express as

$$\mathbf{M} = \begin{pmatrix} 1 & P_x & 0 & 0 \\ P_x & 1-2D_v & 0 & 0 \\ 0 & 0 & P_y & P_z \\ 0 & 0 & -P_z & P_y \end{pmatrix} \quad (2.15)$$

where P_x turns unpolarized light into linearly polarized light, circular polarization P_z turns linear polarized light into circularly polarized light, the part which preserves the polarization of incident light is P_y and D_v is the cross-polarized scattering which is a part of depolarization. The degree of polarization (pseudo-polarization) of a response is then [37]

$$P = \sqrt{P_x^2 + P_y^2 + P_z^2} \quad (2.16)$$

and depolarization is defined in [37] as

$$D \equiv 1 - P = D_u + D_v \quad (2.17)$$

where D_u is defined as the self-correlation of the incoherent copolarized response relative to all polarizations. In our case we approximately have $P = 0.97$ for steel surface and $P = 0.23$ for white paper, respectively.

In Fig. 2.3, a measurement setup suitable for investigation of polarization behavior of targets in interferometry is shown. This setup allow a sharp focusing of the illuminated beam on the target which can lead to eliminating of higher spatial modes in the backscattered field as will be shown later. The next figure 2.4 can be interpreted as the measurement of linear degree of pseudo-polarization. Moreover, from Mueller matrices one can see negligible amount of optical activity. Hence, linear degree of pseudo-polarization corresponds in good approximation to the overall degree of pseudo-polarization. Measurement data points were obtained for two different surfaces. Smooth ceramic surface (black curve), which strongly scatters light in specular direction and white paper (blue) which in the first approximation behaves like Lambertian scatterer. Ceramic surface has scattering properties similar to the steel surface only with lower reflectance which is close to the reflectance of the paper.

The red curve corresponds also to the white paper, but in this case, the illuminated beam was focused sharply in order to reduce higher spatial modes, i.e. speckles. The speckle reduction is treated in detail in section 2.6.

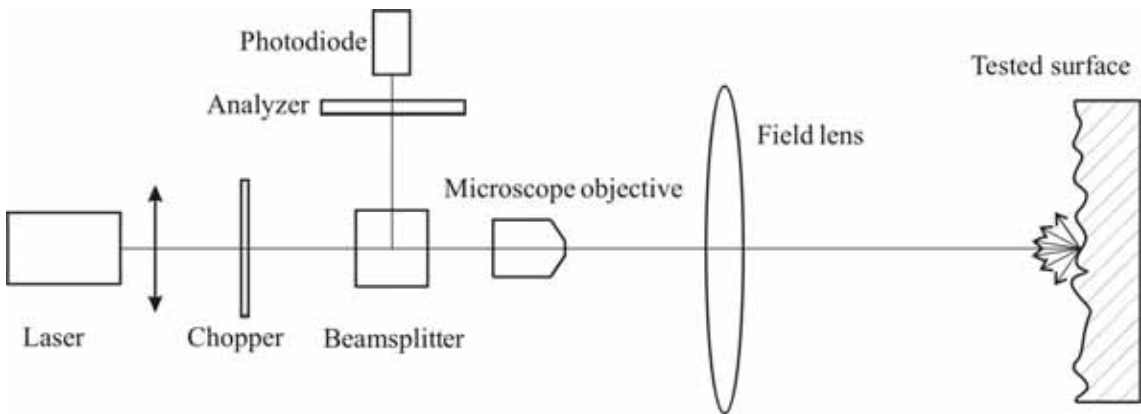


Fig. 2.3. Measurement setup for determination of linear pseudo-depolarization of tested surfaces.

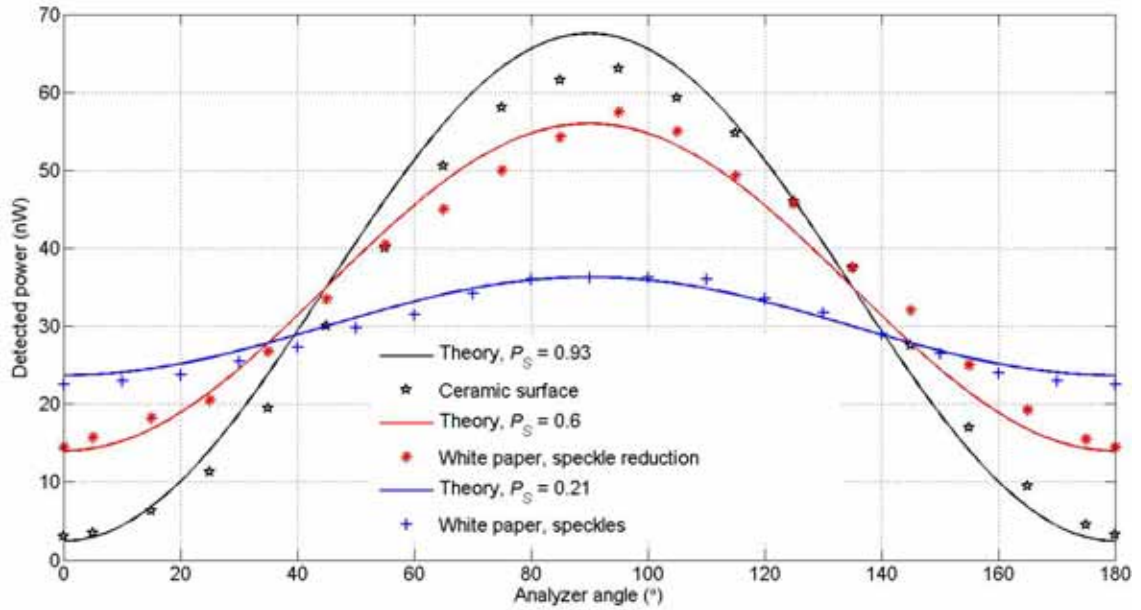


Figure 2.4. Detected scattered power from a target illuminated by a linearly polarized beam (633 nm, 1.2 mW) as a function of analyzer angle.

However, the speckle reduction was not perfect because we used slightly different imaging optics from that which was used in the final arrangement of the vibrometer. The optics used in this case were anti-reflection coated but the optics did not enable focusing sharp enough to eliminate all higher modes. When we used the same imaging optics like in the final arrangement of the vibrometer, then the reflected light from microscope objective exceeded the light of interest, the one scattered from target. This was not a problem in the vibrometer because reflected light from lenses was eliminated by polarization means. The irradiance pattern of the target field formed at the detector looked as it is depicted in the second-last figure in Fig. 2.15 on page 24 rather than in the last one.

The important thing is that degree of pseudo-polarization increase with decreasing number of spatial modes in the backscattered field. This confirms the analogy with optical fiber. Indeed, when an illuminating beam is focused sharply on the target, the fundamental mode dominates in the backscattered field and has properties of the original beam (polarization, direction of the propagation only opposite in sign) which caused the disturbance. It is remarkable to note that the diameter of the illuminated target area in the speckle reduction mode is comparable with the diameter of the core of single-mode fiber. As was stated before, a more detailed analysis of the problem is deferred to section 2.6.

The final note belongs to power consideration. For the ceramic surface and white paper in speckle reduction mode, the detected area was same. For the case of white paper in the speckle mode, the area of detector was enlarged approximately 10 times, hence the irradiance of speckle field is reduced by factor 10. This is in good agreement with results shown in section 2.6, namely see Fig. 2.10 and 2.12 where irradiance patterns of backscattered field on the detector were obtained using computer simulation.

In order to verify formula (2.13) measurements with different targets were performed. We used a simple interferometer arrangement shown in Fig. 2.1. No polarization components were involved in the setup as was the case of final vibrometer arrangement shown further. The first two measurements points in Fig. 2.2 correspond to

a steel metal surface and ceramic surface used as the targets. The three remaining measurements were performed using a white paper as the target. For each case a different imaging optics was used in order to control field backscattered from the paper. Note that the measurement point which corresponds to the case $P_S = 0.8$ was in fact obtained by inverse using of (2.13) hence degree of pseudo-polarization was deduced from the measured interferometric signal. This was done because that in the direct measurement procedure shown in Fig. 2.3 used for the measurement of DOP different imaging optics was used as was mentioned before. The reflected light from microscope objective in the interferometrical arrangement in Fig. 2.1 (in this setup objective was not anti-reflection coated) caused no problems because it was not modulated (only target was oscillating).

From measurement results depicted in Fig. 2.2, it is then reasonable state that the field at a single point on the detector can be indeed described by (scattered field was collimated with lens so longitudinal component of the field vector is zero)

$$\mathbf{E}(t) = e^{j\omega t} \sum_n E_{0n} \begin{pmatrix} \cos \chi_n \\ \sin \chi_n e^{j\varphi_n} \end{pmatrix} \quad (2.18)$$

where polarization of modes can differ (this depends on the material properties of the scattering media). Through substitution of (2.18) into (2.3) and using definition of degree of polarization (2.4), one obtains $P = 1$. However, the mode amplitudes in (2.18) are functions of spatial coordinates which define detector area which is of finite size.

Now, we calculate degree of pseudo-polarization which means using ensemble averages in the definition of Stokes parameters. We will assume that polarimetric parameter χ is uniformly distributed for the case of complete pseudo-depolarization. Stokes parameter S_1 is then

$$\begin{aligned} S_1 = \left\langle \sum_n |E_{0n}|^2 \cos^2 \chi_n + \sum_{n,m \text{ for } n \neq m} E_{0n} E_{0m}^* \cos \chi_n \cos \chi_m - \right. \\ \left. - \sum_n |E_{0n}|^2 \sin^2 \chi_n - \sum_{n,m \text{ for } n \neq m} E_{0n} E_{0m}^* \sin \chi_n \sin \chi_m e^{j(\varphi_n - \varphi_m)} \right\rangle_S = 0. \end{aligned} \quad (2.19)$$

Similar results hold for the remaining Stokes parameters. Hence degree of pseudo-polarization $P_S = 0$.

2.4 First order statistics of partly pseudo-polarized speckles

Several numerical models for describing speckles are reported in literature [19]. According to these, the speckle effect is a function of the roughness of the scattering surface, the correlation function of the surface and the size of the illuminated area. Quite often, a different kind of target requires using a different model in order to properly describe the speckle pattern produced by the target.

The most basic models view the rough surface of the target as amplitude or phase screens which perturbed the illuminating beam. Optical imperfection due to these perturbing screens can be modeled either as a collection of point scatterers or by a perturbation transmission function which is expressed as a superposition of sinusoidal spatial frequency components in the transverse direction.

In Fig. 2.5, two speckle patterns (cycle averaged optical intensity) with degree of pseudo-polarization 0.2 and 1 are shown. The patterns were produced by a computer simulation but experimentally, the former can be observed by illuminating a matt white surface (white paper for instance) and the latter by illuminating a metal surface.

In the simulation, the rough surface was assumed to be consisting of a large number of independently radiating scatterers. Then, the field of each scatterer was decomposed into unpolarized and polarized part. Namely, the former part is expressed as

$$E_{x_i}^{(u)} = E_i \sqrt{\frac{1-P_S}{2}} \exp(i2\pi\varphi_{x_i}^{(u)}), E_{y_i}^{(u)} = E_i \sqrt{\frac{1-P_S}{2}} \exp(i2\pi\varphi_{y_i}^{(u)}) \quad (2.20)$$

where E_i is amplitude of the illuminating laser beam at the point where the scatter is considered, $\varphi_{x_i}^{(u)}$ and $\varphi_{y_i}^{(u)}$ are phases for both components which possess uniform distribution over i and are non-correlated. Polarized part was simulated as

$$E_{x_i}^{(p)} = E_i \sqrt{\frac{P_S}{2}} \exp(i2\pi\varphi_{x_i}^{(u)}), E_{y_i}^{(p)} = E_{x_i}^{(p)} \exp\left(i\frac{\pi}{2}\right) \quad (2.21)$$

where $\varphi_{x_i}^{(u)}$ is uniformly distributed. The choice of the circularly polarized light is just a basis choice. The total field in the plane of the target is then given by a superposition of (2.20) and (2.21). The Huygens principle for each component was then used to obtain a field in the observer plane.

The probability density functions of intensity (expressed in the number of counts where a given parameter lies in a particular interval) are shown in Fig. 2.6. Also shown is the analytically obtained density function of the intensity based upon intensity basis rather than amplitude basis [4].

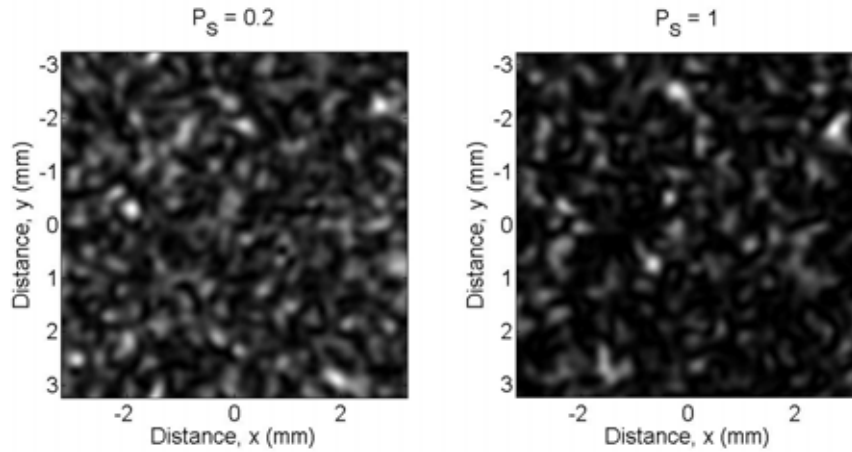


Fig. 2.5. Speckle patterns produced by scattering a laser light by a white paper ($P_S = 0.2$) and a metal surface ($P_S = 1$).

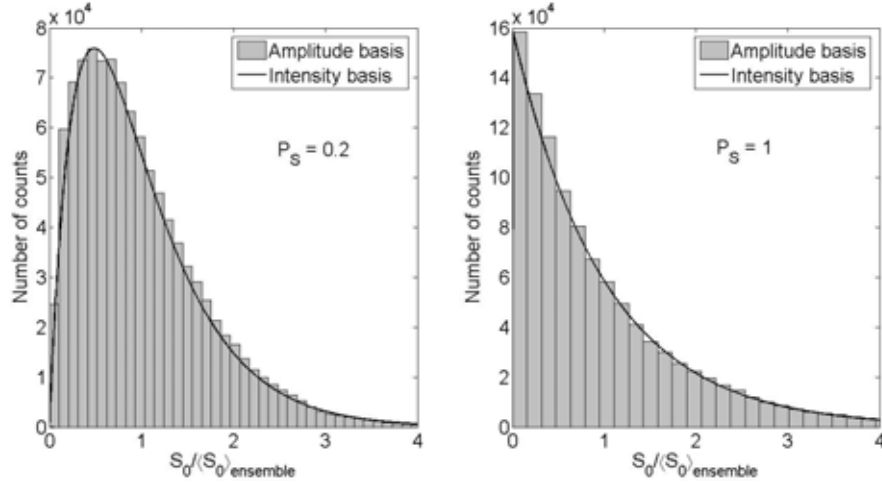


Fig. 2.6. The first order statistics of the intensity (irradiance).

The remaining Stokes parameters are depicted in Fig. 2.7. The polarization of the illuminating beam was assumed to be circular. The S_1 statistics is symmetric with its mean value being approximately 0. For the metal, it has the shape of a Dirac function (note the fine scale of the x -axis). The departure from the “true” Dirac function is due to the simulation imperfection. The S_2 statistics has the same form as S_1 statistics and are not shown here. Finally, S_3 statistics for the metal scatterer are the same as for S_1 statistics due to the fact that the metal does not depolarize the light. The S_3 statistics in the case of the paper is asymmetric with a mean value of 0.2.

This result can be compared with [20]. There, an analytic expression is given for the statistics of Stokes parameters of a chaotic source. This source is simulated by a large sum of random phasors, thus in the exactly same way (but in a time domain) as a speckle field considered there.

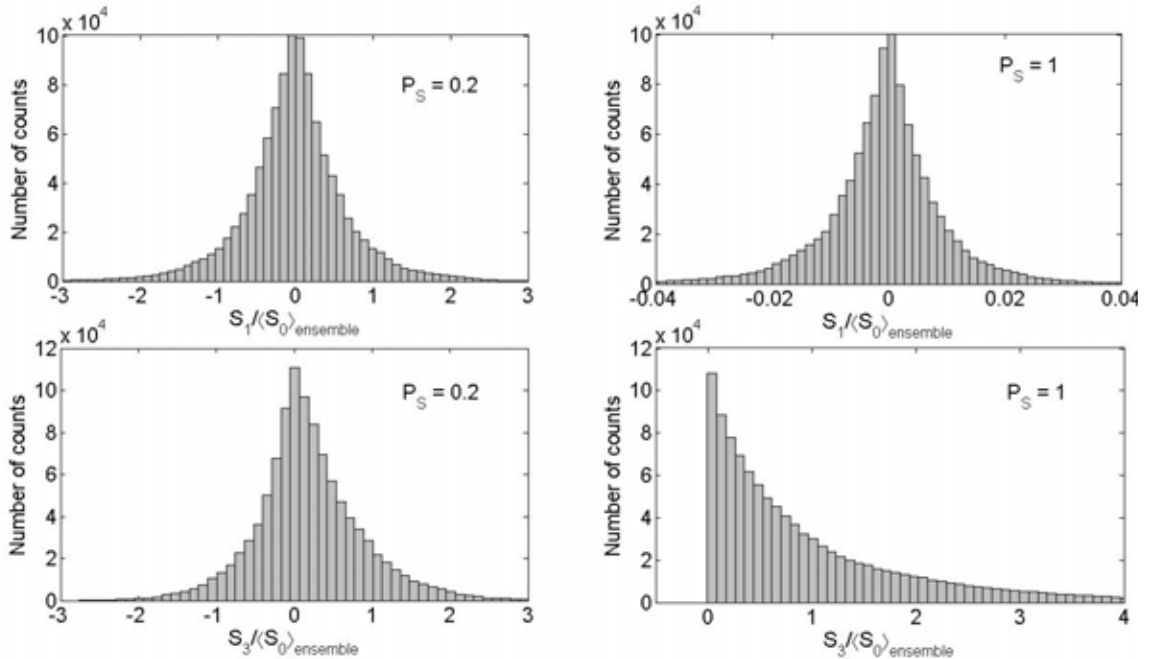


Fig. 2.7. The first order statistics of Stokes parameters.

2.5 Integrated speckle pattern

In section 2.1, we had shown how the statistics of the modulation power can be obtained under the assumptions of a detector with finite aperture and with a fully developed (polarized) speckle field. The latter assumption will be dropped now. Through the section, it will be assumed that the scattered light is partly pseudo-depolarized and all averages appearing in the section denote ensemble averaging. Then the interferometric signal (modulation intensity), at a given point at the detector, is given by (2.13).

First we combine the method illustrated in section 2.1 (the I_M statistics for a fully developed speckle pattern) and the results from section 2.2. Namely, we assume that the intensity at a given elementary area i at the detector is described by the formula

$$\begin{aligned} I_i &= I_{0,i} + I_{M,i} \cos(\varphi_i + \Delta\varphi) = \\ &= I_{R,i} + I_{S,i} + 2\sqrt{I_{R,i}I_{S,i}} \frac{(1+P_S)}{2} \cos(\varphi_i + \Delta\varphi). \end{aligned} \quad (2.22)$$

To keep the information concerning the phase of the field, the convention to work with the complex representation of the modulated intensity is adopted. The real and imaginary part of modulation intensity are then expressed as

$$I_M^{(r)} = \frac{1}{S} \sum_{i=1}^n \left(I_{M,i}^{(r)} \frac{S}{n} \right) = \frac{1}{S} \sum_{i=1}^n \left(2\sqrt{I_{R,i}I_{S,i}} \frac{(1+P_S)}{2} \cos(\varphi_i + \Delta\varphi) \frac{S}{n} \right) \quad (2.23a)$$

and

$$I_M^{(i)} = \frac{1}{S} \sum_{i=1}^n \left(I_{M,i}^{(i)} \frac{S}{n} \right) = \frac{1}{S} \sum_{i=1}^n \left(2\sqrt{I_{R,i}I_{S,i}} \frac{(1+P_S)}{2} \sin(\varphi_i + \Delta\varphi) \frac{S}{n} \right). \quad (2.23b)$$

The aim is to establish the density probability function of the complex modulation intensity.

The reference beam is assumed deterministic and uniform over the detector area. Hence, all of the randomness in (2.23) is due to the speckle field formed by the target.

The first order statistics of the partly pseudo-polarized speckle field was presented in section 2.4. The first order statistic of the intensity was obtained by considering that the resultant speckle pattern can be decomposed into two independent fully developed speckle patterns. These patterns possess same statistic, namely negative exponential probability density function, but differ in their mean values which are given by

$$\begin{aligned} \langle I_X \rangle_S &= \frac{1}{2} \langle S_{0T} \rangle_S (1+P_S) \\ \langle I_Y \rangle_S &= \frac{1}{2} \langle S_{0T} \rangle_S (1-P_S) \end{aligned} \quad (2.24)$$

where we used angle bracket to denote ensemble averaging and the lower index will be suppressed in the rest of the section. The probability density function of the resultant speckle intensity $I_{S,i}$ is then given by convolution of both negative exponential probability functions which yields to

$$p(I_{S,i}) = \frac{1}{P_S \langle S_{0T} \rangle} \left\{ \exp \left[-\frac{2I_{S,i}}{(1+P_S) \langle S_{0T} \rangle} \right] - \exp \left[-\frac{2I_{S,i}}{(1-P_S) \langle S_{0T} \rangle} \right] \right\}. \quad (2.25)$$

The statistic of the complex modulated intensity $\tilde{I}_{M,i}$ is obtained by using rules of transformations of random variables

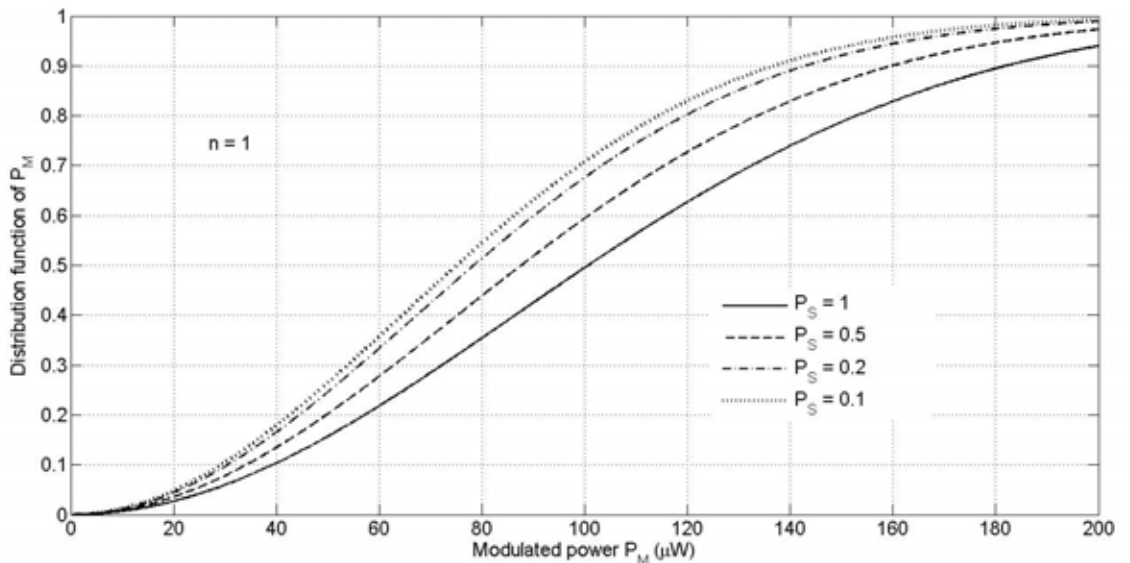
$$\begin{aligned} I_{M,i}^{(r)} &= 2\sqrt{I_R I_{S,i} \frac{(1+P_S)}{2}} \cos \varphi_i \\ I_{M,i}^{(i)} &= 2\sqrt{I_R I_{S,i} \frac{(1+P_S)}{2}} \sin \varphi_i \end{aligned} \quad (2.26)$$

where we suppressed index i at reference intensity (assumed constant over the detector) and constant phase difference $\Delta\varphi$ which has no effect on the resulting statistics. To complete the task we recall that the probability density function of the phase is assumed to be uniform and the phase is assumed to be independent of intensity. The probability density function of the complex modulated intensity $\tilde{I}_{M,i}$ is then given by

$$\begin{aligned} p(I_{M,i}^{(r)}, I_{M,i}^{(i)}) &= \frac{1}{2\pi \cdot I_R (1+P_S) P_S \bar{S}_{0T}} \times \\ &\times \left\{ \exp \left[-\frac{(I_{M,i}^{(r)})^2 + (I_{M,i}^{(i)})^2}{I_R (1+P_S)^2 \bar{S}_{0T}} \right] - \exp \left[-\frac{(I_{M,i}^{(r)})^2 + (I_{M,i}^{(i)})^2}{I_R (1-P_S)(1+P_S) \bar{S}_{0T}} \right] \right\}. \end{aligned} \quad (2.27)$$

Finally, to obtain statistics for the resulting modulated intensity \tilde{I}_M (see left parts of equations (2.23)), one needs to perform convolution of n independent random variables characterized by (2.27).

Figure 2.8 shows probability distribution functions for modulated power for two different values of n . In this case, we preferred distribution functions to density functions because of the possibility of directly reading the mean values and we also interpreted the results in terms of modulated power rather than intensity. Figures were obtained by numerical calculation and the reference power is taken to be 370 μW and the speckle power 10 μW .



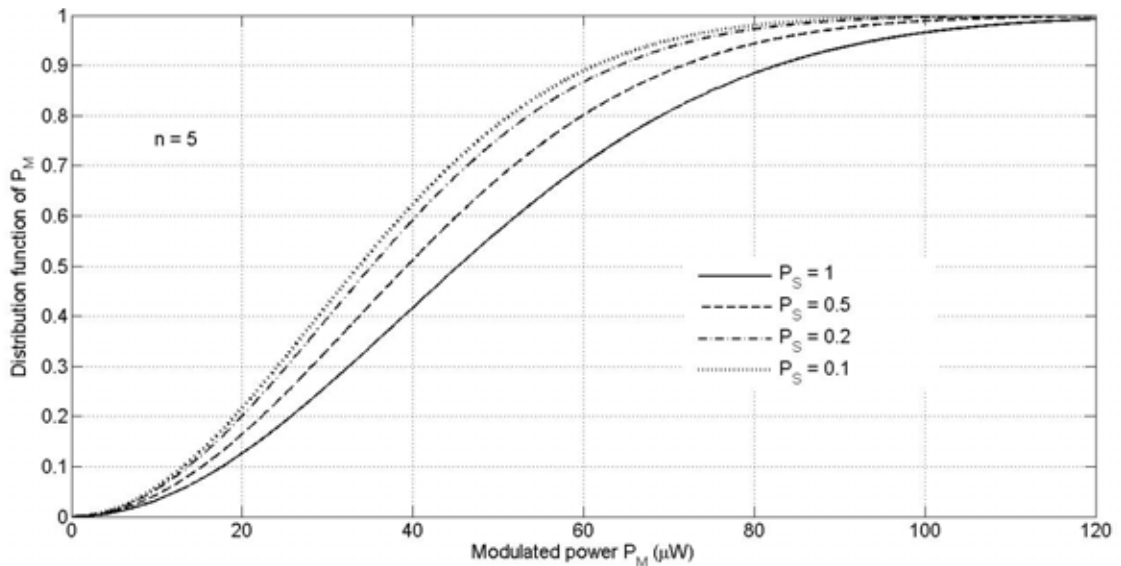


Fig. 2.8. Distribution functions of modulated power for three values of n . Target pseudo-depolarized incident beam.

The curves in Fig. 2.8 for fully developed speckles can be compared with [7] where experimental verification was shown. Next, from Fig. 2.8 one can see that the mean value of the interferometric signal (also denoted like modulated power) behaves like in Fig. 2.2.

2.6 Speckle reduction

In the previous section, it was shown that collecting more power scattered by the target reduces the contrast of the interference signal (modulated power). This spoiling effect is due to the stochastic nature of the speckles. However, with suitable imaging optics and for small oscillation amplitude of the target (order of 50 microns), the stochastic nature of the speckles can be reduced even for rough surfaces.

The optimization of interferometers which operate with large displacement amplitude of the target (in the speckle mode) can be found in [21]. Here we are considering small vibration amplitudes (a situation which is normally encountered in laser vibrometry; large amplitude vibrations would often be measured with some alternative, less costly instrumentation).

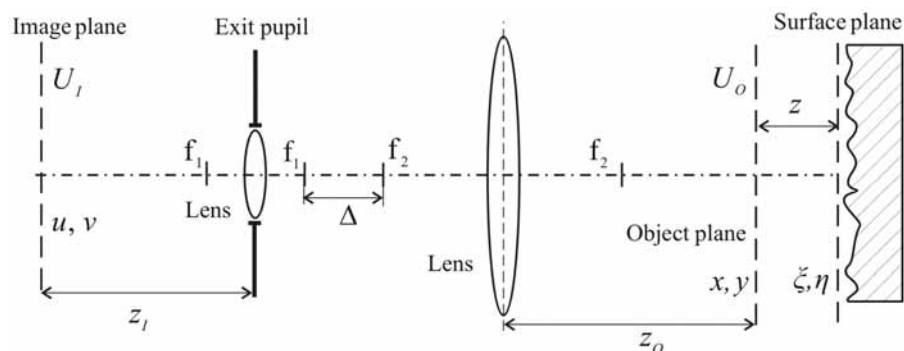


Fig. 2.9. Imaging optics of an interferometer.

Let us assume imaging optics which is depicted in Fig. 2.9. The optics serve both for focusing the laser beam on the target and for collecting the backscattered light. The position of the second lens can be positioned by parameter Δ . The amount of the light that reaches the detector placed in the image plane is determined by the aperture stop which coincides with the exit pupil.

It is assumed that waves emitted by different surface elements are focused to form a parallel light beam and that the observed light has a fixed polarization, so that the electric field can be added algebraically. The total electric field produced by a large number of radiating surface elements on the detector is then [22]

$$\tilde{U}_2(u) = \exp(-ikL_0) \int \tilde{K}(u, \xi) \tilde{U}_1(\xi) d\xi \quad (2.28)$$

where the kernel is defined as

$$\tilde{K}(u, \xi) = \sqrt{\frac{i}{B\lambda}} \exp\left[-i\frac{\pi}{B\lambda}(A\xi^2 - 2\xi u + Du^2)\right] \quad (2.29)$$

where the total optical path length through the paraxial $ABCD$ system for a ray traveling exactly on the axis is denoted by L_0 . Equation (2.28) represents Huygens' integral in one transverse dimension for wave propagating all the way through the paraxial system, from plane z_1 to plane z_2 . These planes correspond to the surface plane and the imaging plane where the detector is placed (cf. Fig. 2.9). Note that eq. (2.28) tacitly assumes that the system between the two planes does not contain elements which dramatically reduce the amount of transmitted light (aperture stops). If this is the case, the system is then viewed as a collection of subsystems where the previous statement is satisfied and (2.28) is used for input-output relation of each subsystem.

From the geometrical optics point of view, the general relation between the object and image plane of an optical system in the ray-transfer matrix formalism and paraxial approximation is given by

$$\mathbf{T} = \begin{bmatrix} M & 0 \\ C & M^{-1} \end{bmatrix} \quad (2.30)$$

where M stands for a magnification of the system and C for a general system can not be closely determined at this point. In the case of Fig. 2.9 matrix \mathbf{T} has the form

$$\mathbf{T} = \begin{bmatrix} M_1 M_2 & 0 \\ \left(-\frac{M_2}{f_1} - \frac{1}{M_1 f_2}\right) & (M_1 M_2)^{-1} \end{bmatrix} \quad (2.31)$$

where M_1 (M_2) stands for the magnification of the first (second) lens. The relation between the absolute values of object and image field is given by

$$|\tilde{U}_i(u, v)| = \frac{1}{|M|} \left| \tilde{U}_o\left(\frac{u}{M}, \frac{v}{M}\right) \right| \quad (2.32)$$

where u , v are coordinates in the image plane. When the target distance from the object plane (denoted as z in Fig. 2.9) is much larger than the illuminated area of the target, the phase of the backscattered field is deterministic. In fact, the phase can be approximated by a radius of curvature which is identical with the value of z .

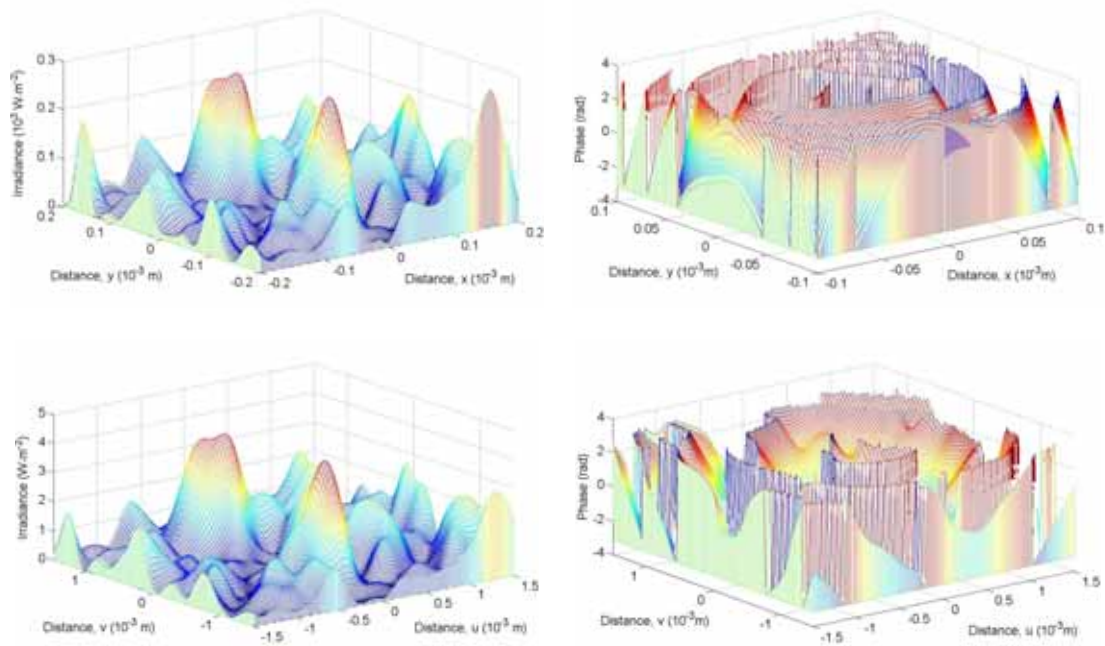


Fig. 2.10. The upper part: irradiance and phase of the backscattered field in the object plane ($z = -3.6$ mm, radius of illuminated area $w = 25 \mu\text{m}$), the lower part: irradiance and phase of the backscattered field in the image plane.

The series of figures in Fig. 2.10 show the field in the object plane and in the image plane. Field in the object plane was obtained by using the Huygens' integral for free space propagation and the field in the image plane was calculated by using (2.28). Next, it was assumed that the target does not absorb the incident light which was produced by He-Ne laser with the output power 1mW. The laser light was collimated on the target to produce the spot of radius 25 microns.

One can see from Fig. 2.10 that the phase of the field can be approximated with the radius of curvature equal to z . The extent of the phase distortion apparent in Fig. 2.10 is given by the ratio z/w . In other words, to remove stochastic nature of the phase, one needs to use the imaging optics with the object plane situated sufficiently far from the target surface in comparison with the width of the spot of the illuminating beam.

Next, a photograph of the speckle field in the detector plane is shown in Fig. 2.11 on the left. The interferometric setting was the same as used in the computer simulation with results shown in Fig. 2.10.

Finally, the interference fringes, obtained by superimposing the speckle field with the uniform reference beam, are shown in Fig. 2.11 on the right. This photograph confirms that the phase of the speckle field formed by rough surface can be described in the deterministic way when certain conditions are met. In the photograph, there is also apparent the phase distortion shown at the bottom of Fig. 2.10.

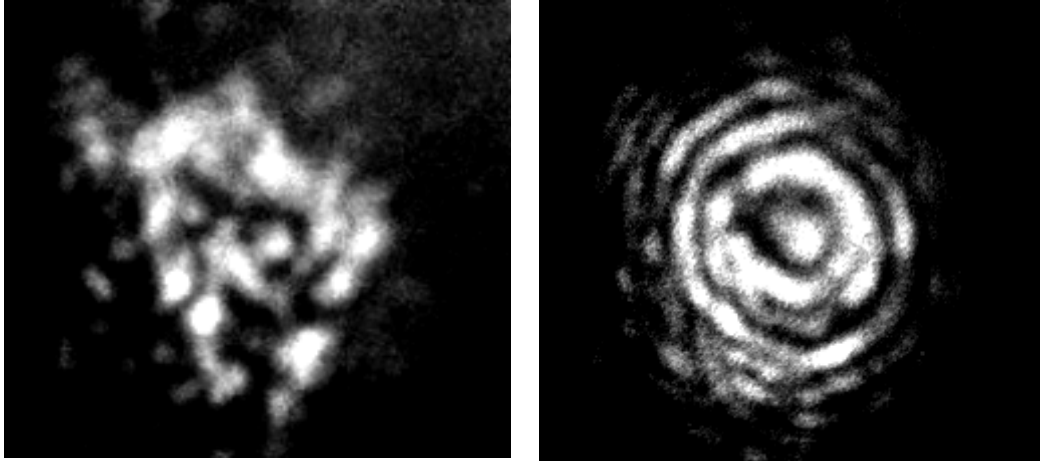


Fig. 2.11. A photograph of backscattered field in the detector plane (left) and interference fringes formed after superimposing with the reference beam (right).

One can see that the irradiance pattern in Fig. 2.10 is highly overmoded and that the phase of the speckles is deterministic. The speckle effect in the irradiance pattern can be reduced considerably so that only the fundamental mode will survive. This can be achieved by focusing sharply the laser beam on the target. The field for this case is shown in Fig. 2.12.

The difference in the irradiance patterns between Fig. 2.12 and 2.10 can be explained in the following way: The rough scattering surface in the case of Fig. 2.10 was simulated as a large number of radiating elements. The intensity pattern over the surface was assumed to be Gaussian, and the phases of the radiating elements were assumed uniformly distributed and uncorrelated. Hence, the statistical correlation function of the electric disturbance (ensemble-averaged quantity over surfaces with different microstructure) on the surface was approximated by Dirac's delta function. The amplitude speckle reduction (Fig. 2.12) is due to the fact, that the size of the illuminated area is comparable with the wavelength of the illuminating source. Then, the statistical correlation function in the surface plane is partly correlated and the width of the correlation function is approximately one wavelength. This fact results in killing of higher spatial modes. Based on our simulation results, we estimated the limit value of the beam waist on the target where higher-mode suppression can be expected as 25 microns.

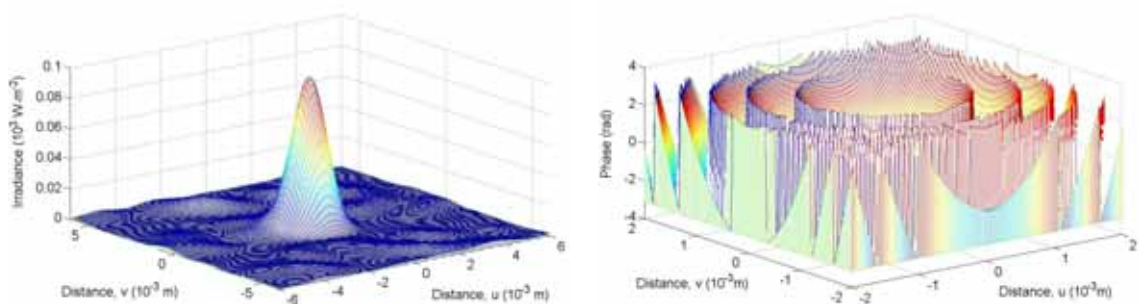


Fig. 2.12. Irradiance and phase of the backscattered field in the image plane (radius of illuminated area $w = 5\mu\text{m}$).

The advantage of an interferometer working with this kind of backscattered field is that this field is similar to the reference Gaussian beam. Hence, it is simple to achieve the amplitude and phase matching on the detector to produce a maximum interferometric signal.

Before concluding the section with experimental results, we present a mathematical approach how the speckle reduction can be understood. First we will limit ourselves to paraxial approximation of the backscattered field. The field on the target can be then decomposed into Hermite-Gaussian modes which form a basis set [22]. These normalized eigenfunctions for one transversal component at $z=0$ where the target is placed are given by (the considered geometry is shown in Fig. 2.9)

$$\tilde{\psi}_n(\xi,0) = \left(\frac{2}{\pi}\right)^{1/4} \left(\frac{1}{2^n n! w}\right)^{1/2} H_n\left(\frac{\sqrt{2}\xi}{w}\right) \exp\left(-j\frac{k\xi^2}{2\tilde{q}}\right), \quad (2.33)$$

where H_n are Hermite polynomials and complex quantity \tilde{q} is defined as

$$\frac{1}{\tilde{q}} = \frac{1}{R} - j\frac{\lambda}{\pi w^2} \quad (2.34)$$

where R stands for the radius of curvature. The second transversal component is expressed analogously. The backscattered field can be then written as

$$\tilde{E}(\xi,\eta,0) = \sum_n \sum_m \tilde{c}_{nm} \tilde{\psi}_n(\xi,0) \tilde{\psi}_m(\eta,0) \quad (2.35)$$

where the weighting coefficients are given by

$$\tilde{c}_{nm} = \iint \tilde{E}(\xi,\eta,0) \tilde{\psi}_n^*(\xi,0) \tilde{\psi}_m^*(\eta,0) d\xi d\eta. \quad (2.36)$$

This decomposition is suitable because the intensity pattern of any given mode changes size but not shape as it propagates forward in z – direction. Thus there is no mode coupling as the field propagates to the detector through free space and lenses (this is mathematically given by the fact that (2.33) are eigenfunctions of Fourier transform).

The target is illuminated by Gaussian beam so one can write for backscattered normalized field at the target plane

$$\tilde{E}(\xi,\eta,0) = \frac{2}{\pi w^2} \exp\left(-\frac{\xi^2 + \eta^2}{w_0^2}\right) \exp(j\phi(\xi,\eta)) \quad (2.37)$$

where $\phi(\xi,\eta)$ may be interpreted as a sample function of a random process which characterizes the phase distribution. As we are interested in relative power contained in the modes, the normalization in (2.37) has no spoiling effects in the following calculation.

The rough surface is described by a height function $h(\xi,\eta)$ that represents the departure of the surface from its mean position. Height functions for metal and white paper are depicted in Fig. 2.13. The height function is assumed to be a random process with autocorrelation function $\Gamma_h(\xi,\eta)$.

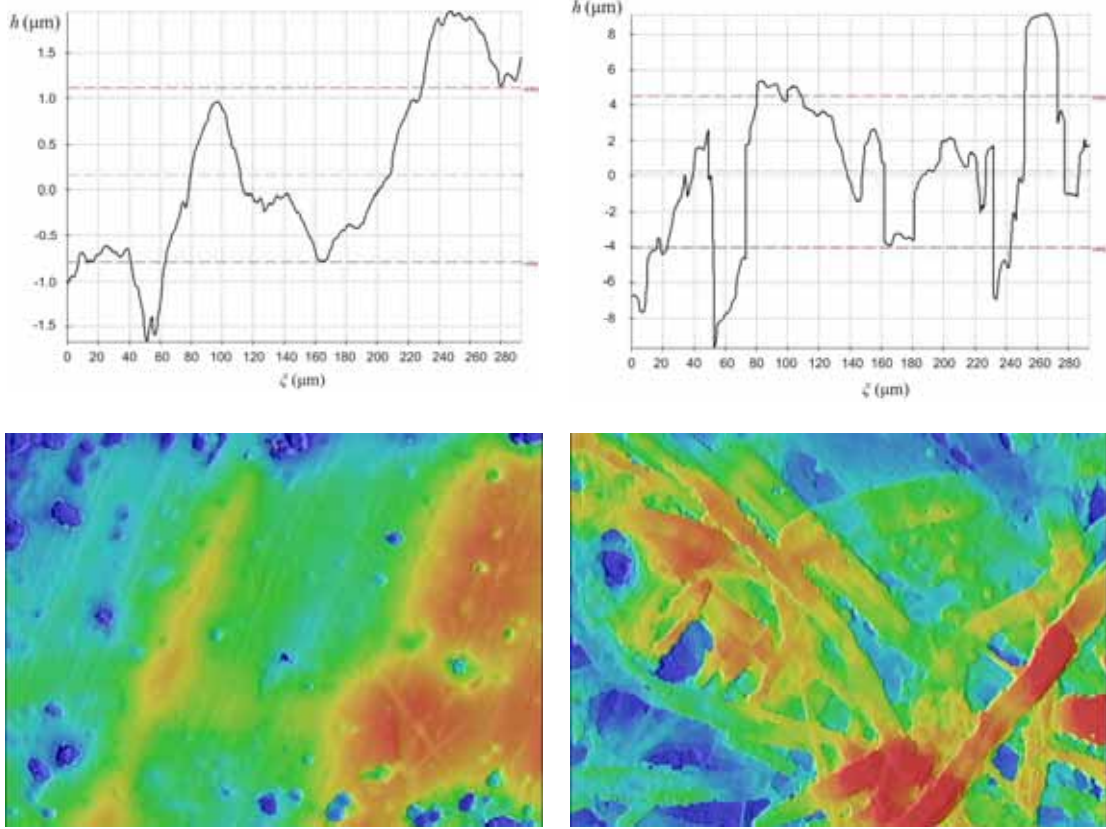


Fig. 2.13. Height functions and two dimensional profile of rough steel surface (left) and white paper (right). Figures were obtained at University in Darmstadt.

We will assume the simplest relation between the height function and the phase of the backscattered field

$$\phi(\xi, \eta) = \frac{2\pi}{\lambda} (1 + \cos \beta) h(\xi, \eta) \quad (2.38)$$

where β is angle between the normal of the surface and the wave vector of the illuminating beam. Note that (2.38) does not include shadowing, multiple scattering and the field penetration into the material which should not be neglected especially in the white paper case. However, our used imaging optics eliminated speckles for all targets we tested without significant modification. So we will use (2.38) as an approximation which is sufficient for our purpose, namely for finding relation between the spot size of the illuminating beam and weighting coefficients \tilde{c}_{nm} .

When assumptions are made that the surface height fluctuations are a Gaussian random process and the normalized correlation function of the surface heights is also of Gaussian form, then the relation between the coherence factor of the reflected field Γ_ϕ and rough surface can be expressed as [4]

$$\begin{aligned} \Gamma_\phi(r) &= \langle \exp[-i(\phi(r_1) - \phi(r_2))] \rangle = \exp[-\sigma_\phi^2 (1 - \Gamma_h(r))] = \\ &= \exp\left[-\sigma_\phi^2 \left(1 - \exp\left(-\frac{r}{r_c}\right)^2\right)\right] \end{aligned} \quad (2.39)$$

where $r^2 = (\Delta\xi)^2 + (\Delta\eta)^2$, next σ_ϕ^2 represents the variance of the phase and can be obtained using (2.38) and r_c specifies the width of the surface Gaussian correlation function.

Inserting of (2.37) into (2.36) one obtains

$$\begin{aligned} \langle \tilde{c}_{nm} \rangle &= \left\langle \frac{2}{\pi w_0^2} \iint \exp\left(-\frac{\xi^2 + \mu^2}{w_0^2}\right) \exp(j\phi(\xi, \mu)) \tilde{\psi}_n^*(\xi, 0) \tilde{\psi}_m^*(\mu, 0) d\xi d\mu \right\rangle = \\ &= \frac{2}{\pi w_0^2} \iint \exp\left(-\frac{\xi^2 + \mu^2}{w_0^2}\right) \Gamma_\phi(\xi, \mu) \tilde{\psi}_n^*(\xi, 0) \tilde{\psi}_m^*(\mu, 0) d\xi d\mu. \end{aligned} \quad (2.40)$$

In order to evaluate integral (2.40), we need to know the parameters w and R which characterize Hermite-Gaussian modes. We will choose them to be equal to the parameters of the illuminating beam which is focused on the target, hence $w = w_0$ and $R \rightarrow \infty$. This choice assures that when coherence factor $\Gamma_\phi = 1$, only fundamental mode will be present in the backscattered field, i.e. $|\tilde{c}_{00}| = 1$. Next, the variance and correlation of the height function needed to evaluate Γ_ϕ depends on the spot size of the illuminated beam as can be seen from Fig. 2.13. Finally, as was stated previously, when computer simulation was presented, the coherence factor has always a width of at least one wavelength.

The integral (2.40) was solved numerically and the results for fundamental mode are shown in Fig. 2.14. The modulus of coefficient \tilde{c}_{00} is depicted as a function of beam waist of the illuminating beam. The coherence factor was chosen to correspond to the metal surface, white paper and in the last case, coherence was approximately one wavelength.

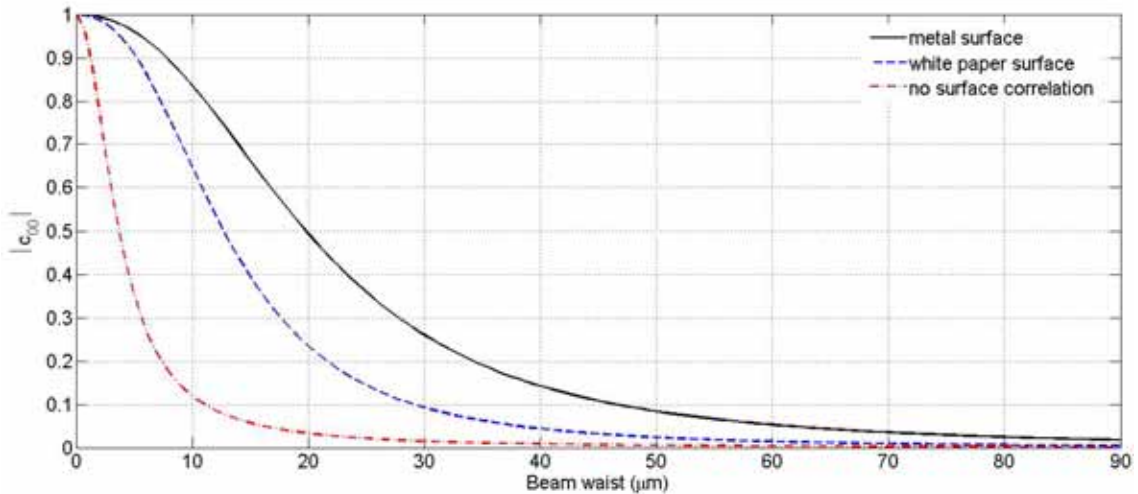


Fig. 2.14. The modulus of the fundamental Gaussian-Hermite mode of the backscattered field for different surfaces as a function of beam focusing.

The results described in the section were verified experimentally with the results shown in Fig. 2.15. The two figures on top right are background radiation and reference beam pattern on the detector respectively. The remaining pictures illustrate the varying signal irradiances obtained by step-wise reduction of the size of the illuminated area on

the target; the third figure depicts the case of 100 microns and the last figure (bottom right) depicts the case of 25 microns.

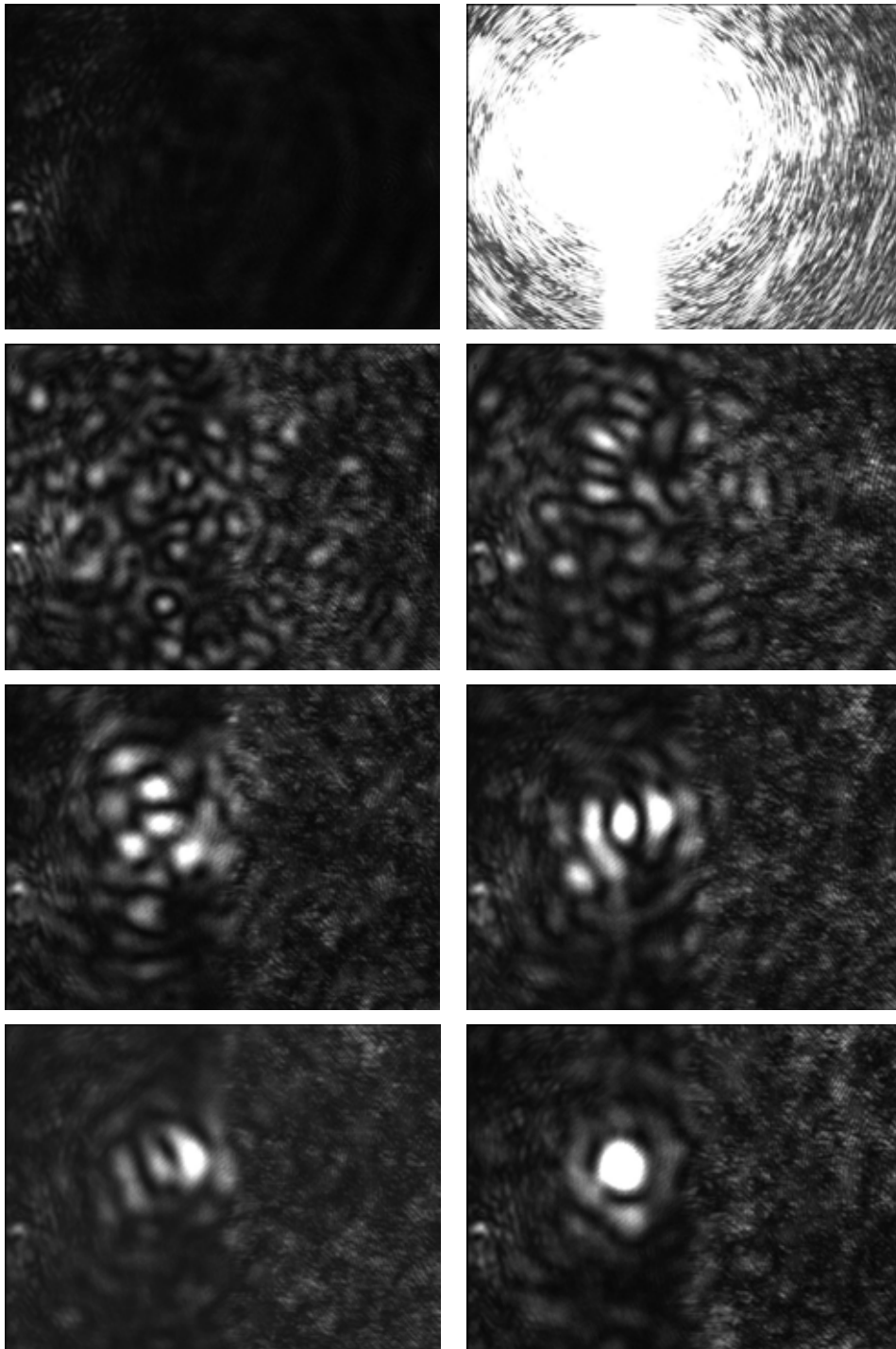


Fig. 2.15. Experimental verification of spatial modes reduction. Two figures on the top correspond to background radiation and reference beam, respectively. Remaining figures represent irradiance patterns of the field backscattered from the target for different sizes of illuminated target area (from $2w = 100 \mu\text{m}$ to $2w = 25 \mu\text{m}$). The dimensions of single area are 3 and 4 mm.

Finally, it needs to be emphasized that the speckle reduction due to the sharply focusing should not be understood as the specular component of the backscattered field.

In the previous calculation and computer simulation the direction of propagation of the reflected field was opposite to the direction of the illuminated beam and not the one which corresponds to the specular reflection. Moreover, the target in the experiments was placed at the beam focus without careful rotational alignment. With the rotation of the target, the backscattered field at the detector held its position.

2.7 Zoom lens in vibrometry

Zoom lenses are standard components in modern photographic cameras and they are also being used in a broad range of technical applications [23]. However, to our knowledge, commercially produced vibrometers operate with optical systems having a fixed focal length. We demonstrate here, for the first time, that the use of a Zoom system in the imaging part of the vibrometer provides a considerable improvement in signal quality.

Figure 2.16 visualizes the imaging situation in a laser vibrometer. We first consider the upper drawing (a). The light beam coming from the laser, at first slightly divergent, is made convergent by a first lens - the field lens - and forms a focal point at some distance behind the field lens. Behind this focal point, the beam is divergent again and is then focused once again by a second lens, the front lens of the system. In a laser vibrometer, this second focal point must be made to coincide with the position of the target by suitably positioning the front lens. The conditions that the arrangement has to satisfy can be expressed by the imaging equation

$$\frac{1}{f_1} = \frac{1}{g_1} + \frac{1}{b_1} \quad (2.41)$$

from which we get for the magnification factor $M1$ of the front lens (relating the beam width on the target to the one at the intermediate focal point)

$$|M1| = \frac{b_1}{g_1} = \frac{f_1}{g_1 - f_1}. \quad (2.42)$$

Now we consider the second drawing (b). There, the target is assumed to be placed at some larger distance, b_1' . If we wanted to have the beam focus again on the target, we would then find that for increasing b_1 to b_1' we would have to reduce g_1 to a value g_1' , i.e. we would have to move the lens to the left. This would, however, increase $|M1|$ as can be seen from (2.42), and is a consequence of our assumption that we had kept the focal length f_1 unchanged. Thus, we have to pay with a larger beam width for the correct placement of the beam waist in the target plane.

Obviously, we have to adapt not only g but also f to the new situation. Anyway, we have to satisfy a condition analogous to (2.41) which – see drawing (c) - now has to be written as

$$\frac{1}{f_2} = \frac{1}{g_2} + \frac{1}{b_2}. \quad (2.43)$$

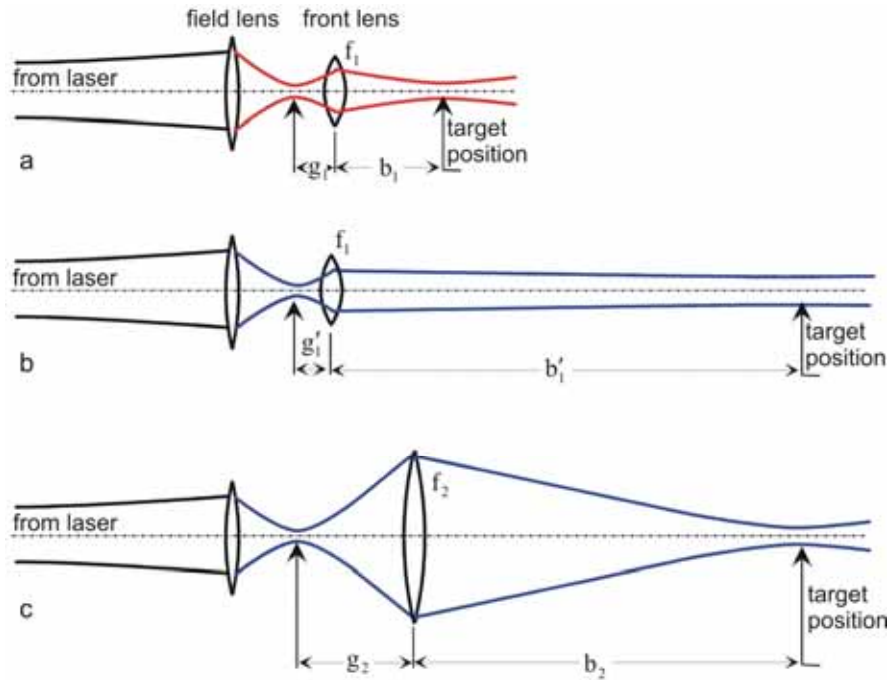


Fig. 2.16. Imaging optics in a laser vibrometer a) fixed target position, b) target position is enhanced and in order to have the beam focus on the target, front lens is slightly shifted towards the field lens, c) adaptation of focal length of the front lens and its position in order to preserve the beam with on the target.

Again, we can calculate the magnification factor which becomes

$$|M2| = \frac{b_2}{g_2} = \frac{f_2}{g_2 - f_2}. \quad (2.44)$$

As we want to have the same beam width on the target both in case (a) and in case (c) we must require that $|M1| = |M2|$. Substituting from (2.42) and (2.44) we find that we must be able to adapt the focal length of the front lens to the varying target distance; the condition that must be met then can be written as

$$\frac{f_2}{f_1} = \frac{b_2}{b_1}. \quad (2.45)$$

This means that if we want our vibrometer to cover a certain distance range without changing the spot size on the target, we have to select a variable-focus lens with an appropriate zoom range.

In Fig. 2.17 electrical output signals from the vibrometer (before digital processing) are shown for different targets placed at distances 0.5 m and 1m, respectively. The beam width was kept constant at 25 microns for both situations. By comparing the corresponding pictures for the same targets, one can see that the signal strength is not affected by the distance of the target and that the amplitude of the signal depends on the properties of the target.

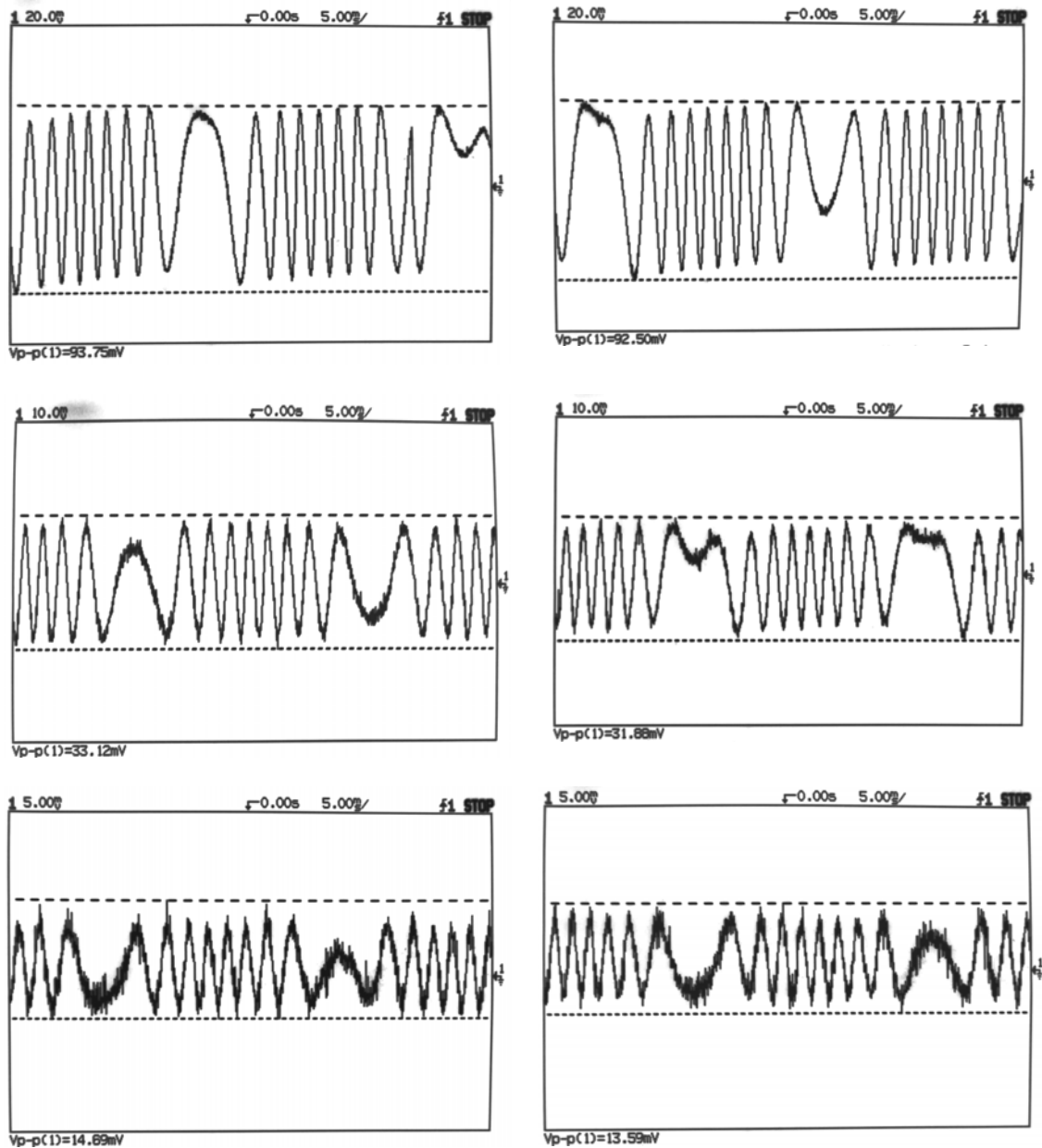


Fig. 2.17. Left part: output signals of the vibrometer analog front end (i.e., before AGC and ADC) for different types of targets (metal, ceramic, white paper) placed at a distance 0.5 m from the front lens, right part: output signals of the vibrometer for different types of targets (metal, ceramic, white paper) placed at a distance 1 m from the front lens.

The analog front end of the vibrometer was followed by an AGC stage keeping the signal amplitude constant even for varying optical power. This was to make sure that the dynamic range of the analog-to-digital converter preceding the digital processing part of the instrument was covered to its best. In other words, the amplitude of the electrical signal was independent of the amount of optical intensity which was brought to interference with the reference beam. The different “effective” intensity of the backscattered field from the target is due to the different reflectivities of the targets, focusing and pseudo-depolarization. These effects result in different signal-to-noise ratios (see Fig. 2.18).

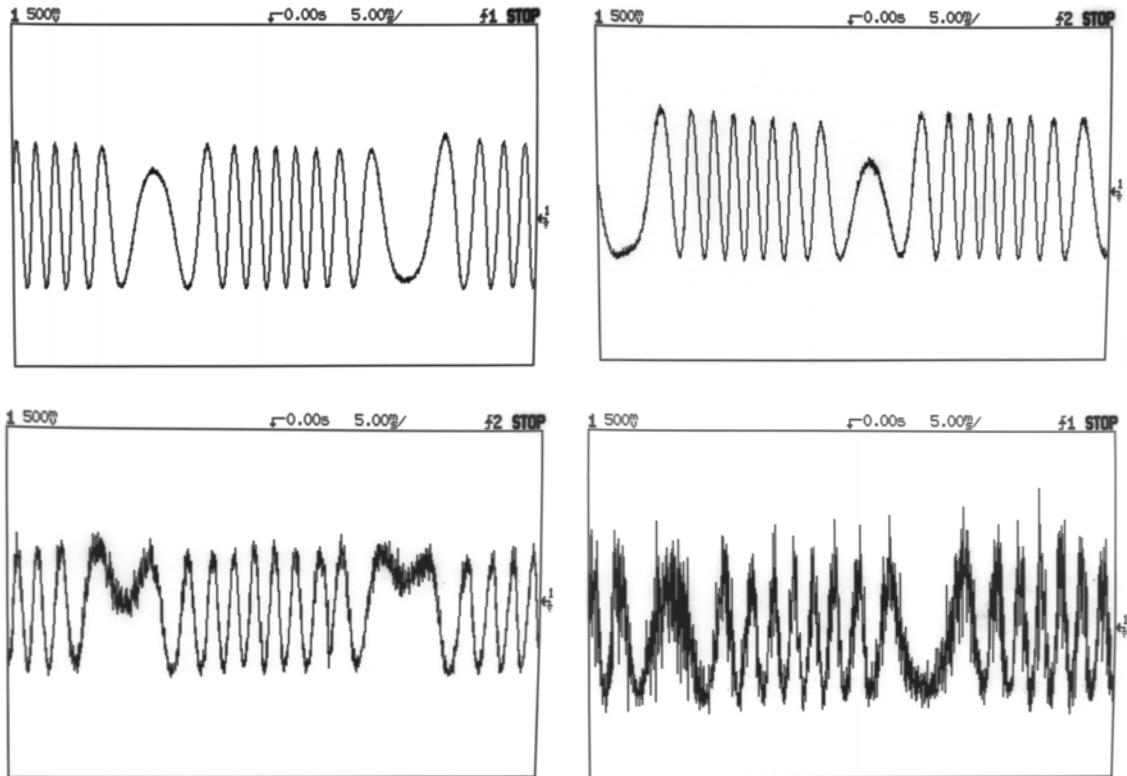


Fig. 2.18. Output signal of the vibrometer after automatic gain control for different types of targets (reflection film, metal, ceramic, white paper) placed at the distance 1 m from the front lens.

We conclude the section with a photograph of the experimental arrangement of the vibrometer shown in Fig. 2.19.



Fig. 2.19. Experimental arrangement of the vibrometer.

2.8 Multimode interference

Even though this topic is not the main object of the chapter, we wish to illustrate a problem here which occurs in interferometry when a multimode He-Ne laser is used. Namely a periodic extinction and revival of the interferometric signal with the change of the target distance.

The width of the Gaussian lineshape is approximately 1.5 GHz and the longitudinal mode spacing for a typical resonator is around 730 MHz. Hence, in normal working conditions (no external mode selection), two modes are present in the output beam.

The beam from the laser is divided into two parts, reference part and a beam which hit a target. In the case of one mode case, the time-averaged power on the detector can be expressed in usual way

$$\langle P_D \rangle = P_0 \left[1 + |g^{(1)}(\tau)| \cos\left(\frac{2\pi}{\lambda} 2z\right) \right] \quad (2.46)$$

where z is distance to the target (a half of the path difference between reference and measurement arm), P_0 is output power of the laser, λ is the mean wavelength and $g^{(1)}(\tau)$ is the degree of first-order temporal coherence. In (2.46), it was assumed that reference and measurement beam share the same amount of the laser output power and are equally polarized. The time difference between reference and signal arm τ in most interferometry applications is much shorter than the coherence time of He-Ne laser. The modulus of degree of first-order temporal coherence can be then set to unity (monochromatic assumption) and the contrast on the detector is independent of the target distance.

Now n modes are assumed to be within the atomic lineshape of the gain medium. The electrical field emerging from laser at some reference point can be written as

$$\mathbf{E}(t) = \sum_n e^{j\omega_n t} E_{0n} \begin{pmatrix} \cos \chi_n \\ \sin \chi_n e^{j\varphi_n} \end{pmatrix} \quad (2.47)$$

the polarimetric parameters χ_n and φ_n for each frequency component are fixed in time, the angular frequencies and complex amplitudes of modes are ω_n and E_{0n} , respectively. In the He-Ne laser, the gas envelope windows are tilted at Brewster's angle which causes the output radiation modes to be identically linearly polarized. The resulting SOP (state of polarization) is thus the same like in single-mode case and the reference and signal beam again possess same polarization. However, the detected time-averaged power in the case of two modes with equal amplitudes is expressed as (we assume only two modes to be within the atomic lineshape because of the parameters stated at the beginning of the chapter)

$$\langle P_D \rangle = P_0 \left[1 + \cos\left(\Delta\omega \frac{z}{c}\right) \cos\left(2\pi \frac{2z}{\lambda}\right) \right] \quad (2.48)$$

where two modes have angular frequencies

$$\omega_1 = \bar{\omega} + \frac{\Delta\omega}{2}, \quad \omega_2 = \bar{\omega} - \frac{\Delta\omega}{2}. \quad (2.49)$$

Equation (2.48) can be also written in similar form to (2.46)

$$\langle P_D \rangle = P_0 \left[1 + |g^{(1)}(\tau)| \cos\left(2\pi \frac{2z}{\lambda}\right) \right] \quad (2.50)$$

where the modulus of degree of first-order temporal coherence is now

$$|g^{(1)}(\tau)| = \left| \cos\left((\omega_1 - \omega_2) \frac{z}{c}\right) \right|. \quad (2.51)$$

In Fig. 2.20 on the left, there is shown a theoretical detected irradiance (related to its maximum value) as a function of the target distance. The target distance is here to be understood as a half of the path difference between the both interferometric arms. The blue color in the figure indicates fast irradiance oscillations (the second cosine term in (2.48)).

The situation with the unequal gain for both modes is depicted in Fig. 2.20 on the right. Namely, the power gain ratio of both modes is 0.762 (this particular value was found to fit with the measurement data for the used laser, see later).

The solid curve in Fig. 2.21 is a theoretical curve which corresponds to the unequal gain for the both modes (with gain ratio 0.762) and takes into account the beam spreading of the target beam (it is not an interpolation of the measurement data). The marks in the Fig. 2.21 then indicate measurement data. The AC component of the electrical signal after the photodetection for a given target distance was measured. This AC component for a suitable detector is linearly proportional to the visibility. Finally, we need to state that a mirror was used as the target in order to achieve the same power of reference and signal beam and, more importantly, to neglect effects which arise using non-conventional target.

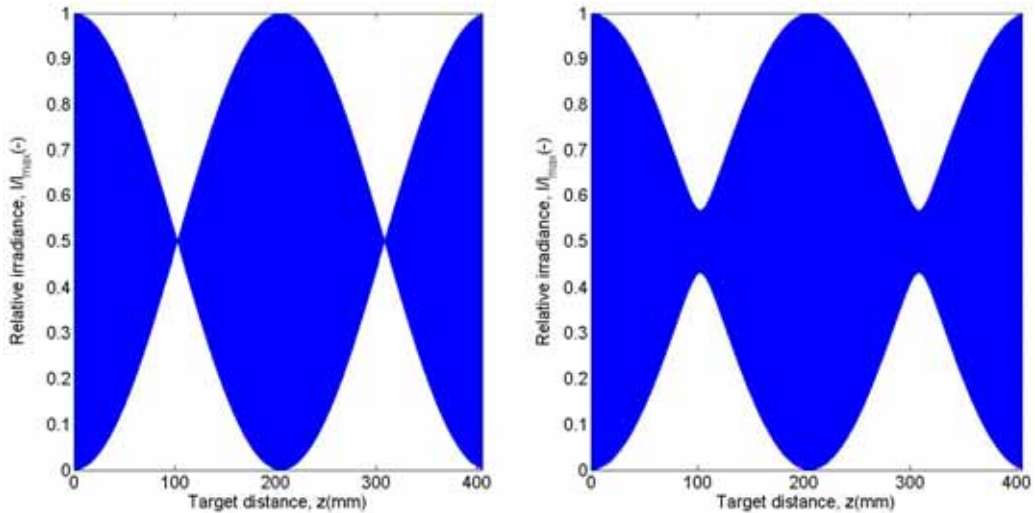


Fig. 2.20. Relative irradiance as a function of the target distance in the case of the equal atomic gain for both modes (left) and with an unequal gain (right).

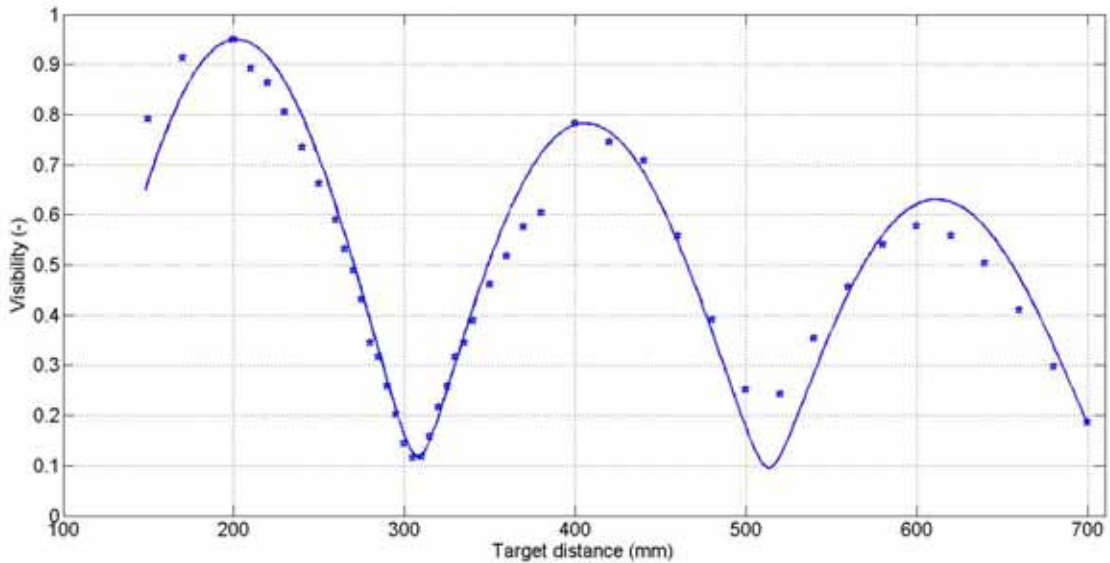


Fig. 2.21. Visibility dependence on the target distance in the case of unequal gain for Gaussian beams (solid curve) and measurement data marks.

2.9 Chapter summary

Let us summarize main results which were reported in the chapter. We derived probability density function of the complex modulated intensity for different degrees of pseudo-polarization and showed how the modulated intensity is reduced due to the speckle field. Next, we illustrated that this reduction of interferometric signal is not necessary. Using a suitable imaging optics the speckle field can be removed. The speckle reduction can be done both in phase and in amplitude. In fact when the illuminating beam is focused sharply on the target the fundamental mode in the backscattered field dominates. This single mode regime was compared to an optical fiber where also higher modes are eliminated with reducing the core diameter. Finally a zoom objective was used in order to achieve independency of the target distance.

3 Periodic deviations in vibrometry

In this chapter, it is studied how polarization imperfections of components influence the output signals of an interferometer.

The mostly used interferometers produce interference signals which are in quadrature at the output of an interferometer. These quadrature signals are generated using polarization method. The main tasks, which are solved by the optical systems, are that the phase shift between these signals is $\pi/2$, the amplitudes of both signals are equal and as high as possible for increasing the accuracy of a measurement. Such optimization for a specific optical system can be found in [3].

The errors due to the polarization imperfection of real optical components are called periodic deviations and were studied in detail in [8] for the case of a heterodyne vibrometer. In [8], one can find the analytical formulations of these errors. These errors, however in general, are difficult to analyze not for the mathematical complexity but for finding the origin of these errors. Periodic deviations result not only from the inherent imperfections of components (non-ideal retardations, non-ideal transmission and reflection coefficients...) but also from the rotational misalignment of these components which in practice is hard to measure and control.

The most important result in the chapter is that it is shown that in the first approximation, periodic deviations can be corrected in the optical part of the vibrometer. That is, output signals are in real quadrature.

To accomplish the modeling of periodic deviation, one first needs to measure the polarization properties of optical components. We used a method based on detecting null intensity which we published in [24]. The basic idea of this method (and many other methods) can be found in [25]. However, in [25], we presented a variation of this method with a geometrical representation and discussed its accuracy in detail.

3.1 *Measuring properties of retarders and beamsplitters*

In this section, we developed methods to determine the polarization properties of basic optical devices like retarders, beamsplitters and mirrors using a Soleil-Babinet compensator.

The most used technique for the polarization treatment is Jones and Mueller calculus. The Jones matrix formalism is a direct consequence of linearity of Maxwell's equations. On the other hand, Mueller calculus is based on the assumption of a linear relation between the input Stokes vector and the output Stokes vector emerging from the optical system. Strictly speaking, Jones calculus is more fundamental than Mueller calculus.

However, another so called spin-vector calculus is used in following sections. Spin-vector formalism (widely used in quantum mechanics) is based on the same assumption like the Mueller calculus, thus vectors which represents a SOP (state of

polarization) form a linear vector space. Spin-vector formalism is used because it attains a high degree of abstraction and in connection with Dirac notation; it can be neatly described (bra and ket vectors). Finally spin-vector formalism makes a connection between Jones and Meuller calculus.

Retarders

A general lossless, linear retarder introduces a phase difference between two field components oriented along two mutually orthogonal directions in a cartesian coordinate system. If we assume, in the simplest case, that these so-called *eigenstates* coincide with the coordinate axes (x , y), we can describe its operation on the field by a unitary Jones matrix in the form

$$\mathbf{J}_R = \begin{bmatrix} 1 & 0 \\ 0 & \exp(-i\varphi) \end{bmatrix}, \quad \varphi \geq 0 \quad (3.1)$$

where φ is the phase difference experienced by two eigenstates of a retarder. An angular misalignment between the eigenstates of the retarder (meaning that fast/slow axes of the retarder are not parallel to y/x axes or, the device frame differs from the lab frame) and the axes of the coordinate system can be accounted for by applying a rotation matrix to matrix (3.1).

We want to determine the retardation angle φ introduced by a nominally-isotropic retarder between its slow and fast axis. A suitable measuring set-up is shown in Fig. 3.1. The laser, in connection with the polarizer, provides linearly polarized light oriented parallel to the y -axis, denoted $|y\rangle$. A Wollaston prism and two photodetectors determine the state of polarization (SOP) in a $|x\rangle$ - $|y\rangle$ basis (in the spin-vector formalism is described by first Pauli matrix). The fast axes (FA) of the retarder-under-test and a Soleil-Babinet compensator (SBC) are set so as to hold an angle of $\pi/4$ with the y -direction.

A common means for visualizing the situation is the Poincaré sphere (Fig. 3.2). There, the x axis of the lab frame is represented by an axis extending from the center of the sphere to the left-forefront, $|x\rangle$. The y axis $|y\rangle$, in lab frame rotated by $\pi/2$ with respect to the x axis, also lies in the equatorial plane, however rotated with respect to $|x\rangle$ by *twice its rotation angle* in lab frame, π . As with the $|x\rangle$ - $|y\rangle$ axes, any two orthogonal SOPs are represented by a line connecting two points diametrically opposed on the sphere.

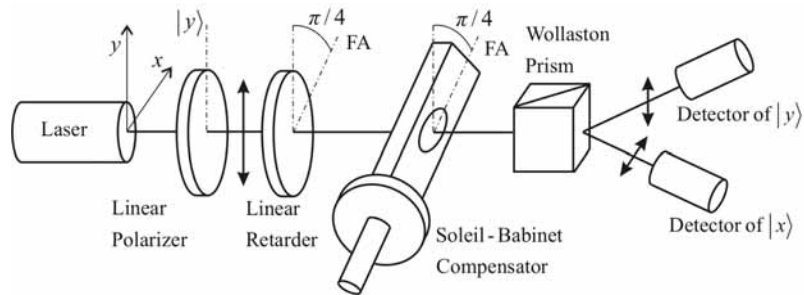


Fig. 3.1. Setup for measuring a phase difference experienced by two eigenstates of a retarder.

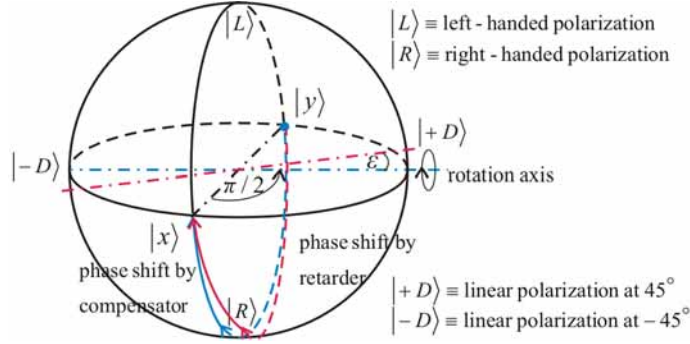


Fig. 3.2. Illustration on the Poincaré sphere.

A linear retarder is also represented on the sphere by a line lying in the equatorial plane, again with its angular orientation with respect to the Poincaré $|x\rangle$ - $|y\rangle$ axis given by *twice its rotation angle* in lab space. Thus, an orientation in lab space of $\pi/4$ leads to an orientation on the Poincaré sphere of $\pi/2$ (horizontal blue line in Fig. 3.2). The retarder’s effect on the SOP is then to rotate the initial state $|y\rangle$ about this *eigenstate axis* by an angle φ . A device having $\varphi = \pi/2$ is called a quarter-wave-plate (QWP). For an adjustable phase shift of the SBC, the output SOP can be made to move along the blue circle on the Poincaré sphere. A half-circle (as drawn), corresponding to a QWP’s $\varphi = \pi/2$ and shift by the SBC, changes the input SOP from $|y\rangle$ to $|x\rangle$, a SOP which can easily be detected by the Wollaston prism. Our measurement task of determining φ of the retarder is now quite easy to solve: We set the *combined* retardation angle of retarder and SBC to π by making sure the output state is $|x\rangle$ and read the SBC setting. The difference to π gives the retardation provided by the retarder-under-test.

We finally state that if the retarder is not lossless, (3.1) needs to be corrected. This is dealt with later in the section.

Error estimation

The used light source (He-Ne laser with a linear polarizer) produced well pure state. Also, the extinction coefficient of the Wollaston prism is very high (10^5). Thus, the error sources of the method described are the phase resolution of the SBC and the setting error of its orientation angle $\pi/4$. The resolution of the compensator directly affects the measured phase φ and was approximately 0.2° for our setup.

A setting error of the orientation angle $\pi/4$ (cf. red curves in Fig. 3.2) has the effect that the rotation on the Poincaré sphere occurs around an axis rotated by an error angle ε with respect to the desired ideal rotation axis. (In fact ε is the difference between the orientation angles of the retarder and the compensator.)

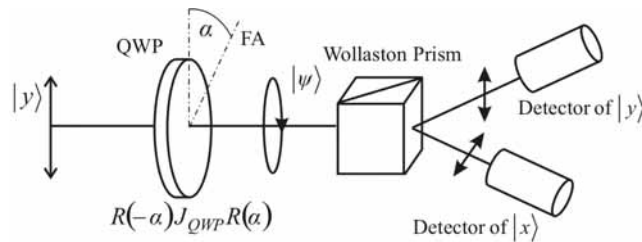


Fig. 3.3. Determination of α based on the detected intensities in each eigenstate of the Wollaston prism.

For the estimation of the error angle ε we use a following concept. Let us assume the situation plotted in Fig. 3.3.

Our aim is to determine the orientation angle α from the output intensities. In our measurement the output voltages for each detector were 30 mV and 30 mV. Suppose that detectors together detected approximately 100 photons. That means 50 photons were in state $|y\rangle$ and 50 photons in state $|x\rangle$. We first need to know the probabilities that the upper or the lower detector will be excited when only one photon is at the input. The final state $|\psi\rangle$ in Fig. 3.3 generally has an elliptic polarization and satisfies

$$|\psi\rangle = \mathbf{R}(-\alpha)\mathbf{J}_{QWP}\mathbf{R}(\alpha)|y\rangle \quad (3.2)$$

where the rotation matrix $\mathbf{R}(\alpha)$ connecting the lab and the QWP frame, respectively, is defined as

$$\mathbf{R}(\alpha) = \begin{bmatrix} \cos \alpha & \sin \alpha \\ -\sin \alpha & \cos \alpha \end{bmatrix}. \quad (3.3)$$

As said, the matrix \mathbf{J}_{QWP} is given by (3.1) with $\varphi = \pi/2$. Of course the actual φ value is a little different, but in a first approximation we assume $\varphi = \pi/2$ (moreover this method of determining the error angle ε can be iterated). Using (3.2) one obtains the following probabilities for excitations of the upper and the lower detector

$$\begin{aligned} P(y) &= \sin^4 \alpha + \cos^4 \alpha \\ P(x) &= 2 \cos^2 \alpha \sin^2 \alpha. \end{aligned} \quad (3.4)$$

We determine the conditional probability that exactly m photons excite the upper and n the lower detector when the orientation angle of the QWP is between α and $\alpha + d\alpha$, and we get (we dropped the normalization)

$$P(\alpha) = P^m(y)P^n(x)d\alpha. \quad (3.5)$$

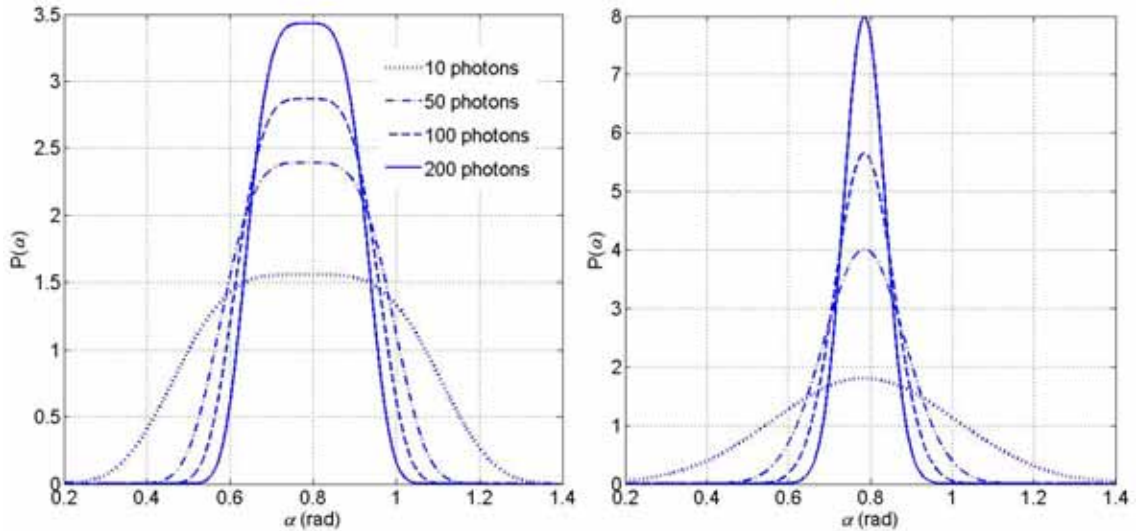


Fig. 3.4. Error angle estimation for a test with a not suitable (left) and suitable (right) polarization of the incident light.

Fig. 3.4 depicts four calculated examples. For 10 incident photons in state $|y\rangle$ we find that 5 photons will be detected by the upper and 5 photons by the lower detector, respectively ($m = n = 5$, dot line). Note that the α axis scaling is in radians ($\alpha = 45^\circ = 0.785$ rad). If we assume 100 incident photons in state $|y\rangle$ we find that 50 photons will hit the upper detector and 50 the lower one. This is plotted with a dot-dashed line. One can see that the peak still is not sufficiently narrow, even for a large number of detecting photons, and the error of the setting angle $\pi/4$ is too high.

Note that in all examples in left part of Fig. 3.4 we assumed that the identical amount of photons was detected by both detectors. This assumption was done for the reason of easier comparison with the next test which follows.

Much better results are obtained when the light source produces one of the eigenstates of the QWP (i.e., $|L\rangle$ or $|R\rangle$) rather than $|y\rangle$. Then one detector gets fully excited and the second detects zero intensity. The result for this setting is shown in Fig. 3.4 on the right, for four different intensities which correspond to the previous example. For example when the number of incident photons was 10 the upper detector was 10 times excited and the lower one was not excited at all. With increasing number of incident photons all curves are narrowing as is illustrated by Fig. 3.4. Note that for the second case ($|L\rangle$ state was produced by the source) probabilities for excitations of the upper and the lower detector are

$$\begin{aligned} P(y) &= 0.5 + \cos \alpha \sin \alpha \\ P(x) &= 0.5 - \cos \alpha \sin \alpha. \end{aligned} \quad (3.6)$$

The deviation of the curve in Fig. 3.4 can be taken as error ε . The main aim of this section was to recommend to use such a preparing state for the setting angle $\pi/4$ to obtain zero intensity for one detector. Then the error ε is reduced.

Beamsplitters

The measurement task that we are treating next is determination of the polarization properties of optical beam splitters (BS). As in the set-up treated previously, the optical source consists of a laser and a linear polarizer. It is used to generate either vertical polarization, horizontal polarization, or diagonal polarization, i.e. three separate measurements will be performed. The measuring arrangement again includes the Soleil-Babinet compensator, the Wollaston prism and the photodiode. This allows one to determine an arbitrary pure polarization state (an arbitrary Jones vector).

The action of the compensator is described by

$$\begin{aligned} \mathbf{J}_{SB}(\alpha, \theta) &= \mathbf{R}(-\theta) \mathbf{J}_{SB}(\alpha) \mathbf{R}(\theta) = \\ &= \begin{bmatrix} \cos \theta & -\sin \theta \\ \sin \theta & \cos \theta \end{bmatrix} \begin{bmatrix} 1 & 0 \\ 0 & \exp(-i\alpha) \end{bmatrix} \begin{bmatrix} \cos \theta & -\sin \theta \\ \sin \theta & \cos \theta \end{bmatrix} \end{aligned} \quad (3.7)$$

where α denotes the phase retardation between fast and slow axis of the compensator, and θ is the angle between the fast axis of the compensator and the y -direction, i.e. the angle which connects the lab frame and the device frame.

First, diagonal polarization is generated (Fig. 3.5). Then the compensator is set to produce a final state $|y\rangle$ by changing the angle of rotation θ and the phase shift α . Then the state $|\psi\rangle$ immediately after passing the beamsplitter satisfies

$$|y\rangle = \mathbf{J}_{SB}(\alpha, \theta)|\psi\rangle. \quad (3.8)$$

From (3.8) one obtains

$$|\psi\rangle = \mathbf{J}_{SB}^{-1}|y\rangle. \quad (3.9)$$

In a very good approximation one can write

$$\begin{aligned} \mathbf{J}_{BS}|y\rangle &= \tilde{y}|y\rangle \\ \mathbf{J}_{BS}|x\rangle &= \tilde{x}|x\rangle. \end{aligned} \quad (3.10)$$

The eigenvalues of the BS determine the loss of the device. Hence the matrix of the BS is in the form

$$\mathbf{J}_{BS} = \begin{bmatrix} |\tilde{x}| & 0 \\ 0 & |\tilde{y}|\exp(i\Delta\delta) \end{bmatrix} \quad (3.11)$$

where $\Delta\delta$ is the phase shift between the eigenstates $|x\rangle$, $|y\rangle$. Note that it is not possible to illustrate loss on the Poincare sphere, because the particular operation on the initial pure state is not unitary. Although all operations in the nature are unitary the description of the real components without considering the interaction with an environment is not unitary. Hence if we want to look only on the system which consists of an input state and an optic component we need to introduce non-unitary operations. This follows from amplitude damping and phase damping (loss information without loss of energy).

For determining $\Delta\delta$ we, for the moment, suppose a unitary matrix (i.e. a lossless BS)

$$\mathbf{J}_{BSu} = \begin{bmatrix} 1 & 0 \\ 0 & \exp(i\Delta\delta) \end{bmatrix}. \quad (3.12)$$

We further have

$$|\psi\rangle = \mathbf{J}_{BSu}|-D\rangle. \quad (3.13)$$

Parameter $\Delta\delta$ is obtained by comparing (3.9) and (3.13).

Now we determine the magnitude of the eigenvalues which are needed in (3.11). First the light source is set to produce $|x\rangle$. Next we calculate $|\tilde{x}|$, the square root of the ratio of outgoing and incident intensity. The parameter $|\tilde{y}|$ is obtained in an analogous way, by setting the source so as to generate light in state $|y\rangle$.

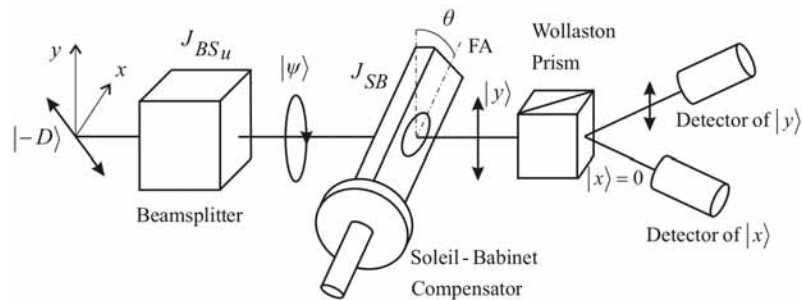


Fig. 3.5. Measuring setup for a beamsplitter.

The matrix for the deflected (reflected) beam is obtained in the similar manner as for the transmitted beam. The method for measuring the polarization properties can be used as well for PBS (polarized beamsplitters) and mirrors.

Let us summarize the assumptions which have been made in the measurement method just described. We supposed that the action of a device on an input state is unitary (no losses, no interaction with the environment). We also supposed orthogonality of eigenstates of measuring devices and no depolarization effects. And finally we assumed that the dynamical laws which govern the working of used devices do not influence the polarization properties. Then we took losses and correct previously determined unitary matrices.

3.2 Influence of periodic deviations on quadrature signals

Introduction

The errors in the laser interferometers can be divided into three categories: setup dependent, instrument dependent and environment dependent.

The setup dependent errors are found depending on the measurement setup. These type of errors are reduced using Mach-Zehnder interferometer instead of Michelson interferometer. In the Mach-Zehnder interferometer, beams are widely separated using the beam dividers and mirrors as separate elements. This is the basic difference between Mach-Zehnder and Michelson interferometer where a plane parallel glass plate is used (thus beam dividing and reflecting is at the same point, at one optical element). Hence in the Mach-Zehnder setup, one can control beams more to protect the undesirable interference with the source beam. The next advantage of Mach-Zehnder interferometer over Michelson interferometer is that there are lesser requirements on the angular position of the mirrors. So, Mach-Zehnder interferometer possesses better mechanical stability. However, both interferometers suffer from deathpath error (the difference in the distance in the air between the reference and measurement paths).

All real components have non-ideal properties. These non-idealities are due to the instrumental errors. Using concept of homodyne detection instead of heterodyne has the advantage that there is lower requirement for the frequency stability of the laser source. On the other hand, in the homodyne detection, there are higher requirements on the polarization properties of the used components. The errors which are due to the non-ideal polarization properties are called periodic deviation and are the result of polarizing mixing. Periodic deviations are the most important errors in the category of instrumental errors.

In the category environment errors, the thermal influence of the interferometer is found. The main errors are expansion of optics components due to the thermal effects of the environment and due to the heat from the laser source. Also refracted index of the medium through the beams travels belong to this category too. But when traveling paths are relatively short and the whole setup is protected from turbulences of the air, this kind of error is not critical.

In summary, by using Mach-Zehnder setup, the setup dependent errors are suppressed. The most important error source is in non-ideal polarization properties of components, so-called periodic deviation.

The most important result concerning the periodic deviations in [8] is that an interference signal can be expressed as

$$I(t) = 2\sqrt{I_R I_S} \cos[\omega t + \Delta\phi + \phi_S(t) + \phi_{pd}] \quad (3.14)$$

where I_R is intensity of the reference beam alone, I_S is intensity of the signal beam alone, $\Delta\phi$ is the phase difference between both beams, $\phi_S(t)$ is the phase introduced due to the moving measured object and finally ϕ_{pd} represents a contribution from periodic deviations. The intensities appearing in (3.14) should be understood as time-averaged over the integration time of a used photodetector. The average notation was suppressed in this case. In (3.14), it is also tacitly assumed that both beams possess the same polarization. If this is not the case, than the amplitude in (3.14) needs to be corrected according to section 2.2.

However, equation (3.14) was derived in [8] for a specific optical setup. In general the output electrical quadrature signals (after a photodetection) can differ in amplitude and even can contain some DC components. Hence generally these signals can be expressed as

$$\begin{aligned} I(t) &\approx A_{pd,I} \cos[\omega t + \Delta\phi + \phi_S(t) + \phi_{pd,I}] + D_{pd,I} \\ Q(t) &\approx A_{pd,Q} \cos[\omega t + \Delta\phi + \phi_S(t) + \phi_{pd,Q}] + D_{pd,Q}. \end{aligned} \quad (3.15)$$

In (3.15), factors as a responsivity of a photodiode and intensities of reference and signal beam was suppressed for a clearer illustration of the influence of periodic deviations. We emphasize that factors $A_{pd,I}$, $\phi_{pd,I}$, $D_{pd,I}$ (and similarly for the second quadrature) are constants and the coupling between amplitudes, phases and DC levels in both quadratures depend on the specific optical system. Note that we will use the word “quadrature” even in the case when the phase difference $\phi_{pd,Q} - \phi_{pd,I}$ is not strictly equal to $\pi/2$. Hence the word “quadrature” generally refers to the output electrical signals.

The possible reasons for periodic deviations are: elliptically polarized laser beam, rotational error in the alignment of a laser and used optics devices (beam splitters, linear polarizers, retarders) and different transmissions coefficients in the components for their eigenstates.

In [8] was also shown that

$$\phi_{pd} = -\arctan \frac{N}{M} \quad (3.16)$$

where N, M are some terms resulting from polarization imperfections of components and from non-ideal angular settings of the components.

Periodic deviation analysis

In Fig. 3.6, there is shown a schema of the interferometer which we have manufactured. It is the schematic schema of the real setup shown in Fig. 2.19. The meaning of the kets appearing in the schema is to represent particular polarization states. The normalization was dropped in the schema (for the states which passes the first two PBS and NBS) and was put back at the end of the description (the final four signals are already normalized). All components are assumed to possess no losses and ideal polarization properties and also all rotational settings are assumed ideal for the moment.

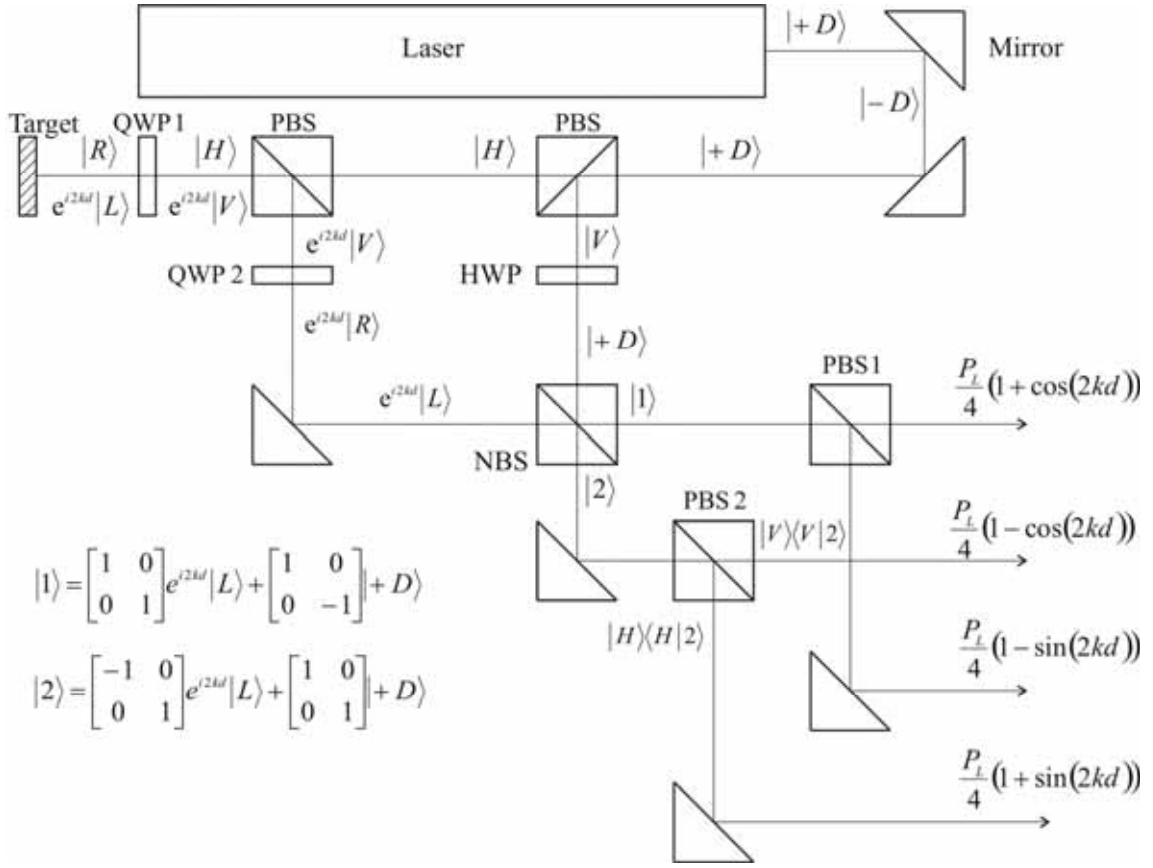


Fig. 3.6. Architecture of the interferometrical laser vibrometer.

The symbol P_L denotes the power of the laser, d is the component of the target displacement which is parallel to the illuminating beam and k is the magnitude of the wave vector.

Note that polarization imperfections of the final two mirrors need not to be taken into account because the following components, namely photodetectors, are not sensitive to the polarization. The angle between the fast axis of both QWP and the reference y -axis (the angle between device and lab frame) is 45° and the angle between lab frame and frame of HWP is 22.5° .

The action of the two last (measuring) polarizing beam splitters denoted as PBS 1 and PBS 2 is interpreted in a slightly different way than the first two PBS. This is done because these beam splitters accompanied with photodiodes (the photodiodes are not explicitly shown in Fig. 3.6) represent projective measurements (the nomenclature is summarized in section 6.2) in their eigenbasis. Hence the measurement results are expressed as

$$\begin{aligned} 1: \quad & \langle H|2\rangle^2 = \frac{P_L}{4}(1+\cos(2kd)) & 2: \quad & \langle H|1\rangle^2 = \frac{P_L}{4}(1-\cos(2kd)) \\ 3: \quad & \langle V|2\rangle^2 = \frac{P_L}{4}(1-\sin(2kd)) & 4: \quad & \langle V|1\rangle^2 = \frac{P_L}{4}(1+\sin(2kd)). \end{aligned} \quad (3.17)$$

To create two signals in the quadrature, the first two and the last two signals are subtracted in the analog part of the vibrometer. The resulting quadrature signals are depicted in Fig. 3.7. Three conditions are generally required for the quadrature signals:

the phase shift is to be equal to $\pi/2$, the amplitudes of AC components of the signals are to be equal to each other to provide identical conditions for the electronic signal processing and the amplitudes are to be high as possible for increasing the accuracy of a measurement.

Non-idealities of real components can be considered quite straightforwardly. The Jones matrix of a component in its eigenbasis has a diagonal form

$$\mathbf{J}_\lambda = \begin{bmatrix} |\lambda_a| \exp(i \arg(\lambda_a)) & 0 \\ 0 & |\lambda_b| \exp(i \arg(\lambda_b)) \end{bmatrix} \quad (3.18)$$

where the magnitudes of eigenvalues λ_a , λ_b represent the amplitude attenuation of the light as it passes through the device in the corresponding eigenvector and the phase of the eigenvalue is the phase delay seen in the corresponding eigenvector. When the lab frame differs from the device frame in which possess the Jones matrix form of (3.18), then the Jones matrix in the lab frame can be expressed as

$$\mathbf{J} = \mathbf{R}(-\theta) \mathbf{J}_\lambda \mathbf{R}(\theta) \quad (3.19)$$

where angle θ connects the lab frame and the device frame and \mathbf{R} is a two-dimensional rotation matrix. For retarders, it is convenient to express the phase of the eigenvalue as a sum of the ideal phase and the phase error of the retarder and angle θ express as a sum of the desired orientation of the fast axis and the rotational misalignment. For example, a QWP which fast axis holds with the y -axis angle $\pi/4$ is described by the following matrix

$$\mathbf{J} = \mathbf{R}\left(-\frac{\pi}{4} - \theta_{err}\right) \begin{bmatrix} |\lambda_a| e^{-i\left(\frac{\pi/2 + \delta_{err}}{2}\right)} & 0 \\ 0 & |\lambda_b| e^{i\left(\frac{\pi/2 + \delta_{err}}{2}\right)} \end{bmatrix} \mathbf{R}\left(\frac{\pi}{4} + \theta_{err}\right) \quad (3.20)$$

where the rotational misalignment θ_{Err} and phase error of the QWP δ_{err} was introduced.

To see how the periodic deviations influence the output quadrature signals, let us assume that the used HWP in Fig. 3.6 possess retardation 150° rather than 180° and the rest of the components and angular setting of the HWP are treated as ideal.

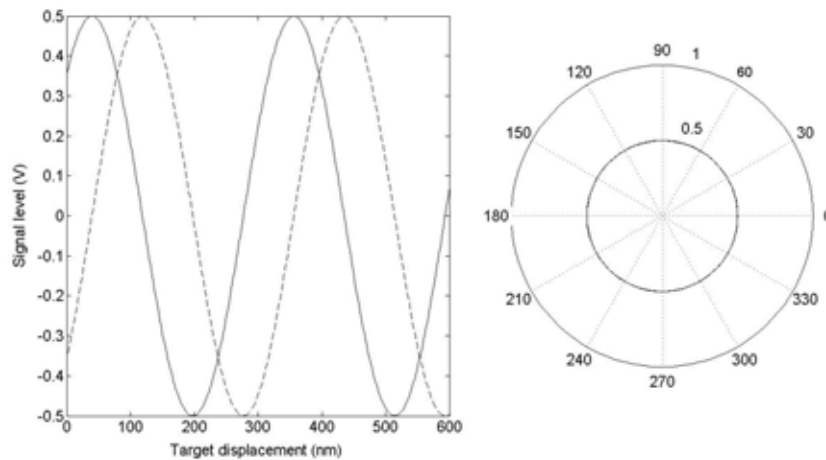


Fig. 3.7. Output quadrature signals (ideal components).

The resultant deformed “quadrature signals” are shown in Fig. 3.8. Note that the retardation error of the HWP mainly influences the phase shift between the quadrature signals and slightly their amplitudes. On the other hand, the effect of a rotational misalignment of the HWP is to change the amplitudes dramatically and the phase shift of the quadrature signals slightly.

When these signals are then used for the determination of the displacement of the measured target, an error of the measurement is introduced. This error can be illustrated in terms of Fig. 3.9. On the left there is shown measured displacement as a function of the actual displacement for two different retardation errors of HWP. The magnitude of the measurement error is then shown in the right part of Fig. 3.9.

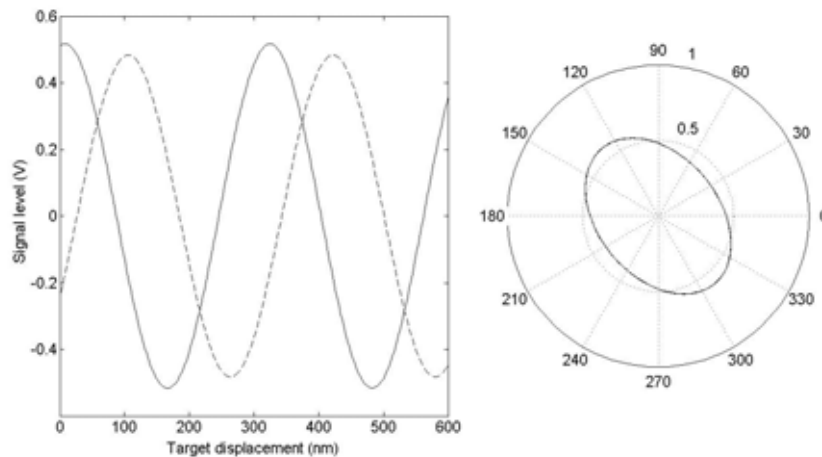


Fig. 3.8. Deformation of quadrature signals due to the non-ideal retardation of the used HWP.

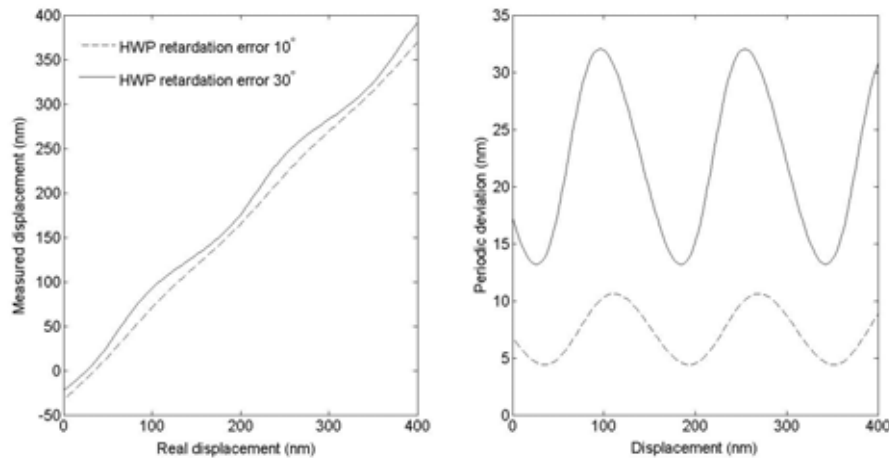


Fig. 3.9. Periodic deviations due to the retardation error of the used HWP.

3.3 Reduction of periodic deviation

In the following discussion, we will investigate polarization imperfection in more details. The influence of polarization imperfections on quadrature signals were already investigated in the literature [8] by another author, as was already mentioned. We will investigate here how periodic deviations can be reduced in the optical part of the vibrometer. Because AGC and DC compensation were integrated in our vibrometer, the only requirement is that the signals are exactly in quadrature. Note, that we will

investigate a slightly different setup from Fig. 3.6. Namely, QWP 2 and the following mirror are exchanged (this does not influence results because of the reciprocity of these devices) and the second modification is that PBS 2 and preceding mirror are exchanged (this requires an additional mirror in order to bring the beams to the detectors). The reason for this is that polarization imperfections of the mirrors after measuring PBS need not be considered. The original setup in Fig. 3.6 was presented because it corresponds to the practical realization (see Fig. 2.19).

Non-ideal measuring polarizing beam splitters

We will first consider the effects of ideal measuring PBS which are misalignment. The angle between lab frame and PBS frame is α_i where index i distinguish both beam splitters. Let us write the states before NBS in the general form

$$|s\rangle = e^{i2kd} (a_s |V\rangle + b_s e^{i\varphi_s} |H\rangle) \text{ and } |r\rangle = a_r |V\rangle + b_r e^{i\varphi_r} |H\rangle \quad (3.21)$$

where $a_i = \cos(\nu_i/2)$, $b_i = \sin(\nu_i/2)$ and angles ν_i , φ_i are spherical coordinates in the Poincare sphere (see Fig. 3.10 on the left for clarity). The power impinging on photodiodes 1 to 4 is then proportional to (NBS was assumed ideal)

$$\begin{aligned} P_1 &\approx \cos^2 \alpha_1 [a_s^2 + a_r^2 + 2a_s a_r \cos(2kd)] + \sin^2 \alpha_1 [b_s^2 + b_r^2 - 2b_s b_r \cos(2kd + \varphi_s - \varphi_r)] \\ P_2 &\approx \cos^2 \alpha_2 [a_s^2 + a_r^2 - 2a_s a_r \cos(2kd)] + \sin^2 \alpha_2 [b_s^2 + b_r^2 + 2b_s b_r \cos(2kd + \varphi_s - \varphi_r)] \\ P_3 &\approx \cos^2 \alpha_1 [b_s^2 + b_r^2 - 2b_s b_r \cos(2kd + \varphi_s - \varphi_r)] + \sin^2 \alpha_1 [a_s^2 + a_r^2 + 2a_s a_r \cos(2kd)] \\ P_4 &\approx \cos^2 \alpha_2 [b_s^2 + b_r^2 + 2b_s b_r \cos(2kd + \varphi_s - \varphi_r)] + \sin^2 \alpha_2 [a_s^2 + a_r^2 - 2a_s a_r \cos(2kd)] \end{aligned} \quad (3.22)$$

If the PBS are perfectly angular adjusted, then $\alpha_i = 0$. The resulting electrical signals $I \approx P_1 - P_2$ and $Q \approx P_4 - P_3$ are in the first approximation (the trigonometric functions before large brackets in (3.22) were developed in Taylor series in the vicinity of the point $\alpha_i = 0$ and the second and higher orders terms were dropped which led to neglecting of second terms in (3.22)) in quadrature if condition $\varphi_s - \varphi_r = \pi/2$ is held. In general, the quadrature signals differ in amplitudes (one amplitude decreases and the second one increases with increasing value of α_i) and possess different dc component. However, these spoiling effects can be eliminated by AGC and DC compensation.

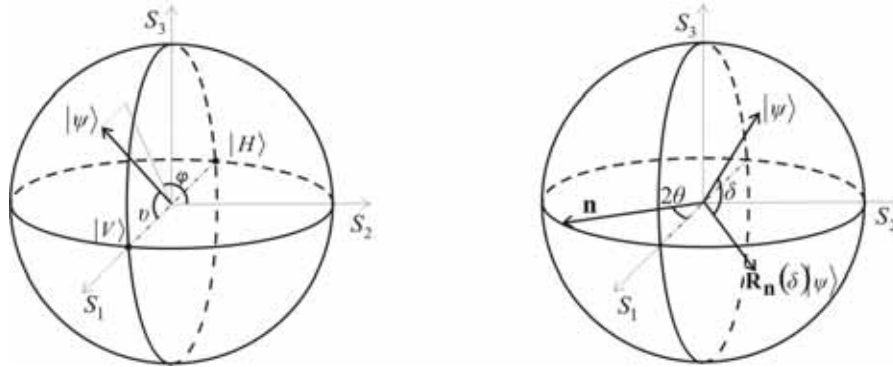


Fig. 3.10. Spherical coordinates of a state vector (left) and illustration of the action of a unitary operator as a rotation.

The more serious effect on the phase difference has non-zero value of extinction coefficient of a real PBS. The resulting signals have similar form to (3.22) with only the difference being that trigonometric functions are replaced by factors A, B , defining extinction coefficient $A/B = e$ (we assumed same extinction coefficient for both PBS). This replacement has the result that the phase of quadrature signals are more affected even for relative high values of e (now the second spoiling terms in (3.22) cannot be dropped).

The effects of a non-ideal PBS are illustrated Fig. 3.11. The first part of the figure shows quadrature signals before AGC and DC compensation when PBS were assumed ideal ($e = \infty$) and angular misalignments were $\alpha_1 = 2^\circ$ and $\alpha_1 = 10^\circ$ (exaggerated value). The second figure shows the signals after AGC and DC compensation. The signal with higher amplitude was reduced to the amplitude of the second one in order to make comparison of signal-noise ratio possible. Finally, the effect of finite value of extinction coefficients ($e = 100$) is illustrated in the last figure in Fig. 3.11. In both cases, the phase difference is 88.7° . To achieve this value, a high rotation misalignment of ideal PBS was introduced and a relatively good extinction coefficient of perfectly aligned PBS was assumed.

The fact that non-ideal extinction coefficient of PBSs influences the phase of the output signals is similar to the phase effect of NBS due to the energy dissipation. Recall the well known fact, that lossless NBS introduces phase difference π between emerging beams. In the case of lossy NBS, the phase difference changes depend on the amount of the losses. In Fig. 3.12, there is shown a slightly rearranged final part of the vibrometer for the case of ideal PBSs and non-ideal PBS with $e = 1$ (this extreme value was chosen for illustrating purposes). The NBS is assumed to be ideal, hence the phase shift between emerging beams from beam splitter is π . We assumed that in the upper arm, constructive interference occurred, and in order to conserve energy, destructive interference occurred in the lower arm. From the energy conservation, one can also deduce the final shift between resulting beams after passing PBSs. Although there is no energy dissipation due to the non-ideal PBS (only finite value of the extinction was assumed, PBS was treated as lossless, however), the non-ideal value of extinction coefficient influences phase difference of the resulting beams. This can be understood as a dissipation of “interference energy” due to the non-ideal polarization overlap between interfering beams after passing PBS.

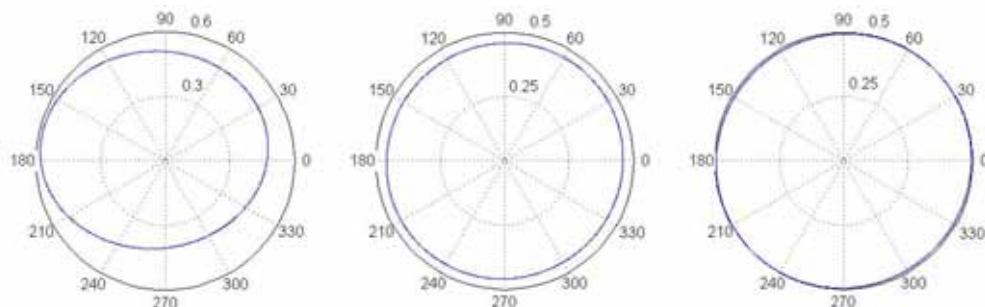


Fig. 3.11. The influence of rotational misalignment of PBS on output quadrature signals before and after AGC and DC compensation (on the left and in the middle) and influence of non-zero value of extinction coefficient.

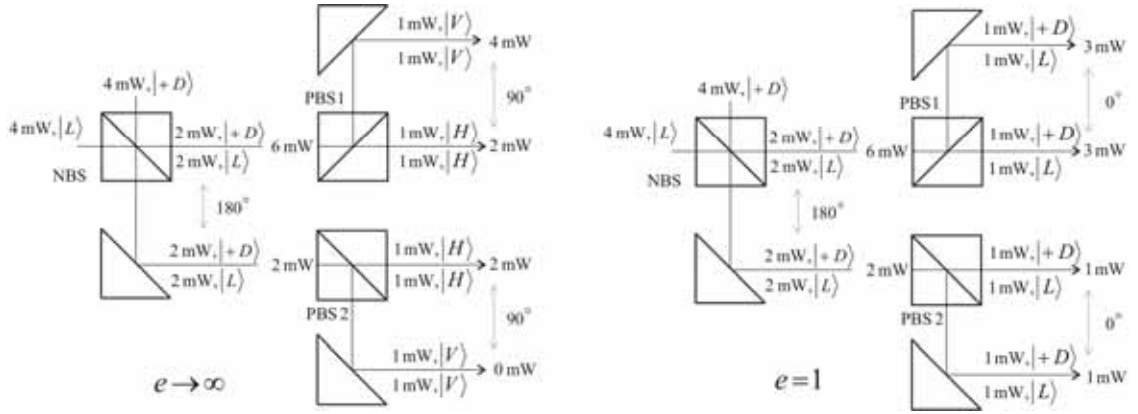


Fig. 3.12. The influence of rotational misalignment of PBS on output quadrature signals before and after AGC and dc compensation (on the left and in the middle) and influence of non-zero value of extinction coefficient.

Non-ideal neutral beam splitter

Next, the effect of a non-ideal NBS will be investigated. The states before NBS are again considered in the form (3.21) and measuring PBS are considered as ideal. The different amplitudes of transmission and reflection coefficients only affect the amount of power distributed in both quadratures but the phase is not influenced. The assumption of the same amplitudes for transmission and reflection coefficients is therefore no loss of generality. The matrices describing the polarization properties of NBS, which were found in [26], in the eigenbasis of the NBS can be written as

$$\begin{aligned}
 \mathbf{M}_{NBS_t} &= \begin{bmatrix} T_p \exp(i\tau_p) & 0 \\ 0 & T_s \exp(i\tau_s) \end{bmatrix} \\
 \mathbf{M}_{NBS_r}^+ &= \begin{bmatrix} R_p \exp(i\rho_p^+) & 0 \\ 0 & R_s \exp(i\rho_s^+) \end{bmatrix} \\
 \mathbf{M}_{NBS_r}^- &= \begin{bmatrix} R_p \exp(i\rho_p^-) & 0 \\ 0 & R_s \exp(i\rho_s^-) \end{bmatrix}.
 \end{aligned} \tag{3.23}$$

Matrix \mathbf{M}_{NBS_t} is used for the transmitted beam, T_p and T_s are modulus of amplitude transmission coefficients for p and s components of electrical field vector and finally τ_p and τ_s are argument of these coefficients. Matrix $\mathbf{M}_{NBS_r}^+$ is used for the reflecting beam when light is incident on NBS in one direction and $\mathbf{M}_{NBS_r}^-$ is used for the reflected beam when light is incident on NBS in the opposite direction. The reflection coefficients are defined in the similar way as transmission coefficients. When a dielectric material is used in NBS, the amplitude coefficients arguments for each component of electric vector are connected with the expression [26]

$$2\tau + \rho^+ + \rho^- = \pi. \tag{3.24}$$

Using relations for the states vectors (3.21), relations (3.23) and (3.24) and assuming that PBS perform ideal projective measurements, one can write for the quadrature signals

$$\begin{aligned}
 I &\approx \sin\left(2kd + \frac{\rho_p^- - \rho_p^+}{2}\right) \sin\left(\tau_p - \frac{\rho_p^- + \rho_p^+}{2}\right) \\
 Q &\approx \sin\left(2kd + \frac{\rho_s^- - \rho_s^+}{2} + \varphi_s - \varphi_r\right) \sin\left(\tau_s - \frac{\rho_s^- + \rho_s^+}{2}\right).
 \end{aligned} \tag{3.25}$$

From (3.25), one can state a requirement for generating true quadrature signals

$$\varphi_s - \varphi_r = -\frac{\pi}{2} + \frac{\rho_p^- - \rho_p^+}{2} - \frac{\rho_s^- - \rho_s^+}{2}. \tag{3.26}$$

In the ideal case $\tau_s = \tau_p = \rho_p^+ = \rho_s^- = 0$ and $\rho_s^+ = \rho_p^- = \pi$ which implies the requirement of $\varphi_s - \varphi_r = -\pi/2$. However, the non-ideal phase properties of NBS require that the phase difference $\varphi_s - \varphi_r$ has a different value in order to generate proper quadrature signals. Next, from (3.25), it can be seen that phase imperfections of NBS reduce amplitudes of quadrature signals.

Now it will be shown that the required phase difference can be achieved by intentional rotational misalignment of QWP 2. To show this, we will assume that components before NBS are ideal hence the state vector before QWP 2 is $|V\rangle$. A general unitary operation can be represented as a rotation by δ about \mathbf{n} axis by the equation

$$\mathbf{R}_n(\delta) = \cos\left(\frac{\delta}{2}\right) \mathbf{I} - i \sin\left(\frac{\delta}{2}\right) (n_x \mathbf{X} + n_y \mathbf{Y} + n_z \mathbf{Z}) \tag{3.27}$$

where $\mathbf{n} = (n_x, n_y, n_z)$ is a real unit vector specifying the rotation (the vector in the case of a retarder lies in the equatorial plane, see Fig. 3.10 on the right), \mathbf{I} is unit matrix and $\mathbf{X}, \mathbf{Y}, \mathbf{Z}$ are Pauli matrices. For the QWP2 one can write

$$\mathbf{R}_n\left(\frac{\pi}{2}\right) = \frac{1}{\sqrt{2}} \mathbf{I} - i \frac{1}{\sqrt{2}} (\sin(2\theta) \mathbf{X} + \cos(2\theta) \mathbf{Z}) \tag{3.28}$$

where θ is the angle between lab frame and device frame in its geometrical interpretation in Poincare sphere is shown in Fig. 3.10. Applying operator (3.28) on vector $|V\rangle$ one obtains phase of the resulting vector in the form

$$\varphi_s = -\frac{\pi}{2} - \arctan(-\cos(2\theta)) \tag{3.29}$$

where properties $\mathbf{X}|V\rangle = |H\rangle$ and $\mathbf{Z}|V\rangle = |V\rangle$ were used. The equation (3.29) can be solved for θ in order to fulfill phase condition (3.26). The first part of Fig 3.13 shows quadrature signals for a real NBP with $\tau_p = 5^\circ$, $\rho_s^+ = \rho_p^- = 170^\circ$, $\rho_s^- = 10^\circ$, $\tau_s = \rho_p^+ = 0^\circ$ (typical values). In the second part, there are illustrated quadrature signals after a rotational alignment of QWP 2 according (3.29) so that the phase was corrected and the signals after AGC are depicted in the last part of the figure.

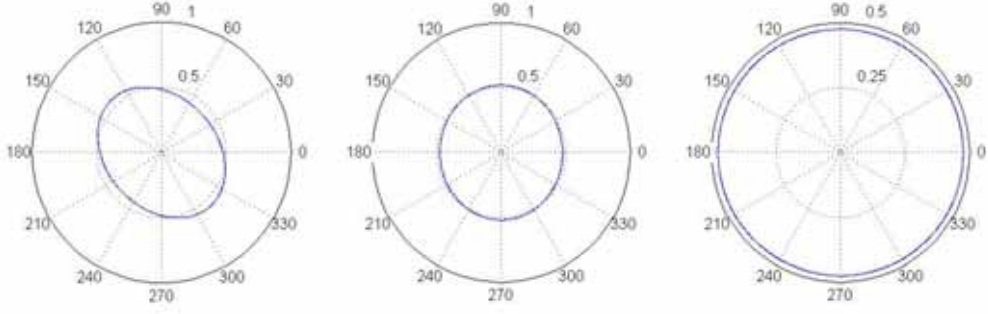


Fig. 3.13. The influence of a real NBS on quadrature signals, phase correction and AGC.

Non-ideal components before neutral beam splitter

Finally it will be shown that all polarization imperfection of components placed before NBP can be, in the first approximation, corrected by a suitable adjustment of QWP 2. The operators describing actions of QWP 2 and HWP in the first approximation (after neglecting second and higher order terms) can be written as

$$\begin{aligned} \mathbf{R}_{n1}\left(\frac{\pi}{2} + \delta_{err1}\right) &= \frac{1}{\sqrt{2}}\left(1 + \frac{\delta_{err1}}{2}\right)\mathbf{I} - i\frac{1}{\sqrt{2}}\left(1 - \frac{\delta_{err1}}{2}\right)(\mathbf{X} + 2\theta_{err1}\mathbf{Z}) \\ \mathbf{R}_{n2}(\pi + \delta_{err2}) &= \frac{\delta_{err2}}{2}\mathbf{I} - i\left(\frac{1}{\sqrt{2}}(1 - 2\theta_{err2})\mathbf{X} + \frac{1}{\sqrt{2}}(1 + 2\theta_{err2})\mathbf{Z}\right) \end{aligned} \quad (3.30)$$

where δ_{err} is a retarder imperfection and θ_{err} is the angle between real and ideal orientation of the retarder. The ideal angles between lab and device frames are 45° and 22.5° for QWP 2 and HWP, respectively. The state vectors before QWP 2 and HWP are, in the first approximation, written as (the general form for state vector (3.21) was developed in Taylor series about the vector $|V\rangle$ and second and higher order terms were neglected)

$$|\psi\rangle_i = |V\rangle + (1 + i\varphi_i)\frac{v_i}{2}|H\rangle \quad i = 1, 2. \quad (3.31)$$

After application operators (3.30) on vectors (3.31) one obtains

$$\begin{aligned} \mathbf{R}_{n1}\left(\frac{\pi}{2} + \delta_{err1}\right)|\psi\rangle_1 &= \\ &= \frac{1}{\sqrt{2}}\left(\begin{array}{l} 1 + \frac{\delta_{err1}}{2} - i2\theta_{err1}\left(1 - \frac{\delta_{err1}}{2}\right) - i(1 + i\varphi_1)\frac{v_1}{2}\left(1 - \frac{\delta_{err1}}{2}\right) \\ (1 + i\varphi_1)\left(1 + \frac{\delta_{err1}}{2}\right)\frac{v_1}{2} - i\left(1 - \frac{\delta_{err1}}{2}\right) + i2\theta_{err1}(1 + i\varphi_1)\frac{v_1}{2}\left(1 - \frac{\delta_{err1}}{2}\right) \end{array}\right) \end{aligned} \quad (3.32)$$

and

$$\begin{aligned} \mathbf{R}_{n2}(\pi + \delta_{err2})|\psi\rangle_2 &= \\ &= \left(\begin{array}{l} \frac{\delta_{err2}}{2} - \frac{i}{\sqrt{2}}(1 + 2\theta_{err2}) - i\frac{(1 + i\varphi_2)v_2}{\sqrt{2}}\frac{1}{2}(1 - 2\theta_{err2}) \\ \frac{\delta_{err2}}{2}(1 + i\varphi_2)\frac{v_2}{2} - \frac{i}{\sqrt{2}}(1 - 2\theta_{err2}) + i\frac{(1 + i\varphi_2)v_2}{\sqrt{2}}\frac{1}{2}(1 + 2\theta_{err2}) \end{array}\right) \end{aligned} \quad (3.33)$$

where additional properties of Pauli matrices $\mathbf{X}|H\rangle = |V\rangle$ and $\mathbf{Z}|H\rangle = -|H\rangle$ were used.

If we assume ideal NBS and measuring PBS, the requirement of quadrature signals demands that the relative phase between states (3.32) and (3.33) is $\pi/2$. After investigation of these equations, it can be seen that this condition is fulfilled when simply

$$\theta_{err1} = \frac{\nu_1}{2}. \quad (3.34)$$

To illustrate these results, the first two PBS were assumed to be non-ideal. The resulting quadrature signals before correction and after the correction according to (3.34) are depicted in Fig. 3.14. The last part of the figure shows phase corrected signals after AGC.

The result (3.34) is more remarkable than it seems. It is because that θ_{err1} is independent of other imperfections, especially independent of θ_{err2} which is misalignment of HWP. This independency suggests that θ_{err2} can be used to equal power of both quadrature signals.

Indeed, the two rows in (3.32) are power contributions to the both resulting quadrature signals due to the signal beam. Similarly two rows in (3.33) are reference beam contributions. The loss of the power in one quadrature due to the phase compensation in signal beam can be then compensated by redistribution of the power of reference beam which can be done by controlling parameter θ_{err2} . The exact analytical formula how this parameter needs to be chosen in order to achieve the same quadratures powers can be derive from (3.32) and (3.33). However, such exact formula has almost no practical importance because it depends on all imperfection parameters appearing in (3.32) and (3.33). For this reason, we verified the idea of power compensation only experimentally which is the subject of the next section.

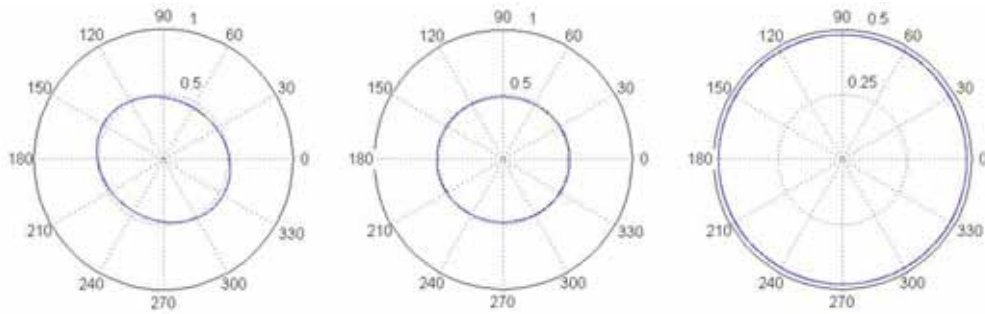


Fig. 3.14. Phase correction by a suitable adjustment of QWP 2.

3.4 Experimental verification

The previous results were obtained using computer simulation of the vibrometer. Direct experimental verification is not easy due to the plethora of parameters which need to be measured. This includes not only devices parameters itself (eigenvalues determination) but also angles which specify connections between devices frames and lab frame. For these reasons, we only present photos of quadrature signals which were

obtained after adjusting all optical elements (Fig. 3.15 on the left) and signals which were obtained exactly at same conditions only with the difference that QWP 2 was intentionally rotationally misalignment in order to obtain real quadrature signals (Fig. 3.15 on the right). The effects of the changing of amplitudes of the signals due to the correction can be observed (illustrated signals are before applying of AGC).

Next we demonstrate rotational misalignment of measuring PBS. We chose this imperfection because it can be controlled in simple way. Namely, it influences the directions of reference and signal beam in the same way, so interference pattern on the detector will not change and there is no need to readjust the other components (except final mirrors, which is easy to perform). After bringing both beams in interference and readjusting QWP2 and HWP in order to obtain quadrature signals in real quadrature and with the same magnitude (see Fig. 3.16 on the left) we intentionally misalignment measuring beamsplitter PBS1, approximately by 10° (this was only estimated value). The resulting quadrature signals are depicted on the right part of the figure. This figure can be compared with the Fig. 3.11 where a similar misalignment was simulated.

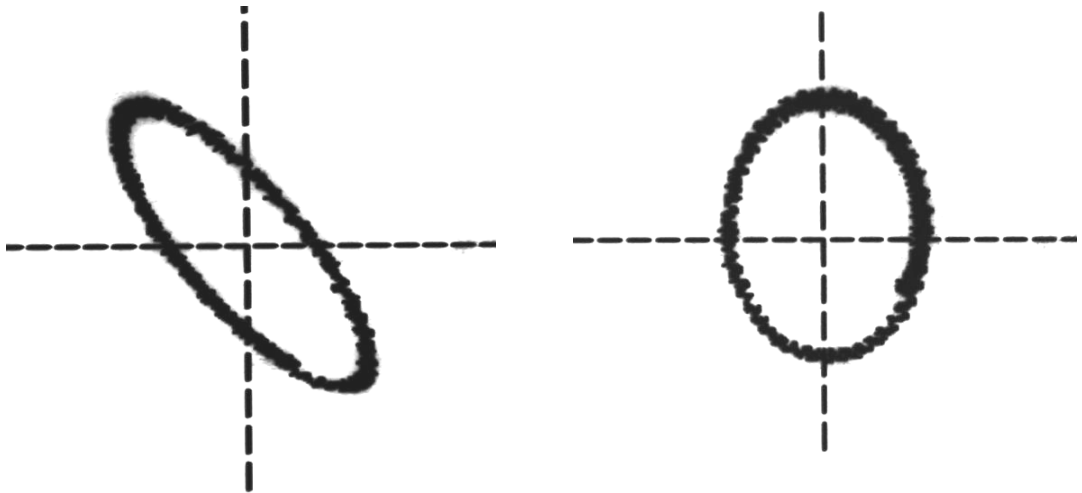


Fig. 3.15. Quadrature signals from the real vibrometer, before and after phase correction.



Fig. 3.16. Experimental illustration of amplitude correction and rotational misalignment of the PBS 1.

In order to appreciate the possibility to eliminate periodic deviations directly in the optical part of the vibrometer, which becomes important when only analog electronics in the vibrometer is used, we state the final algorithm which needs to be implemented in order to obtain velocity from the quadrature signals [27]

$$v = \frac{\lambda}{4\pi} \frac{Q \cdot \dot{I} - I \cdot \dot{Q}}{I^2 + Q^2} \quad (3.35)$$

where λ is the wavelength of the used light and Q and I denote quadrature time-varying signals. The implementation of the algorithm using LabVIEW 8.2 FPGA Module was reported in [27].

However, as was discussed in this chapter used optical components in the interferometric setup non-ideally influence the polarization states of the beams which lead to the generating signals which are not in real quadrature. Then modified version of the algorithm (3.35) is introduced as

$$v = \frac{\lambda}{4\pi} \frac{(Q \cdot \dot{I} - I \cdot \dot{Q}) \cos(\Delta\varphi)}{I^2 + Q^2 - 2IQ \sin(\Delta\varphi)} \quad (3.36)$$

where time-constant phase error $\Delta\varphi$ between non-ideal quadrature signals was introduced. Using digital rather than analog technology in the signal processing part of the vibrometer offers an easy utilization of the modified algorithm. The results of implementation of the original and modified algorithm using LabVIEW 8.2 FPGA Module are shown in Fig. 3.17 where a piezocrystal driven by sinus signal was used as vibrating target. Time constant phase error was $\Delta\varphi = 10^\circ$. We only wish to illustrate the different forms of the resulting signal so some relative units were used.

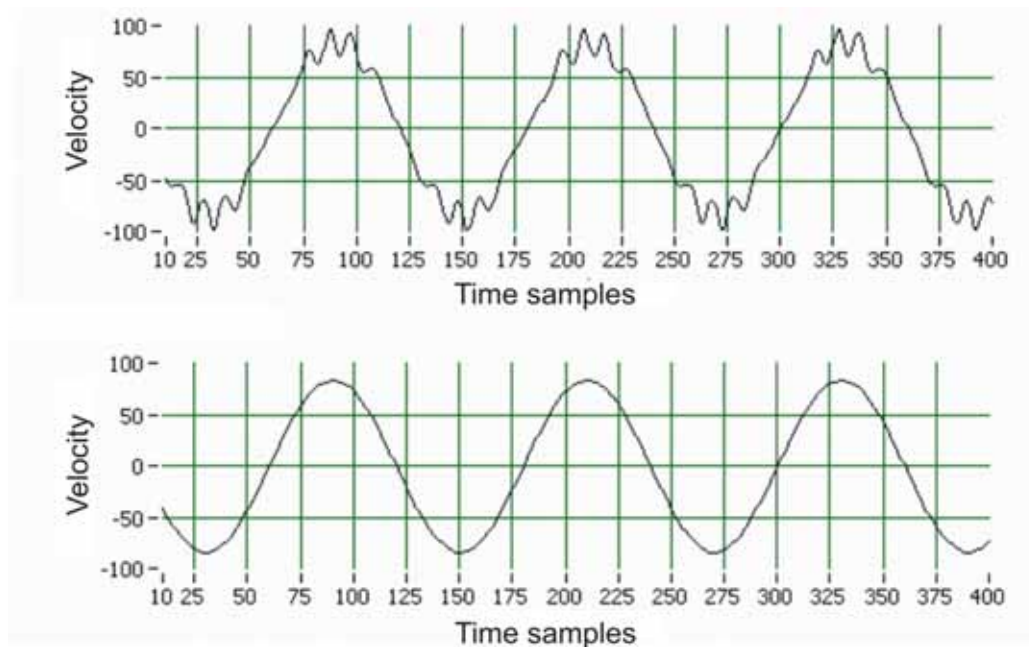


Fig. 3.17. Synthetic Heterodyne Demodulation (upper part) and its modified version (lower part).

3.5 Chapter summary

Let us summarize the results. All polarization imperfection of the components placed before measuring PBS can be, in the first approximation, compensated by an intentionally rotational misalignment of QWP 2. The phase imperfection of NBS can be corrected again by rotational misalignment of QWP 2. The angular misalignments of measuring PBS can be, in the first approximation, neglected. Finite value of extinction coefficients has a crucial effect on the quality of the quadrature signals. This spoiling effect cannot be compensated in the optical part of the interferometer. These results were expected because the measuring PBSs (accompanied by photodiodes) perform true measurements on the states and the components which precede these PBS perform a pure rotation of the states in the Poincare sphere. Finally, we conclude that by an additional rotational misalignment of HWP output quadrature signals can have not only required phase shift 90° but also same amplitudes.

4 Quantum description of optical devices

A quantum-mechanical description of the phase shifters, retarders, mirrors and beam splitters is given in this section. The description is then applied on two types of states; on a coherent state, a classical-like state, and on a number state, hence the strict quantum state. The quantum description of a beam splitter can be found in the literature. However the description does not treat with the polarization concept. The main aim of this section is to introduce quantum description of an arbitrary oriented retarder and give a description of a beam splitter which treats with the polarization. These results were published by the author in the similar form as they are presented in [28].

4.1 Coherent and number states

In this section we introduce the two most common states used in the quantum optics. Used relations in this section are taken from [29].

A coherent state is the eigenstate of the annihilation operator

$$\hat{a}|\alpha\rangle = \alpha|\alpha\rangle \quad (4.1)$$

and can be generated from the vacuum state using the displacement operator

$$|\alpha\rangle = \hat{D}(\alpha)|0\rangle = \exp(\alpha\hat{a}^H - \alpha^*\hat{a})|0\rangle \quad (4.2)$$

where the symbol X^H denotes the Hermitian conjugate. A normalized coherent state can be expressed in the number state basis as

$$|\alpha\rangle = \exp(-|\alpha|^2/2) \sum_{n=0}^{\infty} \frac{\alpha^n}{\sqrt{n!}} |n\rangle. \quad (4.3)$$

Note that $|\alpha|$ is related to the amplitude of the field.

Number states are generated from the vacuum according to

$$|n\rangle = \frac{1}{\sqrt{n!}} (\hat{a}^H)^n |0\rangle. \quad (4.4)$$

The time evolution of the number states is given by

$$|n(t)\rangle = \exp(-in\omega t) |n(0)\rangle \quad (4.5)$$

where we neglected the global factor $\exp(-i\omega t/2)$, the contribution from the vacuum (does not influence the dynamic of the system).

4.2 Phase shifter and retarder

A phase shifter \hat{P} acts like time evolution. It adds an extra time delay $\Delta t = (n_p - n_0)\Delta z / c$ which depends on refractive index n_p and thickness Δz of the shifter. The symbol n_0 denotes the refractive index of the environment. In the following, the symbol n denotes the eigenvalue of energy eigenstate $|n\rangle$. The dependency on the refractive index of the shifter is absorbed in Δt . Hence the action of the shifter on a number state is

$$\hat{P}|n\rangle = \exp(in\theta)|n\rangle \quad (4.6)$$

where $\theta = \omega\Delta t$ was introduced and represents an extra phase due to the shifter. Relation (4.6) can be rewritten in the operator form as (due to the fact that n represents eigenvalue of $|n\rangle$)

$$\hat{P}|n\rangle = \exp(i\hat{n}\theta)|n\rangle \quad (4.7)$$

where the number operator $\hat{n} = \hat{a}^H \hat{a}$ was introduced. Hence, the shifter is generally described by the following unitary operator

$$\hat{P} = \exp(i\hat{n}\theta). \quad (4.8)$$

When the shifter acts on the coherent state, one obtains

$$\hat{P}|\alpha\rangle = \exp(-|\alpha|^2/2) \sum_n \frac{(\alpha \exp(i\omega\Delta t))^n}{\sqrt{n!}} |n\rangle = |\alpha \exp(i\theta)\rangle. \quad (4.9)$$

Note, that the time evolution of a coherent state is given by

$$|\alpha(t)\rangle = |\alpha \exp^{-i\omega t}\rangle \quad (4.10)$$

where the contribution from the vacuum was neglected.

Next, we describe the action of a retarder by extending the foregoing considerations through the assumption that different phase shifts are experienced for two eigenstates. Thus, a retarder is, on the contrary from phase shifter able to change the polarization and one needs to introduce an extra degree of freedom to treat with the polarization.

Retarder in the lab frame

First we consider the situation where the lab frame and frame of the retarder are in the coincidence (so fast axis (FA) of the retarder is parallel to the y -axis as is depicted in Fig. 4.1 on the left).

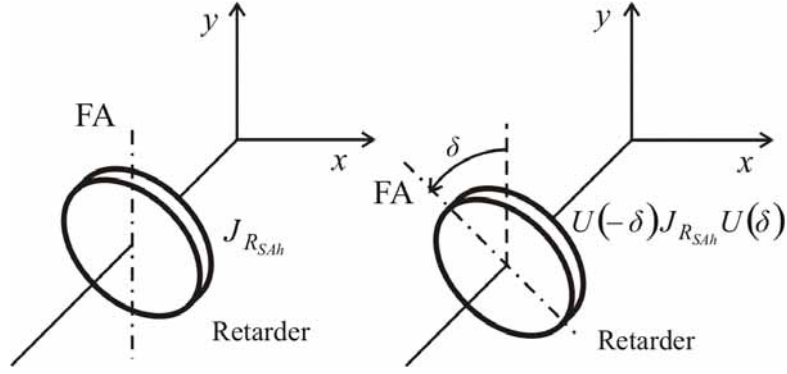


Fig. 4.1. Placing of a retarder. On the left, the lab frame coincides with the retarder frame. On the right the lab frame differs from the retarder frame.

The action of a retarder (slow axis oriented parallel to x -axis) is described by using Jones matrix (expressed in the x - y basis) in the form

$$\mathbf{J}_{R_{SAh}} = \begin{bmatrix} 1 & 0 \\ 0 & \exp(-i\theta) \end{bmatrix}, \quad \theta > 0 \quad (4.11)$$

where θ denotes the phase difference between both eigenvalues of the retarder (the relative phase shift). In the Jones formalism is matrix (4.11) applied on the input vector where each entry of the vector describes the orthogonal (respect with the polarization) electric field component

$$\begin{pmatrix} E'_x \\ E'_y \end{pmatrix} = \begin{pmatrix} 1 & 0 \\ 0 & \exp(-i\theta) \end{pmatrix} \begin{pmatrix} E_x \\ E_y \end{pmatrix}. \quad (4.12)$$

The usual way for obtaining a quantum description is replacing the classical complex field amplitudes by a set of annihilation operators as

$$\begin{pmatrix} \hat{a}'_x \\ \hat{a}'_y \end{pmatrix} = \begin{pmatrix} 1 & 0 \\ 0 & \exp(-i\theta) \end{pmatrix} \begin{pmatrix} \hat{a}_x \\ \hat{a}_y \end{pmatrix}. \quad (4.13)$$

Now we can introduce new basis states as

$$|n_x, n_y\rangle = (n_x!n_y!)^{-1/2} (\hat{a}_x^H)^{n_x} (\hat{a}_y^H)^{n_y} |0,0\rangle \quad (4.14)$$

where an extra degree of freedom was introduced in order to include polarization. A basis state $|n_x, n_y\rangle$ can be interpreted as the state containing exactly n_x x -polarized photons and n_y y -polarized photons.

The input and output modes of a retarder are related according to (using (4.13))

$$\begin{aligned} \hat{a}'_x &= \hat{a}_x \\ \hat{a}'_y &= \exp(-i\theta)\hat{a}_y. \end{aligned} \quad (4.15)$$

Note that the familiar commutations relations

$$[\hat{a}_i, \hat{a}_j^H] = \delta_{ij}, [\hat{a}_i, \hat{a}_j] = 0 = [\hat{a}_i^H, \hat{a}_j^H] \quad (4.16)$$

are still satisfied by transformation (4.15) (indexes i, j represent input and output modes for each polarization).

Relation (4.15) may be written in Heisenberg picture as

$$\begin{pmatrix} \hat{a}'_x \\ \hat{a}'_y \end{pmatrix} = \hat{R}^H \begin{pmatrix} \hat{a}_x \\ \hat{a}_y \end{pmatrix} \hat{R} \quad (4.17)$$

where \hat{R} is an unitary operator representing a retarder. The operator satisfying (4.17) and (4.15) was found in the form

$$\hat{R} = \exp(-i\theta \hat{a}_y^H \hat{a}_y). \quad (4.18)$$

As an example let us act a retarder on input state which consists of one photon polarized diagonally

$$\begin{aligned} \frac{1}{\sqrt{2}}(\hat{a}_x^H + \hat{a}_y^H)|0_x, 0_y\rangle &= \frac{1}{\sqrt{2}}(|1_x, 0_y\rangle + |0_x, 1_y\rangle) \\ \xrightarrow{R} \frac{1}{\sqrt{2}}(|1_x, 0_y\rangle + \exp(-i\theta)|0_x, 1_y\rangle) \end{aligned} \quad (4.19)$$

where we used inverse relation (from (4.15))

$$\begin{aligned} \hat{a}_x^H &= (\hat{a}'_x)^H \\ \hat{a}_y^H &= \exp(-i\theta)(\hat{a}'_y)^H. \end{aligned} \quad (4.20)$$

Through investigation of (4.19), it can be seen that in the case of quarter-wave plate ($\theta = \pi/2$), one obtains from a photon initially diagonally polarized photon which is right-handed polarized.

Retarder in the device frame

Generally the retarder is placed as shown on the right in Fig. 4.1. Then the Jones matrix $\mathbf{J}_{R_{SAh}}$ is undergone the active transformation

$$\mathbf{U}(-\delta)\mathbf{J}_{R_{SAh}}\mathbf{U}(\delta) \quad (4.21)$$

where

$$\mathbf{U} = \begin{pmatrix} \cos \delta & \sin \delta \\ -\sin \delta & \cos \delta \end{pmatrix}. \quad (4.22)$$

Note that $\mathbf{U}^H(\delta) = \mathbf{U}(-\delta)$. Working out the multiplication in (4.21) one again can associate the fields with annihilation operators as

$$\begin{aligned} \hat{a}'_x &= \cos^2 \delta(\hat{a}_x) + \cos \delta \sin \delta(\hat{a}_y) + \exp(-i\theta)\sin^2 \delta(\hat{a}_x) - \\ &\quad - \exp(-i\theta)\sin \delta \cos \delta(\hat{a}_y) \end{aligned} \quad (4.23)$$

and

$$\begin{aligned} \hat{a}'_y &= \exp(-i\theta)\cos^2 \delta(\hat{a}_y) + \cos \delta \sin \delta(\hat{a}_x) + \sin^2 \delta(\hat{a}_y) - \\ &\quad - \exp(-i\theta)\sin \delta \cos \delta(\hat{a}_x). \end{aligned} \quad (4.24)$$

Note that commutation relations (4.16) are for the operators (4.23) and (4.24) again satisfied. Relations (4.23) and (4.24) can be formally written as

$$\begin{pmatrix} \hat{a}'_x \\ \hat{a}'_y \end{pmatrix} = \hat{R}^H \hat{U}^H \begin{pmatrix} \hat{a}_x \\ \hat{a}_y \end{pmatrix} \hat{U} \hat{R} \quad (4.25)$$

where \hat{R} is given by (4.18) and

$$\hat{U} = \exp(\delta(\hat{a}_x^H \hat{a}_y - \hat{a}_x \hat{a}_y^H)). \quad (4.26)$$

Equation (4.26) is the quantum analogy of (4.22). Hence, the unitary operator describing arbitrary placed retarder is $\hat{U}\hat{R}$. As an example, let us suppose $\delta = \pi/4$, $\theta = \pi/2$ and input state $|2_x, 0_y\rangle$. Using (4.23) and (4.24) one obtains

$$\hat{a}_x^H = \frac{1}{\sqrt{2}}((\hat{a}'_x)^H + i(\hat{a}'_y)^H). \quad (4.27)$$

Then

$$\begin{aligned} |2,0\rangle &\xrightarrow{R} ((\hat{a}'_x)^H + i(\hat{a}'_y)^H)^2 |0,0\rangle = |2,0\rangle + |0,2\rangle + 2i|1,1\rangle = \\ &= (|1,0\rangle + i|0,1\rangle) \otimes (|1,0\rangle + i|0,1\rangle) \equiv |0_R, 2_L\rangle. \end{aligned} \quad (4.28)$$

And generally $|n_x, 0_y\rangle \xrightarrow{R} |0, n_L\rangle$. So, we obtained left-handed polarized photons as expected. As a last example suppose input x -polarized coherent state and the properties of the retarder from the previous example. Then

$$\begin{aligned} \exp(\alpha \hat{a}_x^H - \alpha^* \hat{a}_x) |0_x, 0_y\rangle &\xrightarrow{R} \exp\left(\frac{1}{\sqrt{2}} \alpha (\hat{a}'_x)^H - \frac{1}{\sqrt{2}} \alpha^* \hat{a}'_x\right) \cdot \\ \cdot \exp\left(\frac{i}{\sqrt{2}} \alpha (\hat{a}'_y)^H - \frac{-i}{\sqrt{2}} \alpha^* \hat{a}'_y\right) &|0_x, 0_y\rangle = \left| \frac{\alpha}{\sqrt{2}_x}, \frac{i\alpha}{\sqrt{2}_y} \right\rangle. \end{aligned} \quad (4.29)$$

So, we obtained left-handed polarized beam.

4.3 Mirror

A common mirror has for normal incidence Jones matrix in the form

$$\mathbf{J}_{Mirror} = \begin{bmatrix} -1 & 0 \\ 0 & 1 \end{bmatrix} \quad (4.30)$$

in the accordance with the Frenel's equations (see Fig. 4.2).

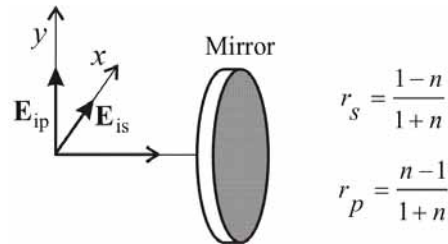


Fig. 4.2. Used notation for the components of the incident field and Frenel's equations.

Hence the action of a mirror is the same as half-wave plate (HWP) when the fast axis is parallel to x -axis. The mirror is then described by the unitary operator satisfying

$$\hat{R} = \exp(i\pi\hat{a}_x^H\hat{a}_x) \quad (4.31)$$

where we neglected the global phase factor $\pi/2$ (is same for both field components) due to the reflection. Now we apply the mirror on a coherent left-handed polarized light

$$\begin{aligned} \left| \frac{\alpha}{\sqrt{2}}_x, \frac{i\alpha}{\sqrt{2}}_y \right\rangle &\xrightarrow{M} \exp\left(\frac{-1}{\sqrt{2}}\alpha(\hat{a}'_x)^H - \frac{-1}{\sqrt{2}}\alpha^*\hat{a}'_x\right) \cdot \\ &\cdot \exp\left(\frac{i}{\sqrt{2}}\alpha(\hat{a}'_y)^H - \frac{-i}{\sqrt{2}}\alpha^*\hat{a}'_y\right) |0_x, 0_y\rangle = \left| \frac{-\alpha}{\sqrt{2}}_x, \frac{i\alpha}{\sqrt{2}}_y \right\rangle \end{aligned} \quad (4.32)$$

where we used (4.15) with setting $\theta = \pi$. Left-handed beam is converted to the right-handed beam due to the reflection. This is obvious because the Jones matrix (4.30) in the left-right handed (helicity) basis is expressed as

$$\mathbf{J}'_{Mirror} = \begin{bmatrix} 0 & 1 \\ 1 & 0 \end{bmatrix}. \quad (4.33)$$

4.4 Non-polarizing beamsplitter

Classical scalar description of non-polarizing beam splitter

The classical scalar (input and output beams are assumed to have a common linear polarization) description of a non-polarizing beam splitter (NBS) can be found in [29]. The output fields are related to the input fields by relation

$$\begin{bmatrix} E_2 \\ E_3 \end{bmatrix} = \begin{bmatrix} t_0 & r_1 \\ r_0 & t_1 \end{bmatrix} \begin{bmatrix} E_0 \\ E_1 \end{bmatrix} \quad (4.34)$$

where the meaning of reflection and transmission coefficients is illustrated in Fig. 4.3.

The phases of reflection and transmission coefficients are related via (formula derived by considering the energy conservation [29])

$$\arg(r_0) + \arg(r_1) - \arg(t_0) - \arg(t_1) = \pm\pi. \quad (4.35)$$

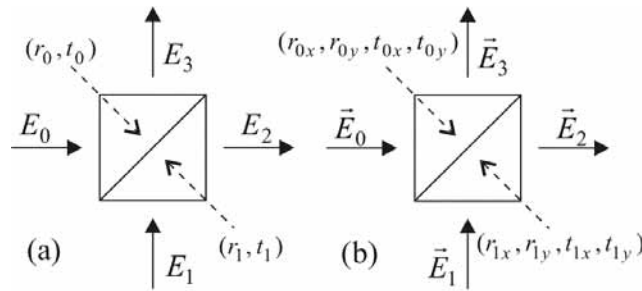


Fig. 4.3. Classical scalar (a) and vector (b) description of NBS.

Note that there are two choices of phases which have different observable effects. These choices depend on the construction of the beam splitter [30]. For a beam splitter cube, the conventional choice is

$$\arg(r_0) = \arg(r_1) = \arg(t_0) = 0 \text{ and } \arg(t_1) = \pi \quad (4.36)$$

whereas for a single dielectric layer beam splitter, the conventional choice is

$$\arg(t_0) = \arg(t_1) = 0 \text{ and } \arg(r_0) = \arg(r_1) = \pi/2. \quad (4.37)$$

Of course, the phase choice in (4.36) and (4.37) is not unique. Hence for a 50:50 beam splitter cube one can write

$$E_2 = \frac{E_0 + E_1}{\sqrt{2}} \text{ and } E_3 = \frac{E_0 - E_1}{\sqrt{2}}. \quad (4.38)$$

Classical vector description of non-polarizing beam splitter

In the previous subsection, it was assumed that all beams have the common linear polarization. The reason is following. In general, an optical device divides an incident field into two parts, the eigenstates (eigenvectors) of the optical device. And these eigenstates are treated independently. As an example, we measured Jones matrix of NBS 10701A in the form

$$NBS_t = \begin{bmatrix} 0.69 & 0 \\ 0 & 0.73 \exp(-3.5^\circ i) \end{bmatrix} \text{ and } NBS_r = \begin{bmatrix} 0.67 & 0 \\ 0 & 0.62 \exp(172.9^\circ i) \end{bmatrix} \quad (4.39)$$

for the transmitted and the deflected (reflected) beam, respectively. Matrices (4.39) are expressed in the linear basis. Hence matrix component NBS_{11} tells us how evolves x component of the field. From (4.39), one can guess an ideal 50:50 NBS as

$$NBS_t = \frac{1}{\sqrt{2}} \begin{bmatrix} 1 & 0 \\ 0 & 1 \end{bmatrix} \text{ and } NBS_r = \frac{1}{\sqrt{2}} \begin{bmatrix} 1 & 0 \\ 0 & -1 \end{bmatrix}. \quad (4.40)$$

However in general, the input beams are in the superposition of eigenstates of NBS. Hence the reflection and transmission coefficients are different for x and y -polarization. Now, we suppose a symmetric beam splitter cube ($|r_0| = |r_1|$ and $|t_0| = |t_1|$). Then the vector description of a beam splitter cube can be expressed as

$$\begin{aligned} \vec{E}_2 &= NBS_t \cdot \vec{E}_0 + NBS_r \cdot \vec{E}_1 \\ \vec{E}_3 &= NBS_r \cdot \vec{E}_0 - NBS_t \cdot \vec{E}_1 \end{aligned} \quad (4.41)$$

Note, that for non-symmetric beam splitter cube, one needs to measure Jones matrices for both input beams (hence the second formula in (4.41) will obtain different Jones matrices from the first formula).

If we now assumed that input beams are both x -polarized

$$\vec{E}_0 = \begin{pmatrix} E_0 \\ 0 \end{pmatrix} \text{ and } \vec{E}_1 = \begin{pmatrix} E_1 \\ 0 \end{pmatrix} \quad (4.42)$$

and next we suppose an ideal 50:50 NBS, using (4.40) and (4.41) we arrive to (4.38).

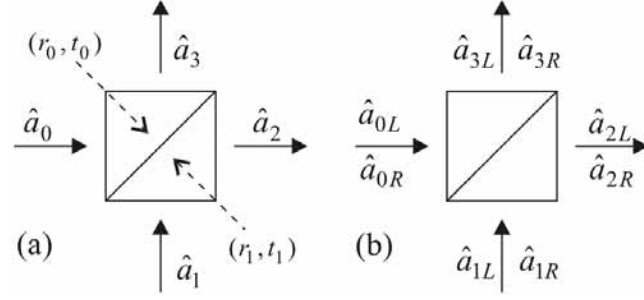


Fig. 4.4. Quantum scalar (a) and vector (b) description of NBS.

Quantum non-polarization description of NBS

The quantum scalar description of a beam splitter is given in [29], [30]. The electric field vectors in (4.34) are replaced by annihilation operators (Fig. 4.4(a))

$$\begin{bmatrix} \hat{a}_2 \\ \hat{a}_3 \end{bmatrix} = \begin{bmatrix} t_0 & r_1 \\ r_0 & t_1 \end{bmatrix} \begin{bmatrix} \hat{a}_0 \\ \hat{a}_1 \end{bmatrix}. \quad (4.43)$$

Formula (4.43) can be formally written as

$$\begin{pmatrix} \hat{a}_2 \\ \hat{a}_3 \end{pmatrix} = \hat{B}^H \begin{pmatrix} \hat{a}_0 \\ \hat{a}_1 \end{pmatrix} \hat{B} \quad (4.44)$$

where the unitary operator of a 50:50 beam splitter has a form [30]

$$\hat{B} = \exp\left(i\frac{\pi}{4}(\hat{a}_0^H \hat{a}_1 + \hat{a}_0 \hat{a}_1^H)\right). \quad (4.45)$$

If a beam splitter is acted on the state $|1\rangle_0|1\rangle_1$ (in both inputs is exactly one photon), one obtains

$$|1\rangle_0|1\rangle_1 \xrightarrow{B} \frac{i}{\sqrt{2}}(|2\rangle_2|0\rangle_3 + |2\rangle_3|0\rangle_2). \quad (4.46)$$

The possibilities $|1\rangle_0|0\rangle_1$ and $|0\rangle_0|1\rangle_1$ do not occur due to the fact that the processes shown in Fig. 4.5 are indistinguishable and interfere destructively.

For example, for input coherent states and a single dielectric layer beam splitter one obtains

$$|\alpha\rangle_0|\beta\rangle_1 \xrightarrow{B_1} \left| \frac{\alpha + i\beta}{\sqrt{2}} \right\rangle_2 \left| \frac{i\alpha + \beta}{\sqrt{2}} \right\rangle_3 \quad (4.47)$$

and for a beam splitter cube, made of a right angle prisms, one obtains

$$|\alpha\rangle_0|\beta\rangle_1 \xrightarrow{B_1} \left| \frac{\alpha + \beta}{\sqrt{2}} \right\rangle_2 \left| \frac{-\alpha + \beta}{\sqrt{2}} \right\rangle_3. \quad (4.48)$$

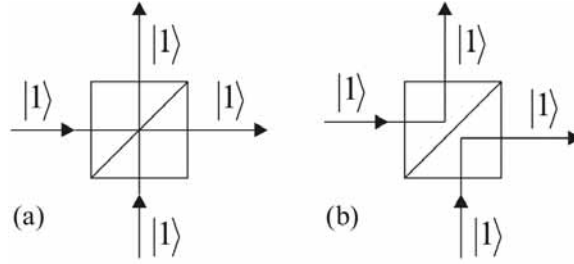


Fig. 4.5. Two indistinguishable processes.

Quantum polarization description of NBS

From (4.40), one can see that for the ideal beam splitter, there is the change of the polarization for the reflected beam. Note relation (4.40) differs from (4.30) only in the global factor which is for us unimportant now (has no observable effects).

Thus, if we assume that the photon polarization is swapped under a reflection from left-handed to right-handed and vice versa (see Fig. 4.6) then the processes in Fig. 4.5 are truly indistinguishable only if the inputs of the beam splitter are both x or y -linearly polarized.

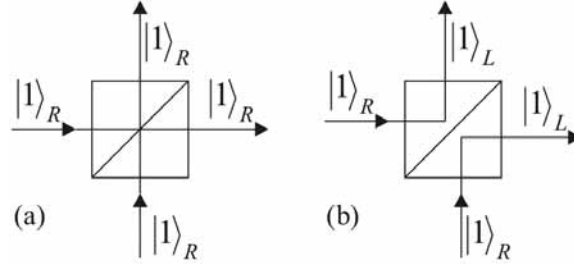


Fig. 4.6. Two distinguishable processes.

Thus, for the complete description one needs to introduce an extra degree of freedom to treat with the polarization. For this purpose, we use the following definition (applicable only for a lossless beam splitter) for the reflection and transmission coefficients

$$\cos \theta = |r| \quad \text{and} \quad \sin \theta = |t| \quad (4.49)$$

where we set $|r_0| = |r_1| = |r|$ and $|t_0| = |t_1| = |t|$ (assuming symmetric beam splitter). Note that the angle θ has no geometrical interpretation. For instance $\theta = \pi/4$ represents a 50:50 beam splitter.

In Fig. 4.4(b) there is shown the new set of operators for the input and output modes. In this section, we use right-handed and left-handed basis. In this basis the transmitted photon is left untouched and the reflected photon is swap from $R \rightarrow L$ and vice versa. Then the action of a beam splitter cube can be expressed as

$$\begin{aligned} \hat{B} \hat{a}_{0R}^H \hat{B}^H &= \hat{a}_{2L}^H \cos \theta + \hat{a}_{3R}^H \sin \theta \\ \hat{B} \hat{a}_{0L}^H \hat{B}^H &= \hat{a}_{2R}^H \cos \theta + \hat{a}_{3L}^H \sin \theta \\ \hat{B} \hat{a}_{1R}^H \hat{B}^H &= -\hat{a}_{2R}^H \sin \theta + \hat{a}_{3L}^H \cos \theta \\ \hat{B} \hat{a}_{1L}^H \hat{B}^H &= -\hat{a}_{2L}^H \sin \theta + \hat{a}_{3R}^H \cos \theta. \end{aligned} \quad (4.50)$$

As an example, we suppose the following input states of a beam splitter

$$\begin{aligned}
 & |1_R, 0_L\rangle_0 |1_R, 0_L\rangle_1 \xrightarrow{B} \hat{B} |1_R, 0_L\rangle_0 |1_R, 0_L\rangle_1 = \\
 & = \hat{B}(\hat{a}_{0R}^H) \hat{B}^H \hat{B}(\hat{a}_{1R}^H) \hat{B}^H \hat{B} |0_R, 0_L\rangle_0 |0_R, 0_L\rangle_1 = \\
 & = -\cos\theta \sin\theta |1_R, 1_L\rangle_2 |0_R, 0_L\rangle_3 + \cos^2\theta |0_R, 1_L\rangle_2 |0_R, 1_L\rangle_3 \\
 & \quad - \sin^2\theta |1_R, 0_L\rangle_2 |1_R, 0_L\rangle_3 + \cos\theta \sin\theta |0_R, 0_L\rangle_2 |1_R, 1_L\rangle_3
 \end{aligned} \tag{4.51}$$

where we used the unitary property $\hat{B}^H \hat{B} = 1$ and $\hat{B} |0_R, 0_L\rangle_0 |0_R, 0_L\rangle_1 = |0_R, 0_L\rangle_2 |0_R, 0_L\rangle_3$. From (4.51), it is clear that if we do not treat with the polarization and assume 50:50 beam splitter ($\theta = \pi/4$), the two middle terms in (4.51) cancel and we obtain a relation similar to (4.46) (the different phases are due to the fact that in (4.46), we used a single dielectric layer as a beam splitter and in (4.51), beam splitter cube).

4.5 Chapter summary

The main goal of this section was to give quantum description of an arbitrary placed retarder and a vector description (description which treats with the polarization) of a beam splitter.

The derivation was based on the analogy with Jones matrix calculus where electric fields vectors were replaced by annihilation operators.

In quantum case, we supposed lossless components (no interaction with the environment) to represent them by unitary operators. This is the fundamental difference in comparison with Jones matrix concept where one can represent the loss optical device by Jones matrix. This difference is due to the fact that Jones concept arises from Maxwell's equations hence analogy between Jones calculus and quantum description can't be taken too seriously. The description of loss systems in quantum domain needs to introduce an environment which interacts with the principal system.

Jones calculus can't be used when the experiments are treated in the quantum domain. The quantum description of retarders, phase shifters and beam splitters is needed for a single photon transmission and quantum computation where mentioned devices are used for manipulation with single photons.

5 Polarization imperfections in Polarimetry

The photoelasticity is one of the oldest forms of interferometric measurement. It involves the observation of fringe patterns for determination of stress-induced birefringent. Photoelastic stress was first investigated by so-called plane polariscope (also called polarimeter). Plane polariscope consists of a light source, polarizer, measured model, analyzer and detector. Model to be investigated is formed from transparent material, is non-scattering, has a form of a plate which normally is parallel to the beam and is homogenous in the beam direction. The information gained from a photoelastic experiment is then related to the stress or strain in the prototype, which is of different size and different material.

When the light passes through all points of the measured model, then two families of fringes are formed at the detector. The first family consists of isoclinics – the locus of points whose principal stresses have the same directions. The second fringe family consists of isochromatics – the locus of points at which the relative retardation is a certain integer number of wave-lengths.

In order to separate isoclines from isochromatics, two quarter wave plates are inserted before and after the model. The setup is then known as circular polariscope (see Fig. 5.1). Both principal states in the model are equally excited when circular light illuminates the model. This assures uniform and high fringe contrast over the detection plane. The other techniques to distinguish the types of fringes from one another in addition to circular polariscope are using loads on the model, polychromatic light or rotated crossed polarizers.

The fringes do not indicate the order of fringes (i.e. the number of wave-lengths of relative retardation which it represents), or the sign of the relative retardation (i.e. which of the two waves is retarded to the other). To determine the orders of the fringes, a load technique is used. The sign of the fractional order depends on the handedness of QWPs, the photoelastic material properties and the direction of analyzer rotation.

Recent methods usually use a certain discrete set of different orientations of analyzer and the second quarter wave plate in order to obtain required information. The methods are called as phase shifting methods. For instance, Asundi and Liu algorithm [12] uses typical circular setup with analyzer placed at 0° , 45° , 90° , 135° , respectively. However, this produces only three independent measurements (each angular orientation from the set can be deduced from the remaining three ones). Then, QWP 2 is rotated by 45° degrees and two additional intensities for 45° and 135° analyzer orientation are measured (only one is sufficient, however). The rotation of the QWP2 is in order to obtain additional information which is used to eliminate influence of background radiation. Hence, in general there are four unknowns: background radiation, source intensity, isoclinic angle and retardation. This method works for constant background radiation and intensity of the source during the measurement.

In phase shifting methods stated so far, the required information was collected sequentially by changing the orientations of elements within the polariscope. This restricts the applications of the polariscope to the static events only. To eliminate this

drawback, another two optical setups were introduced. In the first case, three beam splitters were used in the optical setup of the polariscope. The beam splitters were used to split the beam emerging from the measured model into fourth path in four different directions. Then different configurations of a quarter-wave plate and analyzer were placed in each path in order to produce required phase shifted images. The second and most recent method introduced by Asundi and Liu [13] uses so called Multispec Imager which splits the beam emerging from the measured model into fourth path along the same directions. This brings an advantage of using only one CCD camera as a detector.

The recent technologies offer to produce micropolarizers arrays [9] and [10]. This brings a possibility of using these arrays in imaging [11] and in polarimetry in order to avoid beam splitting. However, as can be found in [9], [10] these arrays have quite low extinctions coefficients (between 100 and 300). Another difficulty is the exact orientation of transmission axes of micropolarizers. These two problems are investigated in this chapter.

5.1 Laser as a light source

In order to verify the basic mathematical model, we started with almost ideal experimental model which is depicted in Fig. 5.1. The difference in the usual setup is using He-Ne laser in order to avoid chromatic dispersion and produce almost perfect parallel rays, using Soleil-Babinet compensator as a measured model in order to compare measured data with the actual phase being introduced by the model and we used Wollaston prism in order to recover two measured intensities which are sufficient to obtain retardation information. Next, an aperture stop was placed before the detector in order to remove divergent rays and the function of chopper head is to increase signal to noise ratio of the measurement (intensity modulated signal after the photodetection was detected using Lock-In amplifier).

The measurement results when “ideal” components were used are depicted in the first graph in Fig. 5.2. The difference between measured retardation and actual retardation of the compensator is plotted as a function of the compensator retardation.

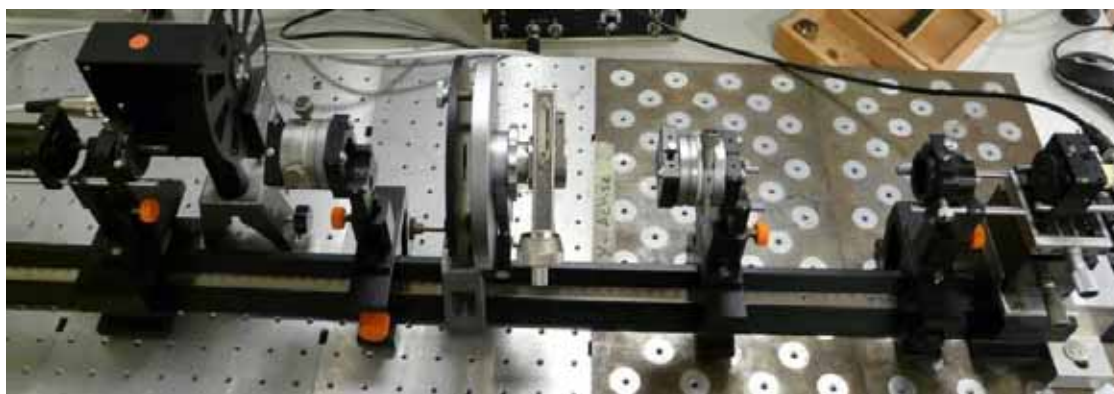


Fig. 5.1. Optical bench simulating single ray polarimeter. Components from left to right are: He-Ne laser, linear polarizer, chopper head, first quarter-wave plate (QWP 1) placed in high precision rotation mount, Soleil-Babinet compensator used as a testing model, QWP 2, Wollaston prism used as an ideal analyzer, aperture stop, photodiode.

The interference of the signal beam and a beam resulting from ghost reflections is apparent from the graph (sine envelope with period equal to π). The small fluctuations

with period approximately 20° are probably due to the surface imperfection of the compensator because they appear at the same positions in subsequent measurements. The sharp peaks at the edges are results of finite extinction coefficient of linear polarizer which was the least “ideal” component in the setup. These effects and also how the measured phase was obtained from measurement data will be treated in the next section.

The next two graphs in Fig. 5.2 illustrate influence of misalignment of the first quarter wave plane and effects when non-ideal QWP 1, although well aligned, was used. The measured results are compared to the theoretical curves obtained using Stokes calculus. The final graph shows measurements results obtained using polarizer with a poor extinction coefficient, namely 25:1.

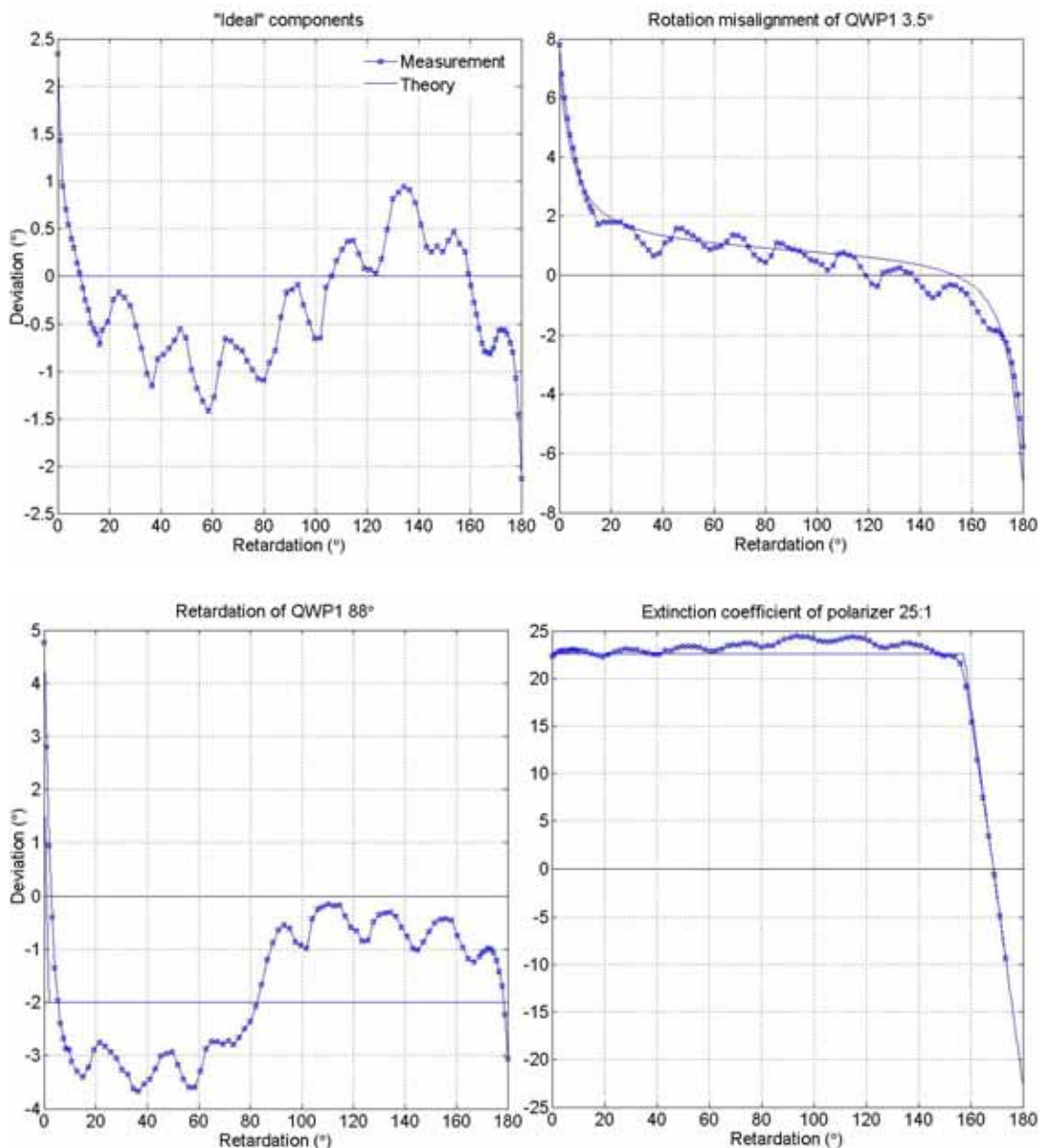


Fig. 5.2. Plots of deviations between measured retardations and actual retardations obtained using circular polarimeter setup with laser source.

In all measurements, the polarization of laser was diagonal (transmission axis of the polarizer forms reference). The angle between fast axis of the compensator and

transmission axis of polarizer, in the first three cases was 45° and in the last case 90° . We choose this value because the deviation was then maximal. The functionality of the measured data on orientation of the FA of the compensator when non-ideal polarizer is used is due to the coherency of the laser. This functionality is not observed using LED as a source.

5.2 Using of non-ideal polarizers and depolarizations effects

The usage of non-ideal QWPs of the same type has in fact not so dramatic effect on the polarimeter performances. This is because when they are used as an inverse pair (the fast axes are crossed), then imperfection retardation and chromatic dispersion is compensated. Hence main polarization imperfections firstly result from using analyzer with poor extinction coefficient and not perfect alignment of its transmission axis (as those in micropolarizers array).

Linear analyzers which are placed at four different directions, namely at 0° , 45° , 90° , 135° , will be described in the section using spin-vector formalism for its elegance.

Ideal analyzers which are perfectly alignment (no misalignment error) are represented by following set of projectors

$$\hat{P}_0 = |0\rangle\langle 0|, \hat{P}_{45} = |45\rangle\langle 45|, \hat{P}_{90} = |90\rangle\langle 90|, \hat{P}_{135} = |135\rangle\langle 135| \quad (5.1)$$

where kets $|0\rangle$ and $|90\rangle$ form orthogonal basis and have meaning of horizontal and vertical polarization, respectively.

Non-ideal analyzers characterized with extinction coefficient e are then mathematically represented with following projectors

$$\begin{aligned} \hat{P}_0 &= |0\rangle\langle 0| + (1/e)|90\rangle\langle 90|, \hat{P}_{45} = |45\rangle\langle 45| + (1/e)|135\rangle\langle 135| \\ \hat{P}_{90} &= |90\rangle\langle 90| + (1/e)|0\rangle\langle 0|, \hat{P}_{135} = |135\rangle\langle 135| + (1/e)|45\rangle\langle 45| \end{aligned} \quad (5.2)$$

Note that in order to avoid plethora symbols, the notation for projectors is kept as for the ideal case.

Ideal analyzers with angular misalignment can be, in the first approximation, written in the form (we assume that misalignment error is small enough that we can drop the second and higher orders terms in the Taylor series of sine and cosine)

$$\begin{aligned} \hat{P}_0 &= |0\rangle\langle 0| + \alpha|0\rangle\langle 90| + \alpha|90\rangle\langle 0| \\ \hat{P}_{45} &= (1/2 - \gamma)|0\rangle\langle 0| + (1/2 + \gamma)|90\rangle\langle 90| + 1/2(|0\rangle\langle 90| + |90\rangle\langle 0|) \\ \hat{P}_{90} &= |90\rangle\langle 90| - \beta|0\rangle\langle 90| - \beta|90\rangle\langle 0| \\ \hat{P}_{135} &= (1/2 + \delta)|0\rangle\langle 0| + (1/2 - \delta)|90\rangle\langle 90| - 1/2(|0\rangle\langle 90| + |90\rangle\langle 0|) \end{aligned} \quad (5.3)$$

where all kets were expressed using horizontal-vertical basis. The angles α , γ , β and δ are deviations from ideal orientations and they are positive in counter clockwise sense.

Through combination of the preceding equations, one can treat non-ideal analyzers which possess error in angular alignment. For instance the first projector is written as

$$\hat{P}_0 = |0\rangle\langle 0| + \alpha|0\rangle\langle 90| + \alpha|90\rangle\langle 0| + \frac{1}{e} \left[|90\rangle\langle 90| - \alpha|0\rangle\langle 90| - \alpha|90\rangle\langle 0| \right] \quad (5.4)$$

and the other projectors are obtained similarly.

A general normalized state which is being measured using an analyzer is represented by density matrix in the form

$$\rho = P \left(\cos \frac{\nu}{2} |0\rangle + e^{i\varphi} \sin \frac{\nu}{2} |90\rangle \right) (\text{c.c.}) + \frac{(1-P)}{2} [|0\rangle\langle 0| + |90\rangle\langle 90|] \quad (5.5)$$

where the vector in the first brackets is a general pure state, P is degree of polarization, c.c. denotes complex conjugate, ν and φ are shown in Fig. 3.10 on page 43. Equation (5.5) hence represents a state after passing all components preceding analyzer. This representation is very convenient because ν is the retardation of device under test and $\varphi/2$ is the difference between polarizer frame and principal stresses at measured point. This can be seen from Fig. 3.10 and from the understanding of polarization transformations which take place in the circular polariscope and are depicted in Fig 5.3.

The red marked points in Fig. 5.3 are states before the first polarizer (the one in the origin of the sphere), after the polarizer action (the one with cartesian coordinates 1, 0, 0) and after passing QWP 1 (with coordinates 0, 0, 1).

Action of the device under test results in rotation in the last state about axis lying in the equatorial plane (its exact position depends on ν). Hence, the circle with its normal perpendicular to the equatorial plane is a set of all possible states after passing the DUT with a given retardation which is $\varphi/2 = 30^\circ$ for the illustrated case. This circle is then rotated about axis S_2 which is a transformation due to the QWP 2 and represents states being measured by the analyzers.

The black circle with its normal axis parallel to S_1 axis represents states before analyzer when some depolarization effects prior to analyzer were assumed, namely the degree of polarization of the states lying on the circle is $P = 0.8$.

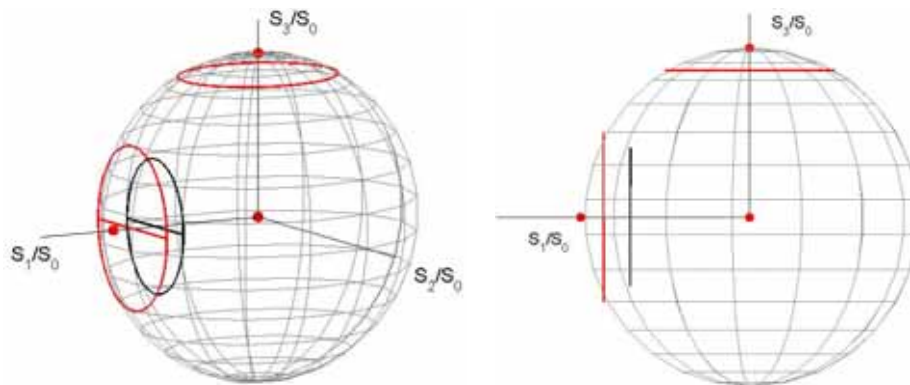


Fig. 5.3. Transformation of polarization states in circular polarimeter.

Hence, in relation (5.5), a polarization state was written in the most general way as a sum of fully polarized part and unpolarized part. This enables simultaneous treatment of coherent and incoherent light sources and depolarization effects (the origins for these effects will be discussed shortly).

The action of analyzers followed with photodiodes is then mathematically described as $\text{Tr}(\hat{P}^H \hat{P} \rho)$. The physical meaning of taking trace of the resulting matrix is obtaining irradiance of the beam impinging on a photodiode. For four different analyzer orientations, one receive following irradiances

$$\begin{aligned}
 I_0/I &= \frac{1}{2}(1 + P \cos \nu) + \alpha P \sin \nu \cos \varphi + \frac{1}{e} \left[\frac{1}{2}(1 - P \cos \nu) - \alpha P \sin \nu \cos \varphi \right] \\
 I_{45}/I &= \frac{1}{2}(1 + P \sin \nu \cos \varphi) - \gamma P \cos \nu + \frac{1}{e} \left[\frac{1}{2}(1 - P \sin \nu \cos \varphi) + \gamma P \cos \nu \right] \\
 I_{90}/I &= \frac{1}{2}(1 - P \cos \nu) - \beta P \sin \nu \cos \varphi + \frac{1}{e} \left[\frac{1}{2}(1 + P \cos \nu) + \beta P \sin \nu \cos \varphi \right] \\
 I_{135}/I &= \frac{1}{2}(1 - P \sin \nu \cos \varphi) + \delta P \cos \nu + \frac{1}{e} \left[\frac{1}{2}(1 + P \sin \nu \cos \varphi) - \delta P \cos \nu \right]
 \end{aligned} \tag{5.6}$$

where I denotes irradiance carried with the state being measured (this parameter does not appear in (5.5) because the state was normalized, i.e. divided by the own irradiance).

We split analysis of equations (5.6) into two parts. First we assume imperfection in angular misalignment of analyzers only, hence $P = 1$ and $e \rightarrow \infty$. Set of equations is then reduced to

$$\begin{aligned}
 I_0/I &= \cos^2 \frac{\nu}{2} + \alpha \sin \nu \cos \varphi, & I_{45}/I &= \frac{1}{2}(1 + \sin \nu \cos \varphi) - \gamma \cos \nu \\
 I_{90}/I &= \sin^2 \frac{\nu}{2} - \beta \sin \nu \cos \varphi, & I_{135}/I &= \frac{1}{2}(1 - \sin \nu \cos \varphi) + \delta \cos \nu.
 \end{aligned} \tag{5.7}$$

First, it is clear that due to the angular misalignment $I_0 + I_{90} \neq I_{45} + I_{135}$ hence the equations (5.7) are independent. Equations (5.7) can be solved for angles α , β , γ and δ if detected irradiances for two special cases of retardation ν are known. Namely for $\nu = 0$ and $\nu = \pi/2$.

Next, we will investigate depolarization effects alone. Setting all errors in misalignment to zero and rearranging terms one obtains from (5.7)

$$\begin{aligned}
 I_0/I &= \frac{e_2 + 1}{2e_2} \left(1 + P \frac{e_2 - 1}{e_2 + 1} \cos \nu \right) \\
 I_{45}/I &= \frac{e_2 + 1}{2e_2} \left(1 + P \frac{e_2 - 1}{e_2 + 1} \sin \nu \cos \varphi \right) \\
 I_{90}/I &= \frac{e_2 + 1}{2e_2} \left(1 - P \frac{e_2 - 1}{e_2 + 1} \cos \nu \right) \\
 I_{135}/I &= \frac{e_2 + 1}{2e_2} \left(1 - P \frac{e_2 - 1}{e_2 + 1} \sin \nu \cos \varphi \right)
 \end{aligned} \tag{5.8}$$

where an additional index was attached to the extinction coefficient in order to distinguish between first polarizer and measuring polarizer (analyzer). In this set of equations, there are only three independent, however. Next, one can see that both P and e reduce the modulation of the useful signal (retardation ν and isoclinic angle φ

are searched unknowns) in the exactly same way. To illustrate this in more detail, let us recall that the reasons for $P < 1$ are non-coherent light source (LED diode as a light source is assumed), non-ideal polarizer, and chromatic dispersion which strictly pseudo-depolarize the light. The difference between depolarization and pseudo-depolarization was discussed in the chapter concerning vibrometry. However, even when a coherent light source is used in polarimetry, there is no time varying path difference so it is not necessary to distinguish between depolarization and pseudo-depolarization. Because of using quarter-wave plate pair, Soleil-Babinet compensator which is in fact zero-order wave plate and LED with narrow spectrum (half-width was 20 nm and central wavelength 635 nm), chromatic dispersion was negligible.

One additional depolarization effect was observed in our setup shown in Fig. 5.4. This effect cannot be neglected. Namely, we observed that placing the compensator in the beam path, even when zero retardation was set, depolarized the light. This effect is due to the non-ideal collimating. A ray which is not perpendicular to the optical axes of quartz crystals in compensator is double refracted. Hence, the double refracted rays after passing the compensator do not overlap and the resulting state of light is a statistical mixture rather than pure state which results in depolarization.

Polarizer removes energy from the wave vibrating perpendicularly to the transmission axis. The degree of polarization of the emerging light from a polarizer is related to the extinction coefficient of polarizer e_1 as $P = (e_1 - 1)/(e_1 + 1)$. So the effect of non-ideal polarizer is exactly same as the effect of non-ideal measuring polarizer (analyzer), see equation (5.8). The reason that the factor $(e_1 + 1)/2e_1$ before the brackets in (5.8) is missing is that it is hidden in I which denotes irradiance carried with the state before the measurement (after passing all components). But as was stated previously, required unknowns ν and φ are expressed using relative irradiances in order to remove requirement to measure I .

Important is that although physical reasons for depolarization can be different the final influence of depolarization on measured irradiances is the same.

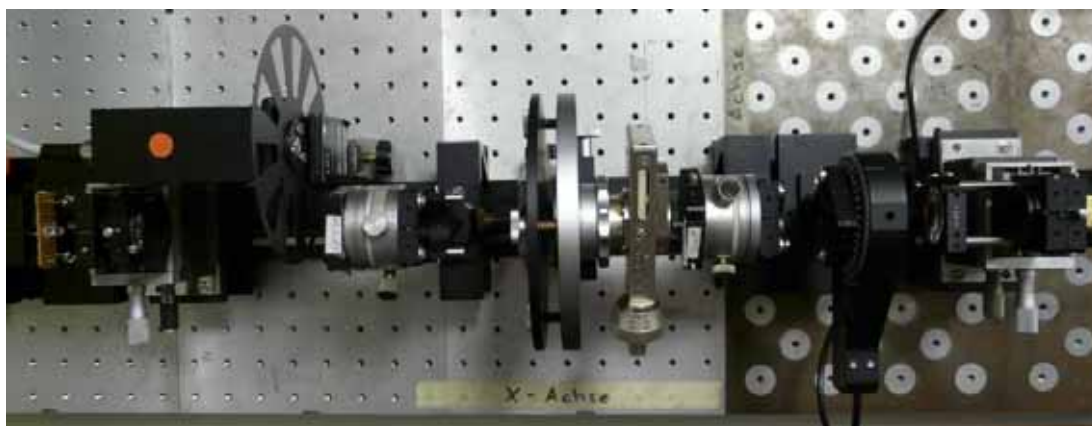


Fig. 5.4. Optical bench simulating polarimeter using LED as a light source. Components from left to right are: LED, collimating lens, polarizer, chopper head, QWP 1, compensator, QWP 2, analyzer placed in motorized high precision rotation mount, field lens, photodiode.

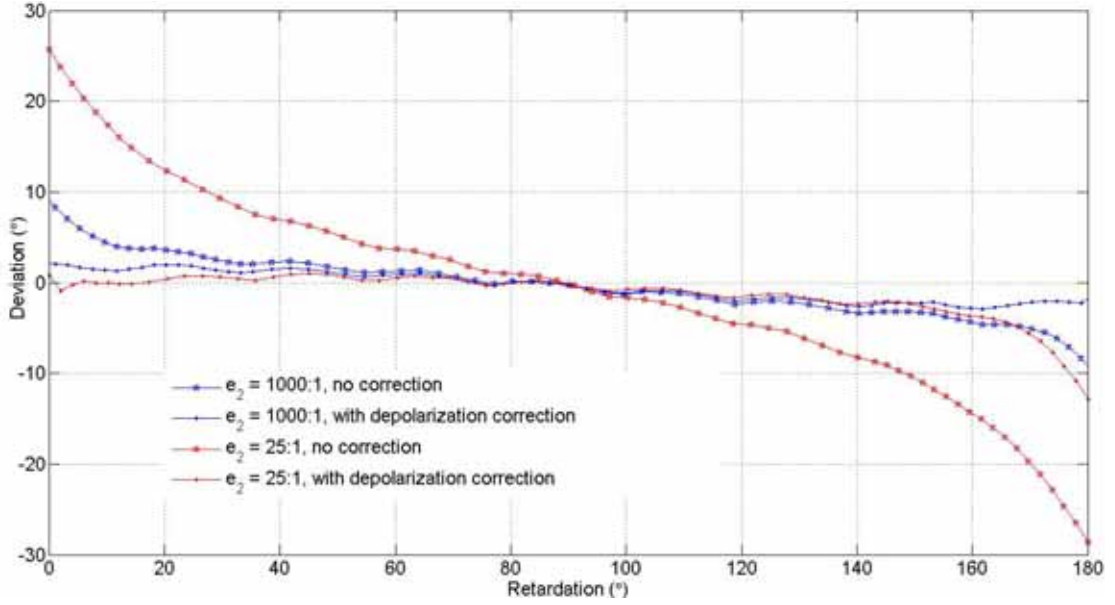


Fig. 5.5. Experimental illustration of depolarization effects.

5.3 Experimental results

Now measurement results for perfectly aligned analyzers will be presented. The measurement was performed using two kinds of analyzers which differed in extinction coefficients, namely 1000:1 and 25:1. In each case, the analyzer was then rotated using motorized high precision mount in order to obtain the four required irradiances. The retardation of the model was first computed using an ideal equation obtained from (5.8) with the settings $P = 1$ and $e \rightarrow \infty$

$$\nu = \arccos\left(\frac{I_{90} - I_0}{I_{90} + I_0}\right). \quad (5.9)$$

Then the full version of (5.8) was used in order to eliminate depolarization effects. Hence the retardation from measured data was obtained using following formula

$$\nu = \arccos\left[\frac{1}{P} \left(\frac{e_2 + 1}{e_2 - 1}\right) \cdot \frac{I_{90} - I_0}{I_{90} + I_0}\right]. \quad (5.10)$$

All results are shown in Fig. 5.5, where the deviation of measured retardation from the actual retardation is plotted as a function of actual retardation. P in (5.10) can be expressed as $P = P_C (e_1 - 1)/(e_1 + 1)$ where P_C is depolarization due to collimating as was explained earlier in the section and e_1 is the extinction coefficient of used polarizer which was 1000 in both cases. Although there are three parameters P_C , e_1 and e_2 in (5.10) which need to be determined in order to use (5.10), but due to their equivalent effects, they can be replaced with single one, P' let say. This single parameter can be then easily determined from measurement data by simply taking measured irradiances for the zero retardation as

$$0 = \arccos \left[\frac{1}{P} \left(\frac{e_2 + 1}{e_2 - 1} \right) \cdot \frac{I_{90}(0) - I_0(0)}{I_{90}(0) + I_0(0)} \right] = \arccos \left[\frac{1}{P'} \cdot \frac{I_{90}(0) - I_0(0)}{I_{90}(0) + I_0(0)} \right]. \quad (5.11)$$

In our two measurements, we obtained $P'_1 = 0.99$ and $P'_2 = 0.90$ or expressed them in terms of extinction coefficients $e'_1 = 167$ and $e'_2 = 19$, respectively.

In order to illustrate the influence of the rotational misalignment of analyzers we present another two measurements. For better illustration, we will show a list of all the measurements settings which have been discussed in this section. In the table, we distinguished between the angle which was approximately set and angles which were set with high precision (analyzers were placed in motorized high precision rotation mount, compensator was adjusted by hand).

Tab. 5.1. Measurements parameters

4 Measurements	P'	$\varphi/2$	α	β	γ	δ
Blue curves in Fig. 5.5, 5.9	0.99	$\sim 45^\circ$	$\approx 0^\circ$	$\approx 0^\circ$	$\approx 0^\circ$	$\approx 0^\circ$
Red curves in Fig. 5.5, 5.9	0.90	$\sim 45^\circ$	$\approx 0^\circ$	$\approx 0^\circ$	$\approx 0^\circ$	$\approx 0^\circ$
Blue curves in Fig. 5.6, 5.7, 5.8, 5.9	0.99	$\sim 22.5^\circ$	$\approx 0^\circ$	$\approx 0^\circ$	$\approx 0^\circ$	$\approx 0^\circ$
Red curves in Fig. 5.6, 5.7, 5.8, 5.9	0.99	$\sim 22.5^\circ$	$\approx -2.5^\circ$	$\approx -1^\circ$	$\approx 2.5^\circ$	$\approx 3.5^\circ$

In Fig. 5.6, there are shown cases when analyzers were perfectly aligned and when intentional misalignments were introduced. Recall that retardation was obtained from relative irradiances so we did not state exact units and that fluctuations of the total irradiance have no effects on measurement results and was probably caused by different transmittance of compensator for different retardation settings. The small oscillations are due to the power fluctuations of the LED.

Of course, parameters in Tab. 5.1 are usually unknown prior to measurement. We will now illustrate how in the last case, misalignment angles can be found to give better estimation of the measured retardation.

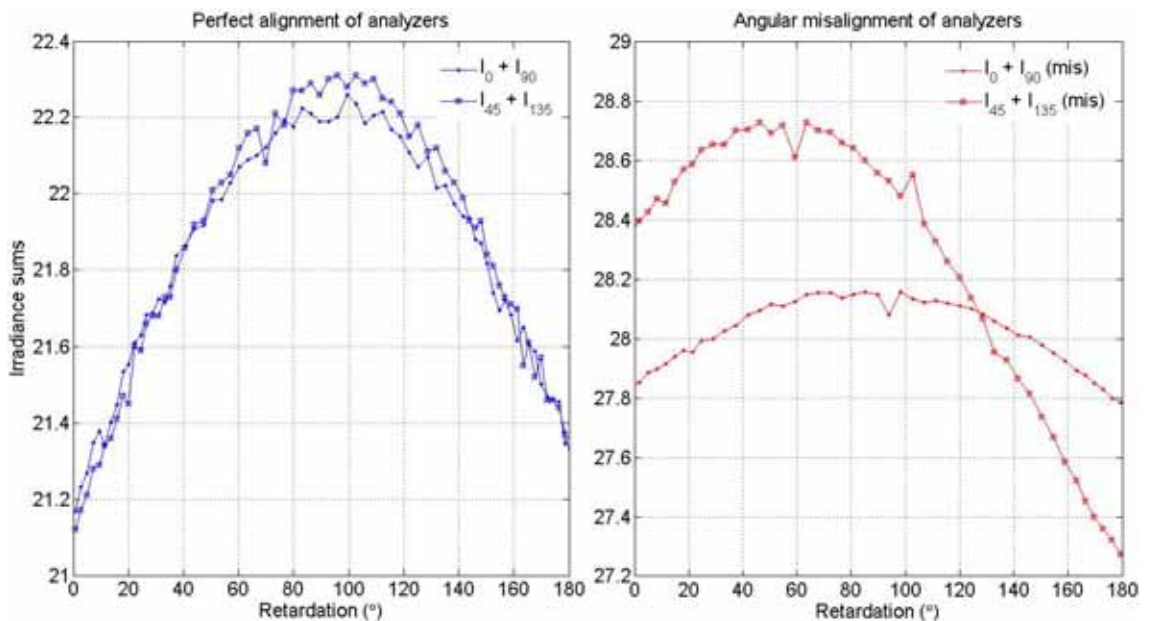


Fig. 5.6. Experimental verification of analyzers alignment using sums of irradiances for orthogonal orientations.

First, we check for measured irradiances if the equation $I_0 + I_{90} = I_{45} + I_{135}$ is held. From right part of Fig. 5.6, we can see that this is not the case, so misalignment errors are present. Next, we present all measured intensities which are depicted in Fig. 5.7.

Now we use equations (5.7) and set $\nu = 0$ which is obtained easily by measurement (no model is present)

$$\frac{I_{45}(\nu = 0)}{I} = \frac{1}{2} - \gamma \quad \text{and} \quad \frac{I_{135}(\nu = 0)}{I} = \frac{1}{2} + \delta. \quad (5.12)$$

The irradiance I can be taken in the first approximation as sum of one orthogonal pair, $I \sim I_0 + I_{90}$ let us say. Then, equations (5.12) have solutions $\gamma \sim 2.6^\circ$ and $\delta \sim 4^\circ$ which is in very good agreement with actual values (see Tab. 5.1). Unfortunately, α and β can not be obtained from (5.7) in such a simple way because it is coupled with $\cos \varphi$. But as can be seen, their spoiling effects vanish at $\nu \rightarrow 0^\circ$ and $\nu \rightarrow 180^\circ$. Hence the deviation of the measured retardation from actual value is not increased by angular misalignment at these points which are significantly influenced by depolarization effects. This is illustrated in Fig. 5.8.

Although the isoclinics angle $\varphi/2$ is the second in importance in residual stress measurement, it can be obtained from measured intensities using (5.8). The estimation of the angle φ is shown in Fig. 5.9 for all the discussed measurements.

The reason that the deviation of experimentally obtained isoclinics angle from the actual one is heavily increased when retardation approaches 0° and 180° can be understood from equations (5.7). It can be recognized that isoclinics angle is coupled with $\sin \nu$. The solution for φ is bad behaved when $\nu \rightarrow 0^\circ$ or 180° .

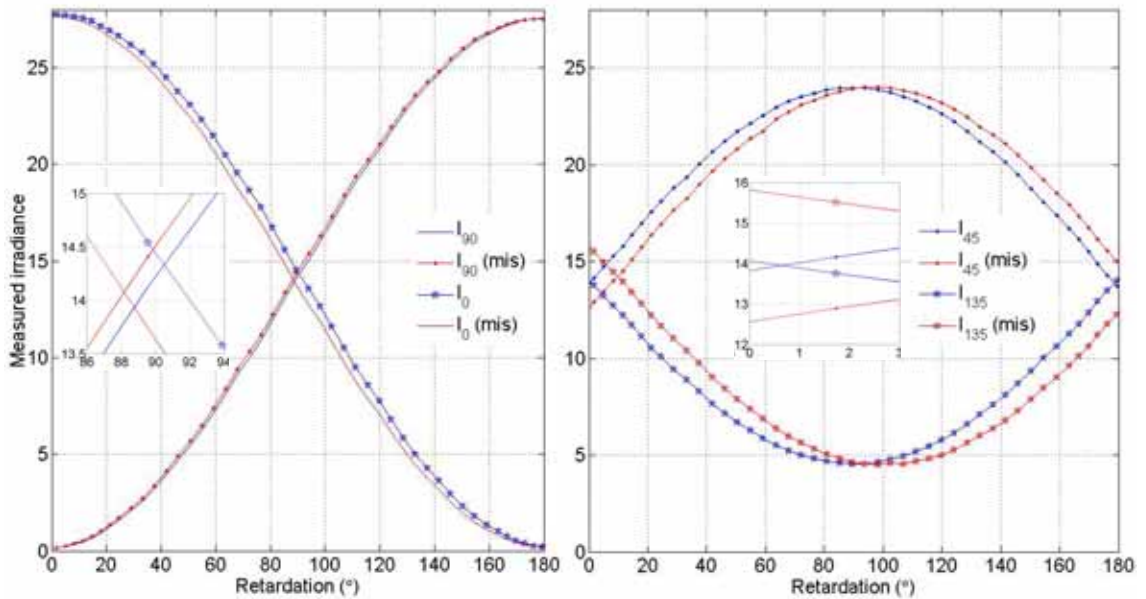


Fig. 5.7. Measured irradiances for well aligned analyzers (blue curves) and for analyzer when rotational misalignments were introduced.

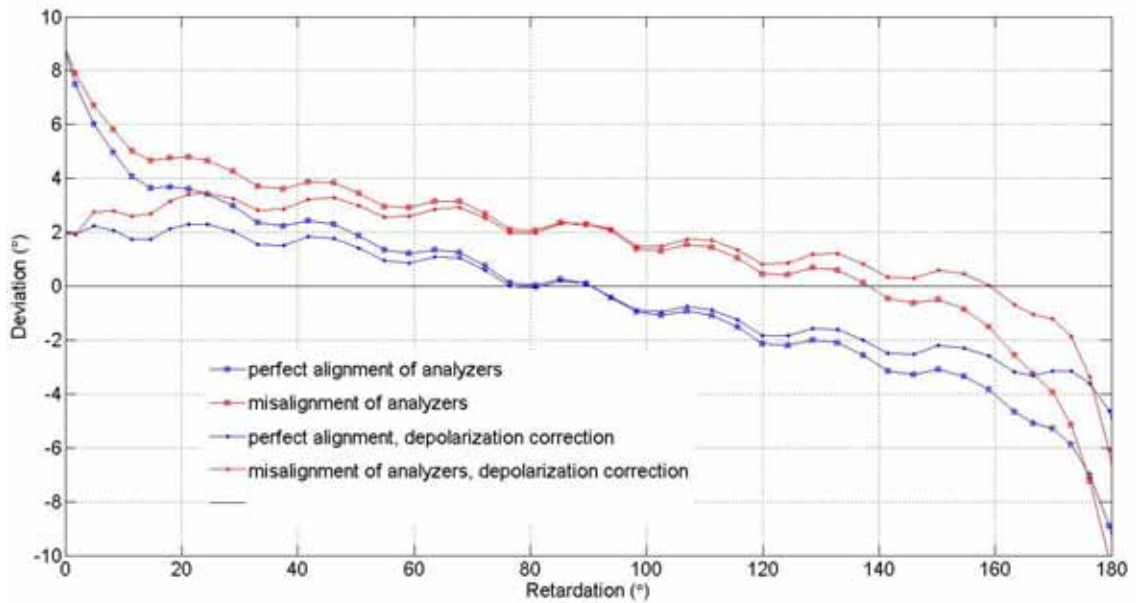


Fig. 5.8. Deviation of experimentally determined retardation from the actual one for well aligned analyzers (blue curves) and for analyzer when rotational misalignments were introduced.

Finally, we wish to report the last effect which is due to the finite extinction coefficient of the analyzer and which can bring some confusion to the calibration procedure of the compensator. Namely, we observed that with decreasing extinction coefficient, the set compensator distance between two irradiances minima was slightly enlarged. When Wollaston prism was used, the two minima was observed for compensator setting $0.0 \mu\text{m}$ and $16.5 \mu\text{m}$, let us say. These values correspond to the introduced retardation 0° and 360° . When analyzer with extinction ratio 1000:1 replaced Wollaston prism, the irradiances minima appeared at $-0.1 \mu\text{m}$ and $16.6 \mu\text{m}$. And finally, when analyzer with extinction 25:1 was used, then irradiances minima appeared at $-0.2 \mu\text{m}$ and $16.7 \mu\text{m}$. However, the calibration data obtain for Wollaston prism was used for measurements interpretation.

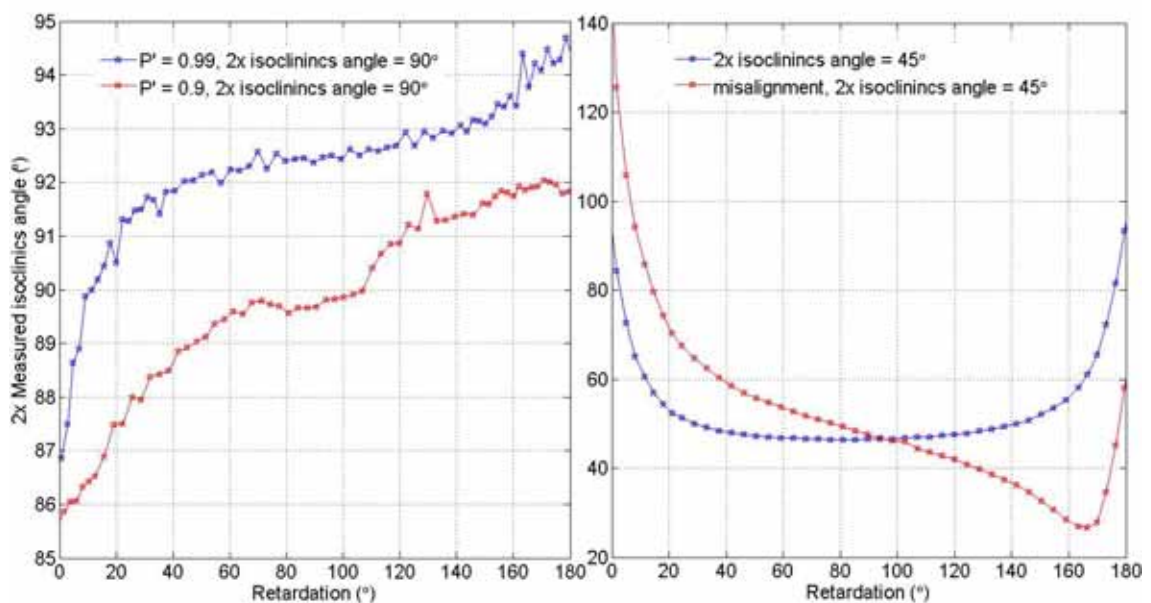


Fig. 5.9. Isoclinics angle determination from measured data.

5.4 *Polariscope with only one QWP*

In residual stress measurement can be sufficient measure the retardation introduced by the investigated model in a small range, between 0° and 20° for instance. However, from Fig. 5.8 can be seen that using circular polariscope brings maximum deviation of the measurement in this range. On the other hand, the smallest deviation is centered at 90° as can be observed from the figure.

An intuitive approach how to bring minimum deviation to the low retardation range is to remove the second QWP from the basic circular polarimeter setup. This can be shown mathematically as follow. First we write again equations (5.8) for irradiances after passing four different analyzer orientations

$$\begin{aligned} I_0/I &= \frac{1}{2}(1 + \cos \nu) \\ I_{45}/I &= \frac{1}{2}(1 + \sin \nu \cos \varphi) \\ I_{90}/I &= \frac{1}{2}(1 - \cos \nu) \\ I_{135}/I &= \frac{1}{2}(1 - \sin \nu \cos \varphi) \end{aligned} \quad (5.13)$$

where we assumed ideal analyzers. These equations were derived for general state (5.5) and angles ν and $\varphi/2$ were associated with the retardation of the model and with the isoclinics angle, respectively.

When the second QWP is not present then this associations is not valid anymore. A new association can be derived using Fig. 5.3 and Fig. 3.10 on page 43. Through the investigating of these figures it can be recognized that the first two Stokes parameters satisfy

$$S_1 = \cos^2 \frac{\nu}{2} - \sin^2 \frac{\nu}{2} \quad \text{and} \quad S_2 = \sin \nu \cos \varphi. \quad (5.14)$$

The retardation θ of the model in new polarimeter setup is then related to the Stokes parameters (5.14) as

$$\theta = \arcsin \sqrt{S_1^2 + S_2^2}. \quad (5.15)$$

Using (5.13) and (5.14) in (5.15) one obtains

$$\theta = \arcsin \sqrt{\frac{(I_{45} - I_{135})^2 + (I_0 - I_{90})^2}{I^2}}. \quad (5.16)$$

The equation (5.16) can be now compared with the equation obtained for the circular polarimeter (5.9) which is repeated here

$$\nu = \arccos \left(\frac{I_{90} - I_0}{I_{90} + I_0} \right). \quad (5.17)$$

In the circular polarimeter the minimum deviation of the measured retardation from the actual one was observed when irradiances I_{90} and I_0 posses the same values

which was for retardation $\nu = \pi/2$. As can be seen from (5.16) now the numerator of the arcsin is zero for retardation $\theta = 0$ and hence the retardation deviation is minimal there because that arcsin for zero argument has the lowest slope (minimal derivation).

5.5 Chapter summary

The current retardation measurements do not include in the mathematical algorithm analyzer imperfections. This is mainly because of using a macroscopic analyzer with good performances. However, when a micropolarizer array with limited parameters is embedded in the measurement setup, analyzers imperfections also need to be considered. The integration of the finite extinction coefficient into current measurement algorithm was made in the chapter. The special attention was paid for the residual stress measurement applications.

6 Polarization properties in communication

Quantum communication provides qualitatively new concepts which are in some aspects more powerful than their classical counterparts [31]. The most known novel schemes due to quantum communication are the secure exchange of cryptographic keys, the increase of channel capacity and the transfer of quantum information between distant parties.

This section is a study of the feasibility for adopting the concepts of quantum physics to optical communication. The quantum view on optical communication is necessary to properly describe transmissions where a sender encodes information by preparing the communication channel into a non-classical state (for example single photon transmission). But even in the schemes, where the transmitted information can be represented in classical manner, the quantum description offers new possibilities. Namely, it gives a recipe in which way the receiver should perform a measurement on the channel to ascertain which state was transmitted by the sender with the minimal probability of misdiagnosis.

Before describing quantum communication itself, a basic nomenclature of quantum mechanics is shortly presented. A special emphasis is made on describing the measurement process from the point of quantum mechanics.

Section 6.2 with the resulting relation (6.8) was published in [32]. Section 6.3 was published in [33] without considering inefficient detectors (quantum efficiency of the detector and extinction coefficient of the Wollaston prism). In the section there is an extension made to treat an inefficient detector. The nature of background radiation and its influence on communication schemas is discussed in section 6.4 which was published in [34].

Some results (the general relation (6.20) which determines the possible minimal error probability) can be compared with papers from other authors [14] and [15]. In [15] there is also presented the influence of background radiation on on-off keying schema. However, as is discussed in section 6.4, a certain contradiction was found in [15].

6.1 *Nomenclature*

A quantum system is a useful abstraction which does not really exist in nature. In fact, a quantum system is defined only in relation to the problem in which we are interested. For example if we are measuring polarization of a photon, the quantum system is not a complete photon. It is only the polarization of that photon. The most accurate definition of quantum system, unfortunately also the most abstract one, is [35]: a quantum system is whatever admits a closed dynamical description within quantum theory.

A quantum state, which mathematically represents quantum system, can be defined only in relation to a test (in a particular basis). Then, the state is characterized by the probabilities of various outcomes of the given test. Of course, different state is

defined (another basis and probabilities) by a different choice of the test, but this state describes the same quantum system. For example, a quantum system can be polarization of photons. The first test can be performed by placing a linear polarizer after preparation device which produces identical polarized photons. Another test can be realized simply by a rotation of the polarizer by some angle. In the second test, the state will be different from the state in the first test, although the quantum system is the same (a well defined polarization).

As was stated previously, terms quantum system and a test cannot be treated separately. A test is called complete if the number of different outcomes obtainable in a test of a given system is equal to a maximum number of outcomes. For example, if we test a polarization of a laser beam using a linear polarizer whose transmission axis has a fixed orientation, then the outcome of this experiment is only one measurement of intensity. On the other hand, two measurements of intensity are obtained if the laser beam is tested using a Wollaston prism. The latter test is complete test of the given system.

There are two types of states. If a quantum system is prepared in such a way that it certainly yields a predictable outcome in a complete test, then a system prepared in such a way is called to be in a pure state (for example photons emitted from laser are identically polarized). If no complete test has a predictable outcome for a given quantum system, the system is said to be in mixed state (in statistical mixture). For example, polarization of photons emitted by a thermal source is completely random.

The choice of a maximal test is analogous to the choice of a coordinate system in Euclidian geometry. The pure states which correspond to various outcomes of a maximal test are then analogous to unit vectors along a set of orthogonal vectors. Hence, it naturally arises that vectors representing pure states form a vector linear space. A pure state is usually denoted as $|\psi\rangle$.

Some quantum systems are in a state which is not completely known. More precisely, suppose a quantum system is in one of a number of states $|\psi_j\rangle$, where j is an index, with respective probabilities w_j . The set $\{w_j, |\psi_j\rangle\}$ is called as an ensemble of pure states. The density operator for the system is defined as

$$\hat{\rho} = \sum_j w_j |\psi_j\rangle\langle\psi_j| \quad (6.1)$$

and the system is also called to be in a mixed state. From experimental point of view w_j is the probability that the system will pass a test for state $|\psi_j\rangle$.

6.2 Quantum measurement

Quantum measurement can be viewed as follows. The measuring device is composed of two parts. The first one is a separator which has a certain number of channels. And the second part is a detector which detects which channel was chosen. If some channels are obscured, the measurement device works like a filter. Let us assume that the maximum number of outcomes obtainable in a test of a given system is equal to four. The complete test is shown in Fig. 6.1c). If the tested system was prepared in such a way that only the third channel in Fig. 6.1c) was active, we say that the measurement

result is b_3 and the state of the system after measurement is $|b_3\rangle$. Value b_3 is called as an eigenvalue or an observable.

A measuring device with infinitely poor resolution is illustrated in Fig. 6.1 a). No information is gained from such a measurement apparatus. The most common case is a measurement device with limited resolution.

The measuring process is mathematically represented by a complete set of orthogonal projection operators (von Neumann's approach), or simply projectors. The structure of a projector is $|b_k\rangle\langle b_k|$. Its action on a state $|\psi\rangle$ results in $|b_k\rangle\langle b_k|\psi\rangle$ which is the projection of vector $|\psi\rangle$ along the direction of $|b_k\rangle$.

Let us assume that a quantum system before being measured is in state $\hat{\rho}$ and after measurement being performed is the system in state $\hat{\rho}'$. If the quantum system was measured by a measuring device with infinitely poor resolution than [36]

$$\hat{\rho}'_{\text{ipr}} = \hat{P}_{\sum_k b_k} \hat{\rho} \hat{P}_{\sum_k b_k} \quad (6.2)$$

where

$$\hat{P}_{\sum_k b_k} = \sum_k \hat{P}_{b_k} = \sum_k |b_k\rangle\langle b_k|. \quad (6.3)$$

Note that in this special case, output state is identical to the input state. On the other hand, if an ideal measurement device was used, then

$$\hat{\rho}'_{\text{ir}} = \sum_k \hat{P}_{b_k} \hat{\rho} \hat{P}_{b_k} \quad (6.4)$$

and the system after measurement is in a pure state. And finally, when a measurement device with limited resolution was used, then

$$\hat{\rho}' = \sum_l \hat{P}_l \hat{\rho} \hat{P}_l \quad \text{where } \hat{P}_l = \hat{P}_{\sum_m b_m} \quad (6.5)$$

and m goes over the channels which cannot be distinguished for a given group l (see Fig. 6.1 b)). In (6.5), we suppressed lower index denoting the type of measuring device because (6.5) is a general case and situations (6.2) and (6.4) can be viewed as limiting cases of (6.5).

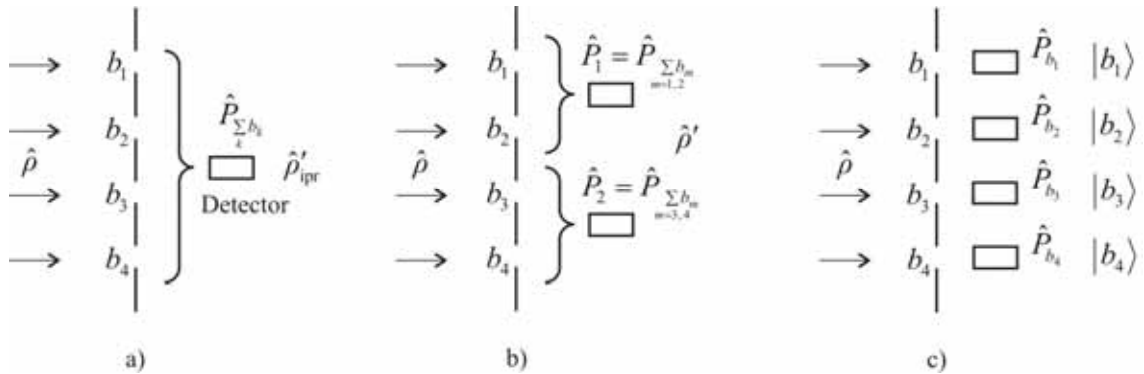


Fig. 6.1. Resolution of measuring device: a) infinitely poor resolution, b) limited resolution, c) ideal resolution.

Note that using projection operators for describing a measuring process is sometimes non-physical. In some cases, after a measurement, a given quantum system is destroyed (converted to another one). For example, when photons are measured, they are absorbed by a detector.

Now the amount of information which is gained upon measurement will be defined. For this purpose we calculate traces of $\hat{\rho}'_{\text{ipr}}$, $\hat{\rho}'_{\text{ir}}$ and $\hat{\rho}'$

$$\text{Tr}\hat{\rho}'_{\text{ipr}} = \sum_m \langle b_m | \hat{P}_{\sum_k b_k} \hat{\rho} \hat{P}_{\sum_k b_k} | b_m \rangle = \sum_j w_j \left| \sum_k \langle b_k | \psi_j \rangle \right|^2 \quad (6.5)$$

$$\text{Tr}\hat{\rho}'_{\text{ir}} = \sum_m \langle b_m | \sum_k \hat{P}_{b_k} \hat{\rho} \hat{P}_{b_k} | b_m \rangle = \sum_j w_j \sum_k \left| \langle b_k | \psi_j \rangle \right|^2 \quad (6.6)$$

$$\text{Tr}\hat{\rho}' = \sum_m \langle b_m | \sum_l \hat{P}_l \hat{\rho} \hat{P}_l | b_m \rangle = \sum_j w_j \sum_l \left| \sum_m \langle b_m | \psi_j \rangle \right|^2. \quad (6.7)$$

Let us assume that input state is normalized, i.e. $\text{Tr}\hat{\rho}=1$. Then also, $\text{Tr}\hat{\rho}'_{\text{ir}}=1$ but $\text{Tr}\hat{\rho}'_{\text{ipr}} > 1$ or $\text{Tr}\hat{\rho}'_{\text{ipr}} < 1$. This situation is a consequence of the interference (it is not certain which channel in the measuring device was chosen and hence different paths can interfere).

At this point, the amount of information gained from a given measurement can be defined as

$$QI = \left(\log_N \frac{\text{Tr}\hat{\rho}'_{\text{ipr}}}{\text{Tr}\hat{\rho}'} \right)_{\text{max}} \quad (6.8)$$

where N denotes number of channels and the trace in numerator is computed according to (6.6) and denominator is computed according to (6.8) for the given measurement device. As can be seen from (6.6), the numerical value of $\text{Tr}\hat{\rho}'_{\text{ipr}}$ depends on the quantum system being measured. Relation (6.9) is defined for the quantum system for which it reaches a maximum value (a pure state which is an equal superposition of basis states $|b_k\rangle$ with the identical phases).

6.3 On-off keying

In the case of on-off keying (OOK) the detection space is divided into two subspaces which are characterized by projectors

$$\hat{P}_1(\xi) = \sum_{k(b_k \leq \xi)} |b_k\rangle \langle b_k|, \quad \hat{P}_2(\xi) = \sum_{k(b_k > \xi)} |b_k\rangle \langle b_k| \quad (6.9)$$

where ξ is a decision value. Relation (6.9) means that if the outcome of the measurement is lesser (greater) than ξ , then the decision of the detector is that bit 0 (bit 1) was sent.

Using a closure relation (the measurement device is assumed to represent a complete test, hence the eigenstates form orthonormal basis)

$$\sum_k |b_k\rangle\langle b_k| = 1 \quad (6.10)$$

one can write

$$\hat{P}_2(\xi) = 1 - \hat{P}_1(\xi). \quad (6.11)$$

The preparation device (transmitter or sender) produces quantum systems which carry information. Let us divide these systems into two groups. The first group corresponds to the situation when bit 0 was sent and the second group of quantum systems corresponds to the case when bit 1 was sent. These two groups are characterized by $\hat{\rho}_1, \hat{\rho}_2$, respectively. In other words, the sender encodes information by preparing the channel into a well defined quantum state $\hat{\rho}$ selected from code words alphabet $\{\hat{\rho}_1, \hat{\rho}_2\}$.

The task of the receiver is to make a decision between two hypotheses. First is, that the transmitted state is $\hat{\rho}_1$. This hypothesis is selected when the measurement result corresponds to $\hat{P}_1(\xi)$. Similarly, the second hypothesis, transmitting of state $\hat{\rho}_2$, is selected when the measurement result corresponds to $\hat{P}_2(\xi)$. One can write for the probability of right decision

$$\begin{aligned} P_C(\xi) &= p_1 \sum_{k(b_k \leq \xi)} \langle b_k | \hat{\rho}_1 | b_k \rangle + (1 - p_1) \sum_{k(b_k > \xi)} \langle b_k | \hat{\rho}_2 | b_k \rangle = \\ &= p_1 \text{Tr}(\hat{\rho}_1 \hat{P}_1(\xi)) + (1 - p_1) (\text{Tr} \hat{\rho}_2 - \text{Tr} \hat{\rho}_2 \hat{P}_1(\xi)) \end{aligned} \quad (6.12)$$

where p_1 denotes the probability that event 0 occurs (bit 0 was sent) and $1 - p_1$ denotes the probability of complementary event 1.

The quantum error probability (QEP) can be then expressed as

$$P_E(\xi) = 1 - P_C(\xi). \quad (6.13)$$

Now, the optimization of the detector will be done for the case $p_1 = 0.5$. Hence we will seek for the minimal QEP. First, we rewrite (6.12) as

$$P_C(\xi) = \frac{1}{2} (\text{Tr}(\Delta \hat{\rho} \hat{P}_1(\xi)) + \text{Tr} \hat{\rho}_2) \quad \text{where } \Delta \hat{\rho} = \hat{\rho}_1 - \hat{\rho}_2. \quad (6.14)$$

Next, we will suppose that states $\hat{\rho}_1, \hat{\rho}_2$ are normalized. Relation (6.14) then yields to

$$P_C(\xi) = \frac{1}{2} (\text{Tr}(\Delta \hat{\rho} \hat{P}_1(\xi)) + 1). \quad (6.15)$$

As can be seen from (6.15), the demand for minimum QEP is to maximize the term

$$\text{Tr}(\Delta \hat{\rho} \hat{P}_1(\xi)). \quad (6.16)$$

In (6.16), it is hidden how the measurement need to be performed in order to minimize QEP. The operator $\Delta \hat{\rho}$ expressed in its eigenbasis satisfies

$$\Delta \hat{\rho} |\rho_l\rangle = \rho_l |\rho_l\rangle, \quad \langle \rho_l | \rho_m \rangle = \delta_{l,m} \quad (6.17)$$

where vectors $|\rho_l\rangle$ are eigenvectors of $\Delta\hat{\rho}$ which correspond to eigenvalues ρ_l . Using (6.17), the term (6.16) can be expressed as

$$\text{Tr}(\Delta\hat{\rho}\hat{P}_1(\xi)) = \sum_{k(b_k \leq \xi)} \langle b_k | \Delta\hat{\rho} \sum_l |\rho_l\rangle\langle\rho_l| b_k \rangle = \sum_l \sum_{k(b_k \leq \xi)} \rho_l |\langle\rho_l|b_k\rangle|^2. \quad (6.18)$$

Eigenvalues ρ_l of $\Delta\hat{\rho}$ are real numbers. To maximize (6.18) the positive eigenvalues need to be maximized and negative minimized. Probability term $|\langle\rho_l|b_k\rangle|^2$ takes values 1 and 0 if and only if the condition $\langle\rho_l|b_k\rangle = \delta_{lk}$ is hold. Hence the minimum QEP is reached when the projector characterizing measuring is in the form

$$\hat{P}_{1\min} = \sum_{k(\rho_k \geq 0)} |\rho_k\rangle\langle\rho_k|. \quad (6.19)$$

From (6.19) one can see that to minimize QEP, the measurement need to be performed in basis $|\rho_l\rangle$ and not in the original basis $|b_k\rangle$. The minimal QEP can be calculated as

$$P_{\min E} = \frac{1}{2} \left(1 - \sum_{l(\rho_l \geq 0)} \langle\rho_l|\Delta\hat{\rho}|\rho_l\rangle \right) = \frac{1}{2} \left(1 - \sum_{l(\rho_l \geq 0)} \rho_l \right) \quad (6.20)$$

where relations (6.12), (6.16) and (6.19) were used.

In two following subsections, relation (6.20) will be studied for single photon transmission and for a classical OOK.

Single photon transmission

The most common situation in single photon transmission is that operators $\hat{\rho}_1, \hat{\rho}_2$ are in the form

$$\hat{\rho}_1 = |\varphi_1\rangle\langle\varphi_1|, \hat{\rho}_2 = |\varphi_2\rangle\langle\varphi_2| \quad (6.21)$$

hence they represent quantum systems in pure states $|\varphi_1\rangle$ and $|\varphi_2\rangle$.

In the case of single photon transmission, the information is usually represented by polarization state of the photon. Let us then express states $|\varphi_1\rangle, |\varphi_2\rangle$ as

$$|\varphi_1\rangle = a_{11}|x\rangle + a_{21}|y\rangle, \quad |\varphi_2\rangle = a_{12}|x\rangle + a_{22}|y\rangle \quad (6.22)$$

where $|x\rangle$ stands for vertically polarized photon and $|y\rangle$ for horizontally polarized photon. (Here we used notation $|x\rangle, |y\rangle$ rather than $|b_1\rangle, |b_2\rangle$ to emphasize that we describe polarization states of photons.) For finding $P_{\min E}$ the eigenvalue equation (6.17) needs to be solved. After straightforward calculation, one obtains eigenvalues

$$\rho_{1,2} = \pm \sqrt{1 - |\langle\varphi_1|\varphi_2\rangle|^2}. \quad (6.23)$$

And using (6.24)

$$P_{\min E} = \frac{1}{2} \left(1 - \sqrt{1 - |\langle\varphi_1|\varphi_2\rangle|^2} \right). \quad (6.24)$$

The measurement process is then performed in the new basis

$$|\rho_1\rangle = c_{11}|x\rangle + c_{21}|y\rangle, \quad |\rho_2\rangle = c_{12}|x\rangle + c_{22}|y\rangle \quad (6.25)$$

where

$$c_{2j} = \frac{(a_{21}a_{11}^* - a_{22}a_{12}^*)c_{1j}}{\alpha_j - |a_{21}|^2 + |a_{22}|^2}, \quad j = 1, 2 \quad (6.26)$$

and

$$|c_{11}|^2 + |c_{21}|^2 = 1, \quad |c_{12}|^2 + |c_{22}|^2 = 1. \quad (6.27)$$

Let us assume the ideal case where vectors $|\varphi_j\rangle$ are orthonormal. One can see from (6.24) that if the measurement is done in this basis, the QEP tends to zero as expected.

As an another example, let us assume two different situations for preparation of photons, namely

$$\begin{aligned} 1: |\varphi_1\rangle &= |x\rangle, |\varphi_2\rangle = |y\rangle \\ 2: |\varphi'_1\rangle &= |x\rangle, |\varphi'_2\rangle = \sqrt{1/2}|x\rangle + \sqrt{1/2}|y\rangle. \end{aligned} \quad (6.28)$$

These systems are used to carry information. As a measurement device is used, a Wollaston prism is followed by photo diodes (phototubes) for each channel. This measurement device is defined by a rotation angle γ of the prism (see Fig. 6.2) which corresponds to its eigenstates $|x'\rangle, |y'\rangle$. If the angle γ is zero, then the measurement device works in $|x\rangle - |y\rangle$ basis.

QEP for both types of preparation is depicted in Fig. 6.3 as a function of γ (see curves with parameter $E = 0$).

In the previous discussion, it was assumed that the measuring device consisting of a Wollaston prism and two photo detectors is ideal. That means that Wollaston prism never misdiagnoses the polarization of incident photons. However, more realistic model includes the extinction ratio e of Wollaston prism. Measurement is then represented by following operators

$$\begin{aligned} \hat{P}_1 &= |x'\rangle\langle x'| + \frac{1}{e}|y'\rangle\langle y'| \\ \hat{P}_2 &= |y'\rangle\langle y'| + \frac{1}{e}|x'\rangle\langle x'|. \end{aligned} \quad (6.29)$$

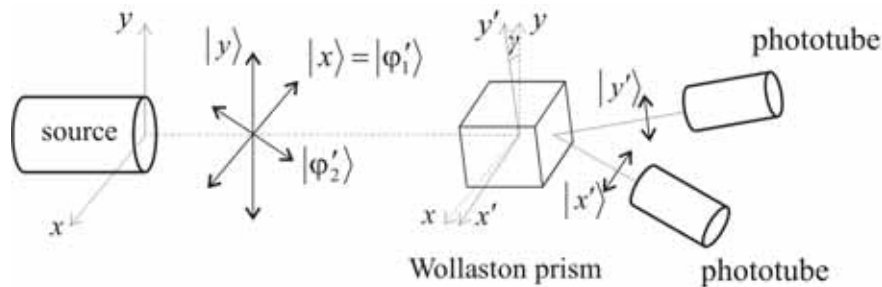


Fig. 6.2. Single photon transmission – illustration of states of polarization.

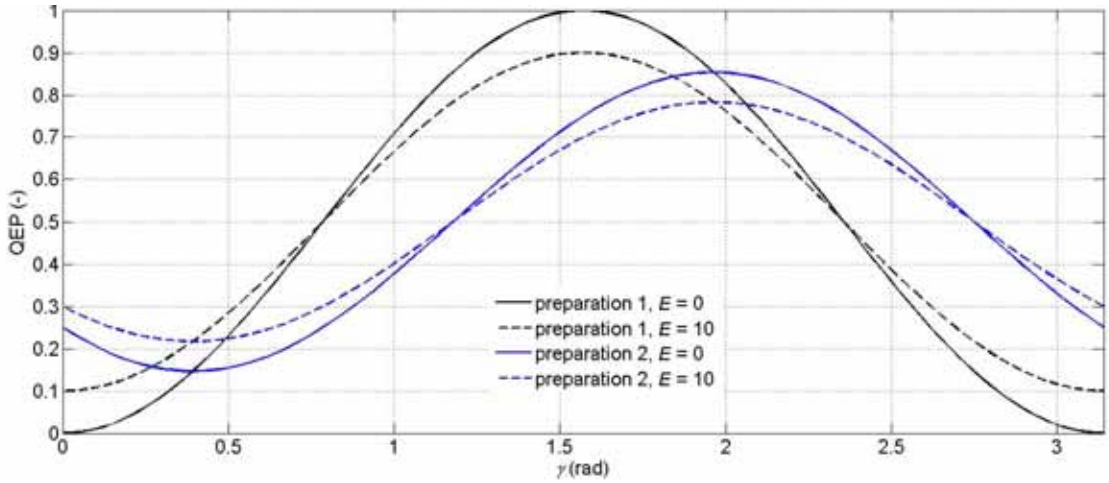


Fig. 6.3. Quantum error probability as a function of position of the Wollaston prism.

Equations (6.29) are more conveniently written in the form

$$\begin{aligned}\hat{P}_1 &= (1-E)|x'\rangle\langle x'| + E|y'\rangle\langle y'| \\ \hat{P}_2 &= (1-E)|y'\rangle\langle y'| + E|x'\rangle\langle x'|\end{aligned}\quad (6.30)$$

where $E = 1/(1+e)$ can be interpreted as the probability of misdiagnosis and the connection between reference frame and Wollaston prism frame is made by the formulas

$$\begin{aligned}|x'\rangle &= \cos\gamma|x\rangle - \sin\gamma|y\rangle \\ |y'\rangle &= \sin\gamma|x\rangle + \cos\gamma|y\rangle.\end{aligned}\quad (6.31)$$

Relation (6.12) is still valid and can be used for calculating the probability of the correct decision. After substituting of (6.30) into (6.16), one obtains

$$\text{Tr}(\Delta\hat{\rho}\hat{P}_1(\xi)) = (1-E)\sum_l \rho_l \langle x' | \rho_l \rangle + E\sum_l \rho_l \langle y' | \rho_l \rangle. \quad (6.32)$$

The expression on the left in (6.32) reaches the maximum when conditions

$$|x'\rangle = |\rho_1\rangle \quad \text{and} \quad |y'\rangle = |\rho_2\rangle \quad (6.33)$$

are met. Hence the optimal measurement basis is the same as in the case of ideal detection ($E = 0$) and the minimal QEP is expressed as (using (6.13), (6.15), (6.32) and (6.33))

$$P_{\min E} = \frac{1}{2}(1 - \rho_1(1-E) + \rho_2 E) \quad (6.34)$$

where eigenvalues $\rho_{1,2}$ are defined in (6.23). For the case when photon states are orthogonal, that is $|\varphi_1\rangle = |x\rangle$ and $|\varphi_2\rangle = |y\rangle$, one obtains the error probability $P_{\min E} = E$ as expected. QEP for the case of $E = 0.1$ and two distinct preparations (6.28) is shown in Fig. 6.3.

Classical OOK

If a light source emits a huge number of photons, the whole system of these particles can be written using a Fock space [35]. In particular, if $n_{\mathbf{k},\lambda}$ is the number of photons in state $|\mathbf{k},\lambda\rangle$, where \mathbf{k} denotes wave vector and λ polarization, then the normalized basis states in Fock space are

$$|\dots n_{\mathbf{k},\lambda} \dots\rangle = \prod_{\mathbf{k},\lambda} (n_{\mathbf{k},\lambda}!)^{-1/2} (a_{\mathbf{k},\lambda}^+)^{n_{\mathbf{k},\lambda}} |0\rangle \quad (6.35)$$

where $|0\rangle$ denotes normalized state which contains no photons and $a_{\mathbf{k},\lambda}^+$ denotes creation operator for a given mode (the action of $a_{\mathbf{k},\lambda}^+$ on $|0\rangle$ results in one photon being in the given mode).

Laser radiation will be assumed for now. Hence, there is only one possible state in which photons can occur so we can write

$$|n\rangle = (n!)^{-1/2} (a^+)^n |0\rangle. \quad (6.36)$$

A coherent state is usually expressed in the basis (6.36). The reason for the choice for this basis is that the measurement is most often performed in this basis (a photo diode simply counts photons). The next task is then to find coefficients which specify a coherent state. These coefficients can be found easily because it is well known from classical physics that probabilities of finding exactly n photons in the coherent state satisfy Poisson distribution. Using this outcome of classical physics is not in conflict with the concept of quantum mechanics. The reason is following. The result of a measurement of a quantum system must be expressed in the classical way. This statement is given by the fact that measuring devices are classical (macroscopic).

From the mentioned condition of Poisson distribution, one can deduce

$$\langle \alpha | n \rangle \langle n | \alpha \rangle = \exp(-|\alpha|^2) \frac{|\alpha|^{2n}}{n!} \quad (6.37)$$

where $|\alpha\rangle$ denotes the coherent state and $|\alpha|^2 = \langle n \rangle$ denotes average number of photons in state $|\alpha\rangle$. From the superposition principle, one obtains a familiar formula

$$|\alpha\rangle = \exp\left(-\frac{|\alpha|^2}{2}\right) \sum_{n=0}^{\infty} \frac{\alpha^n}{\sqrt{n!}} |n\rangle. \quad (6.38)$$

Note that using (6.36) and (6.38) one can show that $|\alpha\rangle$ is an eigenstate of a^+ with eigenvalue α which is in fact a rigorous definition of coherent state.

The bit 0 is represented by a quantum system in state $|0\rangle$ (no laser pulse was sent) and bit 1 is represented by a system in state $|\alpha\rangle$ (laser pulse was sent). The two projectors in the number basis are then expressed as (so called Kennedy receiver [14])

$$\hat{P}_1 = \sum_{n=1}^{\infty} |n\rangle \langle n|, \quad \hat{P}_2 = |0\rangle \langle 0|. \quad (6.39)$$

Substituting in (6.12) and assuming that $p_1 = 0.5$ one obtains

$$P_C = \frac{1}{2} \sum_{n=1}^{\infty} \langle n | \alpha \rangle \langle \alpha | n \rangle + \frac{1}{2} \langle 0 | 0 \rangle \langle 0 | 0 \rangle = \frac{1}{2} \left(\sum_{n=1}^{\infty} \frac{\langle n \rangle^n}{n!} e^{-\langle n \rangle} + 1 \right) = \frac{1}{2} (2 - e^{-\langle n \rangle}). \quad (6.40)$$

The error probability as then

$$P_E = \frac{1}{2} e^{-\langle n \rangle} \quad (6.41)$$

which is well known formula in the classical theory in which the field is assumed to have cosine form and the detection process is viewed as a discrete process.

However for $P_{\min E}$ one obtains

$$P_{\min E} = \frac{1}{2} \left(1 - \sqrt{1 - e^{-\langle n \rangle}} \right). \quad (6.42)$$

The difference between (6.41) and (6.42) is that in the case of (6.41), the measurement is done in number basis (the detector is a simple photo diode) and in the case of (6.42), a measurement is performed in a different basis, which can be determined by using preceding relations. However, each basis state in this new basis is a certain superposition of number states and hence such detector is hard to realize in practice. (In [14], a detection was described where a certain system preceding photo diode performs a unitary operation on the receiving photons which yields to the optimal detection. However, this unitary operation was only described mathematically without possible experimental setup.)

The relations (6.41) and (6.42) are plotted in Fig. 6.4 on the left and on the right, respectively (see the case with parameter $\langle n_{BR} \rangle = 0$, the other curves will be discussed further).

In the previous description of the direct detection, it was assumed that every photon arrival is registered as a photocount. However, more realistic model includes quantum efficiency η of the detector.

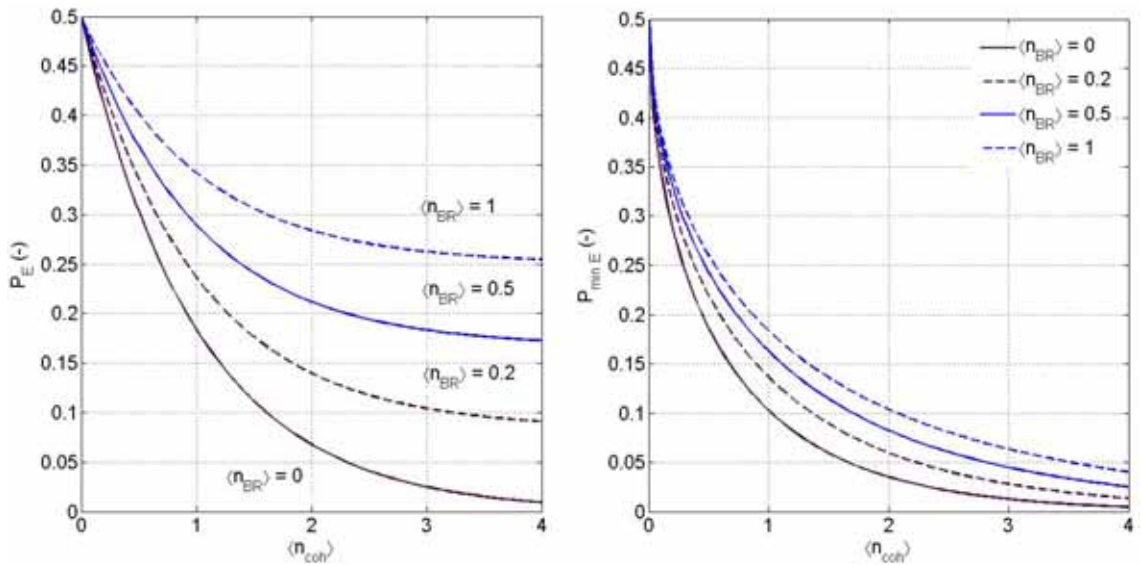


Fig. 6.4. Probability of error for classical OOK as a function of mean number of photons in the coherent state and with the mean number of photons in the background radiation as the parameter.

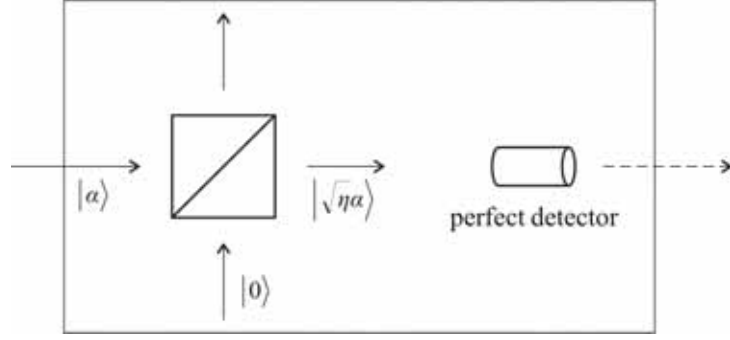


Fig. 6.5. Representation of an inefficient photo detector using beam splitter and perfect detector.

Inefficient photo detector can be represented as a perfect detector preceded by a lossless beam splitter with transmission coefficient $T = \eta^{1/2}$ as it shown in Fig. 6.5 [29].

The two input fields of beam splitter are then in states $|\alpha\rangle$ and $|0\rangle$. The field which impinges on perfect photo detector is then $|\eta^{1/2}\alpha\rangle$. The relations (6.41) and (6.42) including quantum efficiency can then be found in forms

$$P_E = \frac{1}{2} e^{-\eta\langle n \rangle} \quad (6.43)$$

and

$$P_{\min E} = \frac{1}{2} \left(1 - \sqrt{1 - e^{-\eta\langle n \rangle}} \right). \quad (6.44)$$

6.4 Background radiation

In free space optics, background radiation plays an important role. Background radiation can be seen as a special type of light source. The number of irrelevant degrees of freedom depends on used measuring device. If a photo diode is used as a measuring apparatus, then the measurement is performed in basis $|n\rangle$. Hence, the density matrix specifying background radiation source in the number state representation has a diagonal form

$$\begin{array}{ccccc}
 & \hat{\rho}|0\rangle & \hat{\rho}|1\rangle & \dots & \hat{\rho}|n\rangle \\
 |0\rangle & ? & 0 & 0 & 0 \\
 |1\rangle & 0 & ? & 0 & 0 \\
 \vdots & 0 & 0 & ? & 0 \\
 |n\rangle & 0 & 0 & 0 & ?
 \end{array} \quad (6.45)$$

The remaining matrix elements can be obtained by using the following consideration. The statement that photo diode registers exactly n photons means that events $n = 0, 1, 2, \dots, n-1$ do not occur. In other words, diagonal elements of ρ are equivalent to the question: how many independent attempts are needed to make until an event n occurs. Hence, one can guess that the required probability distribution is negative binomial distribution given by following formula

$$f(x_i) = \binom{x_i + m - 1}{m - 1} p^m (1 - p)^{x_i}, \quad x_i = 0, 1, 2, \dots; \quad 0 < p < 1 \quad \text{and} \quad m = 1, 2, \dots \quad (6.46)$$

where p denotes probability of occurrence of an event n (exactly n photons are detected) and m denotes the number of occurring events n . In our task $m = 1$. If the condition $m = 1$ is met, then one obtains from (6.45)

$$f(x_i) = p(1 - p)^{x_i}. \quad (6.47)$$

Probability distribution (6.47) is called as geometric distribution.

The diagonal elements in (6.45) then satisfy (6.47) where $x_i \equiv n$.

Up to now, the background radiation was not quantitatively characterized. To solve this problem, we calculate the average value and the variation of geometric distribution

$$E(X) = \frac{1-p}{p}, \quad D(X) = \frac{1-p}{p^2}. \quad (6.48)$$

Now, one can deduce according to the analogy with Poisson distribution that the average in (6.48) characterizes background radiation. So one can equate

$$E(X) = \langle n_{BR} \rangle \quad (6.49)$$

where $\langle n_{BR} \rangle$ denotes the average number of photons of background radiation. Using (6.48), one can calculate

$$p = \frac{1}{1 + \langle n_{BR} \rangle}. \quad (6.50)$$

Let us now assume classical OOK which was discussed in the preceding section when the background radiation is present. The coherent state itself is described by density operator $\hat{\rho}_{coh}$ which is obtained using (6.1) and (6.38). Background radiation is characterized by density matrix

$$\hat{\rho}_{BR} = \sum_n \frac{1}{1 + \langle n_{BR} \rangle} \left(\frac{\langle n_{BR} \rangle}{1 + \langle n_{BR} \rangle} \right)^n |n\rangle\langle n|. \quad (6.51)$$

Let us as an example, choose $\langle n_{BR} \rangle = 0.2$ and $\langle n_{coh} \rangle = 1$ then one obtains following matrices in number state basis (we dropped the operator notation for the matrix representation of operators)

$$\rho_{coh} = \begin{pmatrix} 0.3679 & 0.3679 & 0.2601 & 0.1502 & 0.0751 & \dots \\ 0.3679 & 0.3679 & 0.2601 & 0.1502 & 0.0751 & \\ 0.2601 & 0.2601 & 0.1839 & 0.1062 & 0.0531 & \\ 0.1502 & 0.1502 & 0.1062 & 0.0613 & 0.0307 & \\ 0.0751 & 0.0751 & 0.0531 & 0.0307 & 0.0153 & \\ \dots & & & & & \dots \end{pmatrix} \quad (6.52)$$

and

$$\rho_{BR} = \begin{pmatrix} 0.8333 & 0 & 0 & 0 & 0 & \dots \\ 0 & 0.1389 & 0 & 0 & 0 & \\ 0 & 0 & 0.0231 & 0 & 0 & \\ 0 & 0 & 0 & 0.0039 & 0 & \\ 0 & 0 & 0 & 0 & 0.0006 & \\ \dots & & & & & \dots \end{pmatrix} \quad (6.53)$$

where only first elements were shown (number basis is infinite). The state space of the composite system (coherent field and background radiation) is the tensor product of the spaces of the components. Moreover, the joint state of the total system is $\rho_{BR} \otimes \rho_{coh}$ with the basis $|n_{BR}\rangle \otimes |n_{coh}\rangle$. This basis can be also written as

$$|00\rangle, |01\rangle, \dots, |0n_{coh}\rangle, |10\rangle, |11\rangle, \dots, |1n_{coh}\rangle, \dots, |n_{BR}0\rangle, |n_{BR}1\rangle, \dots, |n_{BR}n_{coh}\rangle \quad (6.54)$$

where first number corresponds to the background radiation and second to the coherent field. The detector, however, does not distinguish between laser source photon and background radiation photon. The detector simply works in $|n\rangle$ basis. Matrix $\rho_{BR} \otimes \rho_{coh}$ expressed in basis $|n\rangle$ is then

$$\rho = \begin{pmatrix} 0.3066 & 0.3066 & 0.2168 & 0.1252 & 0.0626 & \dots \\ 0.3066 & 0.3577 & 0.2679 & 0.1613 & 0.0834 & \\ 0.2168 & 0.2679 & 0.2129 & 0.1331 & 0.0711 & \\ 0.1252 & 0.1613 & 0.1331 & 0.0866 & 0.0477 & \\ 0.0626 & 0.0834 & 0.0711 & 0.0477 & 0.0272 & \\ \dots & & & & & \dots \end{pmatrix}. \quad (6.55)$$

The analytical expression of $\rho_{BR} \otimes \rho_{coh}$ can be found as follow. Using (6.38) and (6.51), one can write

$$\rho_{BR} \otimes \rho_{coh} = \sum_n \frac{1}{1 + \langle n_{BR} \rangle} \left(\frac{\langle n_{BR} \rangle}{1 + \langle n_{BR} \rangle} \right)^n \sum_l \sum_m e^{-|\alpha|^2} \frac{\alpha^l (\alpha^*)^m}{\sqrt{l!m!}} |n\rangle \langle n| \otimes |l\rangle \langle m|. \quad (6.56)$$

The tensor product $|n\rangle \langle n| \otimes |l\rangle \langle m|$ can be written in the form $|n, l\rangle \langle n, m|$. As was stated previously, only the total number of photons is relevant for the photo detector. Hence the matrix elements of the total system expressed in this measuring basis are given by

$$\langle i | \rho_{BR} \otimes \rho_{coh} | j \rangle = \sum_n \frac{1}{1 + \langle n_{BR} \rangle} \left(\frac{\langle n_{BR} \rangle}{1 + \langle n_{BR} \rangle} \right)^n \sum_l \sum_m e^{-|\alpha|^2} \frac{\alpha^l (\alpha^*)^m}{\sqrt{l!m!}} \langle i | n+l \rangle \langle n+m | j \rangle \quad (6.57)$$

The formula (6.57) can be put into the final form

$$\langle i | \rho_{BR} \otimes \rho_{coh} | j \rangle = \sum_{k=0}^i e^{-|\alpha|^2} \frac{1}{1 + \langle n_{BR} \rangle} \frac{\alpha^{i-k} (\alpha^*)^{j-k}}{\sqrt{(i-k)!(j-k)!}} \left(\frac{\langle n_{BR} \rangle}{1 + \langle n_{BR} \rangle} \right)^k, \quad i \leq j. \quad (6.58)$$

Now the relation (6.12) and (6.13) can be used to calculate P_E . The projection operator appearing in (6.12) is given by (6.39). The operator ρ_1 represents situation

when no laser pulse was sent (bit 0). From the detector point of view, this corresponds to operator ρ_{BR} , hence $\rho_{BR} = \rho_1$. On the other hand, bit 1 is represented by $\rho = \rho_2$. The probability P_E is shown in Fig. 6.4 for different $\langle n_{BR} \rangle$.

The minimal error probability $P_{\min E}$ which can be achieved by a suitable choice of measuring basis is calculated using (6.20) where ρ_i are positive eigenvalues of matrix $\Delta\rho = \rho_{BR} - \rho$. The probability $P_{\min E}$ is plotted in Fig. 6.4 on the right.

As can be seen from Fig. 6.4, when the optimal measurement basis is used, the error probability is not so influenced by an increasing background radiation. The reason for this is that the optimal basis can distinguish relatively well between a pure coherent state and background radiation which is in a mixed state.

The same problem (influence of background radiation) was presented in [15]. The matrices ρ and ρ_{BR} for the case $\langle n_{BR} \rangle = 0.1$ and $\langle n_{coh} \rangle = 1$ are in [15] expressed as

$$\rho = \begin{pmatrix} 0.6921 & 0.3446 & 0.1213 & 0.0349 & \dots \\ 0.3446 & 0.2345 & 0.1047 & 0.0365 & \\ 0.1213 & 0.1047 & 0.0582 & 0.0245 & \\ 0.0349 & 0.0365 & 0.0245 & 0.0123 & \\ \dots & & & & \dots \end{pmatrix} \quad (6.59)$$

and

$$\rho_{BR} = \begin{pmatrix} 0.9091 & 0 & 0 & 0 & \dots \\ 0 & 0.0826 & 0 & 0 & \\ 0 & 0 & 0.0075 & 0 & \\ 0 & 0 & 0 & 0.0007 & \\ \dots & & & & \dots \end{pmatrix} \quad (6.60)$$

respectively. The matrix (6.60) describing background radiation itself has the same form also in our case when relation (6.51) is evaluated. However, matrix ρ (coherent signal with the presence of background radiation) evaluated with using the concept described in the section (now for the parameters $\langle n_{BR} \rangle = 0.1$ and $\langle n_{coh} \rangle = 1$) has in our case following matrix elements

$$\rho = \begin{pmatrix} 0.3344 & 0.3344 & 0.2365 & 0.1365 & \dots \\ 0.3344 & 0.3648 & 0.2669 & 0.1580 & \\ 0.2365 & 0.2669 & 0.2004 & 0.1208 & \\ 0.1365 & 0.1580 & 0.1208 & 0.0740 & \\ \dots & & & & \dots \end{pmatrix}. \quad (6.61)$$

A disagreement between (6.59) and (6.61) can be found. Let us recall the matrix (6.55) for coherent radiation itself where the first two diagonal elements are equal to 0.3679 and which represent probabilities of finding zero and one photon in the coherent state. Obviously, background radiation cannot increase matrix element $\rho(1,1)$ as can be seen in (6.59). Hence, matrix (6.59) cannot properly describe the situation. Note that

only analytical formula (without derivation) for calculating matrix elements of ρ is presented in [15].

Now, we will discuss single photon transmission when background radiation is present. In this case, the measurement device consists of a Wollaston prism and a photodetector for each refracted beam (see Fig. 6.6 on the left). Because in this case the measurement device is sensitive on polarization, density matrix (6.51) for background radiation needs to be expressed in a new basis according to

$$\rho_{BR} = \sum_{n_x, n_y} \frac{\langle n_x \rangle^{n_x}}{(1 + \langle n_x \rangle)^{1+n_x}} \cdot \frac{\langle n_y \rangle^{n_y}}{(1 + \langle n_y \rangle)^{1+n_y}} |n_x, n_y\rangle \langle n_x, n_y| \quad (6.62)$$

where $\langle n_x \rangle$ and $\langle n_y \rangle$ denotes mean numbers of horizontally and vertically polarized photons, respectively. One can assume that $\langle n_x \rangle = \langle n_y \rangle = \langle n_{BR} \rangle / 2$.

The source produces two quantum systems ρ_1 and ρ_2 which represent bit 0 and 1. In order to find the minimal error probability, one needs to find positive eigenvalues of

$$\text{Tr}_n(\rho_1 \otimes \rho_{BR} - \rho_2 \otimes \rho_{BR}) \quad (6.63)$$

where the tracing is over photon number. In (6.63), it was considered that the detection outcome is x (bit 0) if photocurrent $I_x > I_y$. Therefore matrix (6.63) is expressed in polarization basis and has dimension two. As a concrete example, we will assume that $\rho_1 = |x\rangle\langle x|$ and $\rho_2 = |y\rangle\langle y|$. Eigenvalue problem (6.63) was then numerically solved with results shown in Fig. 6.6 on the right. Note that the optimal measuring basis (such an angular orientation of Wollaston prism that error probability is minimal) is not influenced by background radiation.

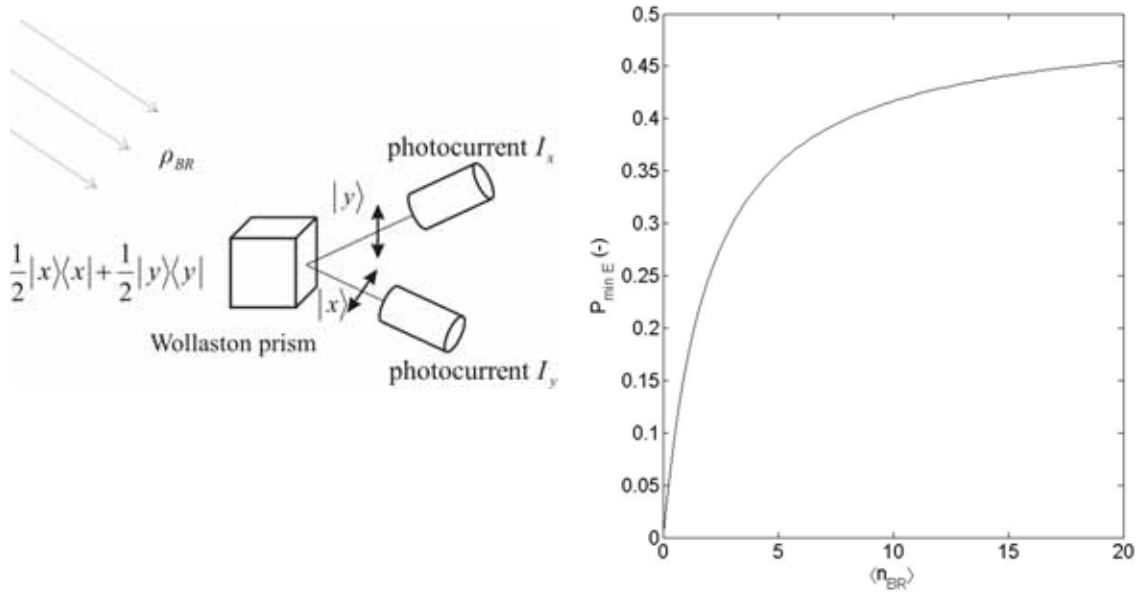


Fig. 6.6. Schema of the detector for single photon transmission and evaluated error probability as a function of background radiation strength.

Quantum communication – refinement

The previous description was limited to the description of experiments that use time-independent light beams. To incorporate time dependency the conversion of discrete mode field operators to the continuous operators is needed. Such a formal conversion can be found in [29]. For example, a single photon is then represented by a photon-wavepacket creation operator which is specified by a spectral amplitude function with a given bandwidth and the time at which peak of the pulse passes the coordinate origin (where the detector can be assumed to be placed). If the measuring time is not large enough in comparison with width of the pulse, then the photon need not to be detected. Clearly the detection probability can be incorporated into quantum efficiency of the detector as was done for on-off keying.

In the case of single photon transmission, the time dependency can be ignored with the additional assumption that the detector is activated at the time when the photon is expected (the time at which peak of the pulse passes the detector). The duration of the activation time corresponds to the bandwidth of the pulse.

6.5 Chapter summary

An attempt of using some basics of quantum theory in optical communication was made in the chapter. Main result is a procedure prescribing a measurement basis in which the minimal QEP is achieved. This procedure was applied to the simplest communication protocols where also background radiation was included.

7 Summary

The topic of the doctoral thesis was investigation of polarization imperfections of optical components which are used to control and transform polarization of light. The theoretical results of this investigation were then applied to different fields which exploit light polarization.

The first application, where the achieved results were applied to, were arrangements for high-resolution measurement of vibrating targets, i.e. interferometrical vibrometers. The required directional information can be acquired by making appropriate use of the polarization properties of the light beams brought to interference. In such arrangements, it is not generally possible to fix a mirror on the surface under consideration and as a result, the light returning from the target will be far from an ideal laser field. The spoiling effect on the interferometrical signal due to this real surface is well known. However, only non-depolarizing surfaces were treated in the literature.

We showed how depolarizing surfaces influence the interferometrical signal in the speckle regime. However, the main original contribution to the vibrometry which was made in the thesis, was eliminating of speckle field using a suitable imaging optics. In fact, we showed, that when illuminating beam is focused sharply on the target then the fundamental mode dominates in the backscattered field and has properties of the illuminating beam even for depolarizing targets. Our results were published in [16] and [17]. Next, we showed how periodic deviations, i.e. errors due to the polarization imperfection of retarders, beam splitters and linear polarizers, can be, in the first approximation, eliminated directly in the optical part of the vibrometer. Only measuring method of properties of these devices was published in [24]. However, the possibility of the direct elimination of periodic deviations was used in a research project at Pforzheim University which goal was development of a laser vibrometer with a novel architecture.

The achieved author results in the vibrometry gave motivation to investigate polarization imperfections in polarimetry, i.e. interferometric measurements for the determination of stress-induced birefringence in transparent materials. The main contribution of this investigation is an innovation of the current algorithm which is used in order to determine the retardation of the investigated material. This result will be used in the another project which is currently running at Pforzheim University.

Polarization imperfections play also an important role in optical communication, especially in quantum optical communication where the polarization is used to encode the transmitted information. The obtained results, namely a procedure of prescribing a measurement basis in which the minimal error probability is achieved and the structure of background radiation, were published in [32], [33] and [34]. Author wish also to note, that these results was discussed with Markus Aspelmeyer from the institute of quantum information and computation in Vienna.

And finally a quantum description of optical devices used in interferometry was given in the thesis and was published in [28].

8 References

- [1] LEWIN, A., MOHR, F., SELBACH, H. Heterodyn-Interferometer zur Vibrationanalyse. *Technisches Messen* 57, p. 335-345, 1990.
- [2] COJOCARU, E., JULEA, T., NICHITIU, F. Absorbing multilayer coatings producing a phase shift. *Applied Optics* 29(28), 1990.
- [3] LYSENKO, G. A., KORNIETS, A. S. Optimum optical system for generating interference signals in quadrature using polarization method. *Opt. Eng.* 40(3), p. 381-386, 2001.
- [4] GOODMAN, J. W. Statistical properties of laser speckle patterns in *Laser Speckle and Related Phenomena*, editor J. C. Dainty, vol. 9, p. 9-74, 1984. ISBN 0-387-13169-8.
- [5] LEHMAN, M. Optimization of wavefield intensities in phase-shifting speckle interferometry. *Optics Communication* 118, p. 199-206, 1995.
- [6] LEHMAN, M. Phase-shifting speckle interferometry with unresolved speckles: a theoretical investigation. *Optics Communication* 128, p. 325-340, 1996.
- [7] LEHMAN, M. Measurement optimization in speckle interferometry: the influence of the imaging lens aperture. *Opt. Eng.* 36(4), p. 1162-1168, 1997.
- [8] COSIJINS SUZANNE, J. A. G. *Displacement laser interferometry with sub-nanometer uncertainty*. Dissertation thesis, 2004, ISBN 90-386-2656-8.
- [9] GUO, J., BRANDY, D. Fabrication of thin-film micropolarizers arrays for visible imaging polarimetry. *Applied Optics*, vol 39, no. 10, 2000.
- [10] ZHAO, X., BOUSSAID, F., BERMARK, A., CHIGRINOV, V. G. Thin Phot-Patterned Micropolarizer Array for CMOS Image Sensors. *IEEE Photonics Technology Letters*, vol. 21, no. 12, 2009.
- [11] GRUEV, V., SPIEGEL, J. V., ENGHETA, N. Image sensor with focal plane extraction of polarimetric information. In *Proceedings of the IEEE International Symposium on circuits and systems 2006*, p. 213-216, 2006.
- [12] ASUNDI, A., LIU TONG, CHAI, G. B. Phase shifting method with a normal polariscope. *Applied Optics*, vol. 38, p. 5931-5935, 1999.
- [13] ASUNDI, A., LIU TONG, CHAI, G. B. Dynamic phase shift photoelasticity. *Applied Optics*, vol. 40, p. 3654-3658, 2001.
- [14] GEREMIA, J. M., Distinguishing between optical coherent states with imperfect detection. *Physical Review A* 70, 2004.
- [15] VILNROTTER, V., LAU C. W. Quantum detection theory for the free space channel. In *IPN Progress Report 42-146*, 2001.
- [16] KUCERA, P., MOHR, F. Partly Polarized speckles and speckle reduction in interferometry. In *Proceedings of the 14th Conference on Microwave Techniques COMITE 2008*, p. 215-220, ISBN 978-1-4244-2137-4, 2008.
- [17] KUCERA, P., MOHR, F. Influence of Non-cooperative Target on Interferometrical signal. In *SIBIRCON 2008*, p. 381-385 ISBN 978-1-4244-2133-6.
- [18] STEEGER, P. F., TOSHIMITSU ASAKURA, FERCHER, A. F. Polarization preservation in circular mode optical fibers and its measurement by speckle a method. *Journals of Lightwave Technology*, vol. LT-2, no.4, p. 435-441, 1984.

- [19] UL'YANOV, S., ZIMNYAKOV, D., TUCHIN, V. Fundamentals and applications of dynamic speckles induced by focused laser beam scattering. *Optical engineering* 33(10), p. 3189-3201, 1994.
- [20] BROSSEAU, CH. *Fundamentals of Polarized Light: A Statistical Approach*. 1998. ISBN 0-471-14302-2.
- [21] NORCIA, M., DONATI, S., D'ALESSANDRO, D. Interferometric measurements of displacement on a diffusing target by a Speckle tracing Technique. *IEEE Journal of quantum electronics*, vol. 37, No. 6, p. 800-806, 2001.
- [22] SIEGMAN, A. E. *Lasers*. 1986. ISBN 0-935702-11-3.
- [23] TARAR, Q., MOHR, F. Optical zoom system for laser Welding Robot. In *Proceedings of the 17th Conference Radioelektronika*. Brno, 2008, p. 675-679, ISBN 978-80-214-3390-8.
- [24] KUCERA, P., MOHR, F. Methods for measuring the polarization properties of retarders and beamsplitters. In *Proceedings of 17th International Scientific Conference Radioelektronika 2007*, Brno, pp. 371-746, ISBN 1-4244-0821-0.
- [25] COLLETT, E. *Polarized light – fundamentals and applications*. New York, 1993, 0-8247-8729-3.
- [26] LYSENKO, G. A. Polarization properties of a beamsplitter based on dielectric interference coating. In *BMSTU Bulletin. Series "Instruments,"* 3, pp. 96, 1995.
- [27] HOLZER, M., MOHR, F. Aspects of signal processing in laser vibrometry and their embedded realisation on FPGA with NI-LabVIEW. In *Proceedings of the 17th Conference Radioelektronika*. Brno, 2008, p. 221-225, ISBN 978-80-214-3390-8.
- [28] KUCERA, P. Quantum Description of Optical Devices Used in Interferometry. *Radioengineering*, 2007, vol. 16, no. 3, p. 1-6. ISSN 1210-2512.
- [29] LOUNDON, R. *The Quantum Theory of Light*. Oxford university press 2000, third edition, ISBN 0-19-850176-5.
- [30] GERRY, C. C., KNIGHT P.L. *Introductory Quantum Optics*. Cambridge University Press, 2005, ISBN 0 521 52735 X.
- [31] ASPELMEYER, M. Quantum communications in space. *Executive summary report*. Vienna University of Technology, 2003.
- [32] KUCERA, P., Quantum Information. In *Proceedings of the conference STUDENT EEICT 2005*, Brno, vol. 3, p. 416-420, ISBN 80-214-2890-2.
- [33] KUCERA, P., WILFERT O. Kvantová Optická Komunikace. In *Optické komunikace 2005*, Praha ČSSF, p. 87-93, ISBN 80-86742-10-5.
- [34] KUCERA, P. Description of Quantum States Using in Free Space Optic Communication. In *Proceedings of ESA/CNES ICSO 2006*, Noordwijk, The Netherlands, p. 1-4, ISBN 92-9092-932-4.
- [35] PERES, A. *Quantum Theory: Concepts and Methods*. Kluwer Academic Publishers, 2002, ISBN 0-306-47120-5.
- [36] FORMANEK, J. *Úvod do kvantové teorie I*, Praha, Academia ISBN 2004 80-200-1176-6.
- [37] NEE SOE-MIE , F., NEE TSU-WEI. Principal Mueller matrix of reflection and scattering measured for a one dimensional rough surface. *Opt. Eng.* 41(5), p. 994-1001, 2002.
- [38] BROSSEAU, CH. Mueller matrix analysis of light depolarization by linear optical medium. *Optics Communications* 131, p. 229-235, 1996.

Curriculum vitae

Personal data:

Name: Petr Kučera
Address: Komenského 519, 588 56 Telč, Czech Rep.
Born: December 24, 1980 in Dačice
Marital status: single
Nationality: Czech
E-mail: petr.kucera@hs-pforzheim.de



Education:

1999 - 2004 Faculty of Electrical Engineering and Communication, Brno University of Technology
– *diploma thesis Digitalization of Chaotic system*
– *2004 final state exam – Master degree (Ing.)*

Work experience:

2004 – 2006 starting the PhD program at Brno University of Technology
– *PhD thesis: Polarization imperfections of light in interferometry*
2007 – 2007 three month study stay at Technical University in Vienna
2007 – 2009 Laser vibrometer project (University of Pforzheim in Germany)
From 2009 Polarimeter project (University of Pforzheim in Germany)

Languages:

English, German, Czech

Skills:

Optics, optic communication, quantum information

Trainings:

Methods of scientific work

Personal characteristics:

Flexibility, ability to learn new things, ability to travel on business trips

Interests:

Physics, sport, poker, friends